Vertical Transport of Nearly-buoyant Particles in a Free-surface Boundary Layer

Julio Enrique Chávez Dorado

A dissertation
submitted in partial fulfillment of the
requirements for the degree of

Doctor of Philosophy

University of Washington

2026

Reading Committee:

Michelle DiBenedetto, Chair

Alberto Aliseda, Chair

Brian Polagye

Program Authorized to Offer Degree:

Mechanical Engineering

University of Washington

Abstract

Vertical Transport of Nearly-buoyant Particles in a Free-surface Boundary Layer

Julio Enrique Chávez Dorado

Co-Chairs of the Supervisory Committee:
Dr. Michelle DiBenedetto
Department of Mechanical Engineering
Dr. Alberto Aliseda
Department of Mechanical Engineering

This dissertation investigates the vertical transport of nearly buoyant, finite-sized particles in a wind-driven free-surface boundary layer, where surface waves and turbulence coexist and interact. Predicting the transport of buoyant particles in these environments is important to many environmental systems, including microplastics in the upper ocean. Vertical transport depends on turbulent mixing and particle rise velocity, both of which are influenced by wave-driven motions, turbulence intensity, and particle properties such as buoyancy, size, and shape. Quantifying the separate and coupled effects of these processes is therefore essential for predicting particle fate and informing effective monitoring and remediation strategies.

To begin addressing this challenge, our first study focuses on separating wave and turbulence effects from Eulerian velocity measurements. We begin with Eulerian measurements because a fixed sensor samples the flow at a known location without any particle effects (i.e., particle drift, inertia, and buoyancy), providing a simpler setting for developing and validating our separation method. Even in this setting, however, separating waves and turbulence from Eulerian data is an ongoing challenge because surface wave motion and turbulence fluctuations can occur at overlapping frequencies. While advanced decomposition techniques have been developed, they often entail restrictive assumptions about the wave and turbulence interactions, require synchronized

measurements, and/or only decompose the signal spectrally without a time series reconstruction. To address this problem, we first develop a Dynamic Mode Decomposition-based algorithm to separate wave-coherent and turbulent contributions in Eulerian velocity data with minimal assumptions about the waves and turbulence. Our method is validated against synthetic, field, and laboratory signals, and it successfully reconstructs both components. Moreover, our algorithm outperforms state-of-the-art mode-based separation methods. The decomposition provides a practical tool for isolating wave and turbulence effects in time series, which we use throughout this dissertation.

In our second study, we quantify the combined effects of waves and turbulence on particle vertical transport. We evaluate the two key vertical transport parameters predicted by existing models for particles in a wind-driven free-surface boundary layers: the vertical turbulent diffusivity (turbulent mixing) and the effective particle rise velocity (particle buoyancy). Current transport models, adapted from sediment transport theory, typically rely on assumptions of a quiescent rise velocity and gradient diffusion with an unconstrained Schmidt number. Thus, we test these types of models against experiments by studying the vertical mixing of near-neutrally buoyant, finite-sized spheres, rods, and disks in a wind-driven, wavy free-surface flow, measuring their diffusivity directly from particle trajectories and comparing against concentration-based estimates. We also use the wave-turbulence separation technique we developed in our first study to characterize the influence of waves relative to turbulence in the flow. We find that particle buoyancy is the main control on the diffusivity while particle shape and finite-size effects are secondary. Furthermore, the diffusivity decreases as particle rise velocity grows relative to the turbulent fluctuations, consistent with the crossing-trajectories theory, even for finite-sized, non-spherical particles in a wavy flow. In contrast, we find that inferring the diffusivity from concentration profiles, assuming a still-water rise velocity, overestimates the diffusivity by up to 80%, consistent with an effective rise velocity lower than the quiescent value. We also find our turbulent Schmidt numbers to be greater than unity. Together, these results show that standard model closures can have biases in both their diffusivities and rise velocities when applied to buoyant particles at the ocean surface.

Having evaluated the assumptions in existing transport closures under both waves and turbulence, we next examine the separate contributions of these processes to particle dispersion. In our third study, we combine Lagrangian measurements of particle positions and velocities with Eulerian velocity measurements for the same range of wind speeds, particle rise velocities, shapes, and sizes considered in our second study. To separate wave and turbulent motions, we use a two-component model for the Lagrangian vertical-velocity autocorrelation, capturing turbulence as a decorrelating process in time and waves as a damped oscillation with its own decorrelation time. The model reproduces the measured autocorrelations and provides estimates of the wave and turbulent contributions to the velocity variance, integral time scale, and diffusivity. The model fits show that the Lagrangian turbulent correlation time, relative to the Eulerian value, decreases with increasing particle buoyancy, consistent with the crossing-trajectories effect. In contrast, the wave decorrelation time is generally longer in the Lagrangian measurements than in the Eulerian measurements, suggesting that particles sample the wave field differently from a fixed observer. Although waves dominate the velocity variance near the free surface, their contribution to the net long-time diffusivity is relatively small, with turbulence being responsible for most of the mixing. Diffusivities estimated from the autocorrelation model agree closely with independent estimates from particle mean-square displacement, and both decrease with increasing particle rise velocity, again, consistent with the crossing-trajectories effect.

Together, these results show that turbulence controls the long-time effective diffusivity of near-buoyant particles, while surface waves primarily influence the near-surface velocity variance. These results are the first of its kind to demonstrate that wave and turbulent contributions can be separated in Lagrangian measurements of particle transport in a vertically inhomogeneous free-surface boundary layer, including conditions with wave breaking.

TABLE OF CONTENTS

Page

List of Figures . . . iii

List of Tables . . . viii

Nomenclature . . . ix

Chapter 1: Introduction . . . 1
- 1.1 The ocean surface boundary layer: waves, turbulence, and their interaction . . . 6
- 1.2 Flow-particle dynamics . . . 8
- 1.3 Wave, turbulence, and particle effects on vertical transport . . . 14
- 1.4 Structure of the dissertation . . . 16

Chapter 2: Wave and turbulence separation using dynamic mode decomposition . . . 19
- 2.1 Introduction . . . 19
- 2.2 Background . . . 22
- 2.3 Methods . . . 27
- 2.4 Dataset descriptions . . . 29
- 2.5 Results and Discussion . . . 33
- 2.6 Conclusion . . . 52

Chapter 3: Dispersion and Rise velocity of Nearly-Buoyant Particles in Free-Surface Boundary Layer . . . 55
- 3.1 Introduction . . . 55
- 3.2 Background . . . 58
- 3.3 Methodology . . . 67
- 3.4 Results and Discussion . . . 78
- 3.5 Conclusions . . . 88

3.6 Appendix 90

Chapter 4: Wave and turbulence effects on Lagrangian statistics of finite-sized particles . 96
4.1 Introduction 96
4.2 Theoretical framework 99
4.3 Methods and statistics 104
4.4 Results and Discussion 106
4.5 Conclusions 116

Chapter 5: Conclusions and future work 118
5.1 Conclusions 118
5.2 Future work 120

Bibliography 121

LIST OF FIGURES

Figure Number Page

1.1 Microplastics sampled from the Great Pacific Garbage Patch by Tara Expeditions Foundation (Abreu and Pedrotti, 2019). We can observe a great variety of particle composition, shapes, and sizes. 2

1.2 Conceptual comparison of Eulerian and Lagrangian descriptions of particle transport. The Eulerian description represents the particle ensemble through a concentration profile measured at fixed spatial locations. The Lagrangian description follows individual particle trajectories and characterizes their displacement and velocity history. 3

1.3 Conceptual schematic of the physical system governing the vertical transport of nearly buoyant, finite-size particles in a free-surface boundary layer. The system includes wave orbital motion, turbulence, and particles with finite size and buoyancy. 5

2.1 Workflow of the proposed DMD wave-turbulence separation methodology. 29

2.2 DMD wave-turbulence decomposition of u-component velocity of synthetic data. (a) POD spectrum of time-delayed matrix $\mathbf{H}$. (b) Power spectra of the original data and DMD-separated wave and turbulence. A -5/3 slope line is plotted for reference. In (c) we plot a portion of the original time series, (d) the true and separated wave components using 104 DMD modes, (e) and the true and separated turbulence components. 34

2.3 Sensitivity analysis to asses the separation performance of the DMD-based algorithm for different time series length, N. A measurement of error, ϵ, was calculated for every combination of normalized rank truncation, r/n_{opt}, and normalized number of columns, n/N, in the time-delayed matrix, $\mathbf{H}$, where n_{opt} is the optimal number of columns and the optimal combination is indicated by a red cross. (a) $\epsilon = 0.1586$, at $r_{\text{opt}}/n_{\text{opt}} = 0.029$, $n_{\text{opt}}/N = 0.5911$ ($N = 10000$), (b) $\epsilon = 0.1894$, at $r_{\text{opt}}/n_{\text{opt}} = 0.043$, $n_{\text{opt}}/N = 0.509$ ($N = 7500$), (c) $\epsilon = 0.2109$, at $r_{\text{opt}}/n_{\text{opt}} = 0.061$, $n_{\text{opt}}/N = 0.540$ ($N = 5000$), and (d) $\epsilon = 0.2737$, at $r_{\text{opt}}/n_{\text{opt}} = 0.179$, $n_{\text{opt}}/N = 0.470$ ($N = 2500$). 37

2.4 Synthetic spectra used for sensitivity analysis on wave intensity $\tilde{u}_{\text{rms}}/u'_{\text{rms}}$. Wave intensity of zero represents the raw turbulence signal, u'. 40

2.5 Reconstruction error from wave and turbulence at the different wave intensities in the sensitivity analysis. 41

2.6 Comparison of the DMD-separated wave spectrum (solid teal line) to the true wave spectrum (dashed black line) and the combined wave and turbulence spectrum (solid grey line). Each figure correspond to a wave intensity: (a) $\tilde{u}_{\text{rms}}/u'_{\text{rms}} = 10$; (b) $\tilde{u}_{\text{rms}}/u'_{\text{rms}} = 5$; (c) $\tilde{u}_{\text{rms}}/u'_{\text{rms}} = 1.81$; (d) $\tilde{u}_{\text{rms}}/u'_{\text{rms}} = 1$; (e) $\tilde{u}_{\text{rms}}/u'_{\text{rms}} = 0.5$; (f) $\tilde{u}_{\text{rms}}/u'_{\text{rms}} = 0.2$. 42

2.7 Relative energy contained in the DMD modes that each wave intensity case requires to resolve the coherent features in the signal. The y axis is the energy of the DMD wave modes relative to the energy contained in the entire signal, where b_i represents the amplitude of the i-th DMD mode, while $b_{\text{wave},i}$ represents the amplitude of the subset of DMD modes associated with wave motion and used in the reconstruction of the wave signal. 43

2.8 DMD wave-turbulence decomposition of u-component velocity of field data. (a) POD spectrum of time-delayed matrix $\mathbf{H}$. (b) Power spectra of the original data and DMD-separated wave and turbulence. A gray -5/3 slope line is plotted for reference. (c) A portion of the time-series of the original and decomposed signals. The wave motion was reconstructed using 34 DMD modes. 44

2.9 DMD wave-turbulence decomposition of u-component velocity of laboratory data. (a) POD spectrum of time-delayed matrix $\mathbf{H}$. (b) Power spectra of the original data and DMD-separated wave and turbulence. A gray -5/3 slope line is plotted for reference. (c) A portion of the time-series of the original and decomposed signals. The wave motion was reconstructed using 506 DMD modes. 46

2.10 DMD wave-turbulence decomposition of w-component velocity of laboratory data. (a) POD spectrum of time-delayed matrix $\mathbf{H}$. (b) Power spectra of the original data and DMD-separated wave and turbulence. A gray -5/3 slope line is plotted for reference. (c) A portion of the time-series of the original and decomposed signals. The wave motion was reconstructed using 732 DMD modes. 47

2.11 The u and w velocity components of DMD-separated wave time series of the laboratory data. 49

2.12 Comparison of modal decomposition methods, showing the spectra of the original data and the decomposed turbulence data. (a) Synthetic data u velocity, (b) field data u velocity, (c) and (d) laboratory data u and w velocity, respectively. 50

2.13 Normalized autocorrelation of raw (u), DMD-filtered turbulence (u_{DMD}), EEMD- and SWT-filtered turbulence (u_{EEMD} and u_{SWT}, respectively) signals. (a) Synthetic data u velocity, the black line is the true turbulence, u'. (b) Field data u velocity. (c) and (d) Laboratory data u and w velocity, respectively. 51

3.1 Power spectrum of (a) surface elevation $S_{\zeta\zeta}$ and (b) depth-averaged vertical velocity S_{ww} for experiments conducted under 12 m/s and 16 m/s wind conditions. The straight black line in (b) has a $-5/3$ slope. 70

3.2 Power spectrum of Reynolds stress from the raw, wave-, and turbulence-only contribution used to assess the effectiveness of the DMD-based separation algorithm. The spectra were checked at two different depths, seen in the lower left corner of each subfigure, for 12 m/s (left column) and 16 m/s (right column). 71

3.3 Mean velocity profiles for experiments conducted under 12 m/s and 16 m/s wind conditions. The shaded regions show the 95% confidence interval derived from bootstrapping. (a) Time-averaged streamwise and vertical velocity profiles $\langle u \rangle(z)$ and $\langle w \rangle(z)$, respectively, for wind forcing at 12 and 16 m/s. (b) Corresponding streamwise and vertical velocity RMS profiles $u_{\mathrm{rms}}(z)$ and $w_{\mathrm{rms}}(z)$. 72

3.4 Vertical profiles of (a) turbulent dissipation using (Gerbi et al., 2009), (b) Kolmogorov length scale and (c) time scale and (d) eddy viscosity from (3.26). 72

3.5 Time evolution of (a-c) particle vertical dispersion and (d-f) instantaneous diffusivity $K_A = 0.5\, d\langle \Delta z_p^2(\tau) \rangle / d\tau$ for all experiments. 79

3.6 (a) Depth-averaged estimations of long-time diffusivity K_A from the asymptotic method. (b) Ratio of bulk diffusivity from the asymptotic method for each particle class to that of the nearly neutrally buoyant particles, $K_A/K_{A,n}$, versus the velocity parameter Rv. The solid line is Csanady's prediction in equation 3.14, where the shaded region represents the 95% confidence interval of the nonlinear least-squares fit to the data. 80

3.7 (a) Depth-averaged decorrelation time scale T_A as a function of the quiescent particle rise velocity w_0. (b) Decorrelation time scale normalized by the corresponding neutral-particle value, $T_A/T_{A,n}$, as a function of the velocity parameter Rv. Error bars denote the uncertainty of the fitted diffusivity. 81

3.8 Normalized concentration profiles across different particle types and flow conditions. Each subfigure corresponds to a different particle group. Larger marker sizes indicate larger particle size. 82

3.9 Vertical profiles of Eulerian turbulent diffusivity calculating assuming that the particle effective rise velocity is equal to the quiescent rise velocities. The 95% confidence intervals were obtained by bootstrap resampling, with uncertainty propagated through the concentration profile and gradient, and diffusivity calculations. We removed measurements with confidence intervals greater than 0.005 m^2/s. . . . 83

3.10 Mixing length and particle concentration profiles derived from exponential fits. (a) Mixing length ℓ_m as a function of particle rise velocity w_0 for all buoyant particle types and wind speeds. Error bars denote 95% confidence intervals from exponential-profile fits. (b) Normalized concentration profiles $\langle c\rangle(z)/c_0$ plotted against normalized depth z/ℓ_m. 84

3.11 (a) Depth-averaged vertical diffusivity from exponential fitting, $K_C = \ell_m w_0$as a function of particle rise velocity. Error bars denote 95% confidence intervals. (b) Comparison of dispersion-based diffusivity vs. diffusivity from exponential fitting; the dashed line is 1:1. 84

3.12 Normalized effective rise velocity w_r/w_0, where $w_r = K_A/\ell_m$, versus (a) velocity parameter Rv, and (b) Galileo number Ga where the black solid line represents the effective rise velocity of settling spheres in HIT from Fornari et al. (2016b). The error bars come from error propagation. We omitted the error bars for Rv and Ga to improve visualization (see Table 3.3 for the values with uncertainties). 85

3.13 (a) Depth-averaged particle turbulent diffusivity assuming $Sc_t \approx 1$ and thus $K_V \approx \nu_t$. (b) Inverse turbulent Schmidt number Sc_t^{-1} versus Rv for all particle types and both wind speeds. The solid curve is the Csanady (1963) crossing-trajectories theory fitting with $C = 1.4$. (c) Turbulent Schmidt number Sc_t plotted against Rv. . 88

3.14 Horizontal-vertical distribution of particle counts (PDF) for various particle types under 16 m/s wind forcing. Each panel displays the probability density of particle counts in the x–z plane, with darker colors indicating higher concentrations. 90

3.15 Temporal evolution of vertical concentration profiles $\langle c\rangle$ for various particle types under 12 m/s (blue shades) and 16 m/s (red shades) wind speeds. 91

4.1 (a) Lagrangian and (b) Eulerian vertical velocity autocorrelation $\rho_{ww}(\tau, z)$ for small spheres at 12 m/s wind speed at four representative depths z: 0–8 cm (yellow), 8–15 cm, 15–25 cm and 25–40 cm (blue). We used the same vertical binning for the Eulerian and Lagrangian measurements so we can compare them. The dotted black lines show the fit of the parametric model (4.11) to each autocorrelation. 107

4.2 Horizontal velocity autocorrelation $\rho_{ww}(\tau, z)$ for spheres at 12 m/s wind speed at three representative depths z: left 5–12 cm, center 12–20 cm, and right 20–33 cm. The neutral particles are shown as black lines in each panel. Only spheres are shown here for clarity; rods and disks exhibit the same trends (not shown). 108

4.3 Depth profiles of the Lagrangian autocorrelation model parameters: (a) turbulent decay time $\Phi_{t,L}$, (b) wave coherence time $\Phi_{w,L}$, (c) wave contribution fraction A_L, and (d) dominant wave frequency ω_L. 110

4.4 Depth profiles of the Eulerian autocorrelation model parameters: (a) turbulent decay time $\Phi_{t,E}$, (b) wave coherence time $\Phi_{w,E}$, (c) wave contribution fraction A_E, and (d) dominant wave frequency ω_E. 110

4.5 (a) Lagrangian and (b) Eulerian non-dimensional time scale in the depth range 20–30 cm. The error bars include the uncertainty associated with the estimates. . . 111

4.6 (a–c) Lagrangian vertical velocity variance, σ^2, associated with waves, turbulence, and their total. (d–f) Lagrangian integral time scale, T_L, associated with waves, turbulence, and their total. 113

4.7 Depth dependence of the (a) wave and (b) turbulent contributions to the total vertical diffusivity (c) for different particle shapes and wind speeds. 114

4.8 Comparison of K_A versus K. The dashed line indicates one-to-one agreement. (b) Normalized diffusivity K/K_n as a function of Rv, together with the fitted relation from (4.1) shown by the black curve. For K_A, the confidence intervals are obtained from the standard deviation of the estimate. The intervals for K and K/K_n are propagated from their respective estimated confidence intervals. 115

LIST OF TABLES

Table Number Page

2.1 Summary of dataset characteristics including some input and output parameters from the wave-turbulence decomposition. Characteristics include length of time series N, sampling frequency f_s, wave peak period T_p, and wave frequency range. . 30

2.2 Summary of the optimal number of rows m and columns n of the time-delayed matrix $\mathbf{H}$, the optimal rank truncation r used and the number of wave DMD modes ψ_{wave}, including the relative rank r/n used to separate high frequency turbulence unaffected by the wave and ψ_{wave}/r used to reconstruct the wave time series. The final column reports the relative wave intensity $\tilde{u}_{\text{rms}}/u'_{\text{rms}}$ using the DMD-separated velocities. For the synthetic data, the true wave intensity is $\tilde{u}_{\text{rms}}/u'_{\text{rms}} = 1.81$. . . . 31

2.3 Summary of sensitivity analysis from figure 2.3. 36

2.4 Comparison of errors from DMD and other modal decomposition methods applied to the longest time-series length of $N = 10000$. 36

3.1 Summary of core formulas, principles, and input data to estimate vertical turbulent diffusivity K in our experiments. 66

3.2 Wave and turbulence parameters for experiments conducted at wind speeds of 12 and 16 m/s. Wave properties and uncertainties are estimated from the vertical velocity spectra, while turbulence statistics and uncertainties are computed from near-surface fluid velocity time series. 69

3.3 Summary of the particle characteristics in quiescent water and wind-driven surface boundary layer for 12 and 16 m/s. For quiescent conditions (0 m/s), the error bounds represent the measurement tolerances for particle physical properties (such as diameter and density) and confidence intervals of terminal rise velocity across multiple releases of particles in still water. The uncertainty for the non-dimensional parameters is calculated through error propagation. For wind-driven conditions (> 0 m/s), the error bounds represent standard deviation due to the spread of the particles' vertical positions through the water column. 75

NOMENCLATURE

Chapter 1

A: Projected particle area facing the flow.

C_D: Particle drag coefficient.

C_m: Added-mass coefficient.

d_p: Particle diameter or characteristic particle length scale.

F_D: Drag force acting on the particle.

g: Magnitude of gravitational acceleration.

$\mathbf{g}$: Gravitational acceleration vector.

$\mathcal{H}$: Coefficient multiplying the Basset history-force term.

ℓ_f: Characteristic length scale of the fluid.

ℓ_η: Kolmogorov length scale.

m_f: Displaced fluid mass.

m_p: Particle mass.

Re_p: Particle Reynolds number.

St: Stokes number.

Rv: Non-dimensional rise-velocity parameter.

Sz: Relative particle-size parameter.

t: Time.

$\mathbf{u}_f$: Fluid velocity evaluated at the particle position.

$\mathbf{u}_p$: Particle velocity.

w_d: Particle drift velocity relative to the fluid.

w_0: Quiescent particle rise or settling velocity.

w_{rms}: Vertical root-mean-square velocity.

$\mathbf{x}_p$: Particle position vector.

z: Vertical coordinate.

β: Particle density parameter.

μ: Fluid dynamic viscosity.

ν: Fluid kinematic viscosity.

ρ_f: Fluid density.

ρ_p: Particle density.

τ_η: Kolmogorov timescale of the turbulent flow.

τ_p: Particle response/relaxation time.

Chapter 2

$\mathbf{A}$: Best-fit linear evolution operator in the DMD formulation.

$\tilde{\mathbf{A}}$: Reduced-rank best-fit linear evolution operator.

a_i: Amplitude of wave component i in the wave spectrum.

b: Amplitude of DMD mode.

$\mathbf{b}$: Amplitude vector of the DMD system.

$\mathbf{C}$: Spectral-density vector of the POD modes.

f_s: Sampling frequency.

g: Magnitude of gravitational acceleration.

$\mathbf{H}$: Time-delayed Hankel-like data matrix.

k_i: Wavenumber.

$\mathbf{M}$: General data matrix used in the SVD, POD, and DMD formulations.

N: Total number of observations in the time series.

m: Number of rows in the time-delayed data matrix.

n: Number of columns in the time-delayed data matrix.

$\mathbf{U}$: Left singular-vector matrix.

$\mathbf{u}$: Left singular vector.

$\mathbf{V}$: Right singular-vector matrix.

$\mathbf{v}$: Right singular vector.

r: Rank truncation used in the POD and DMD calculations.

T: Duration of the time series.

T_p: Peak wave period.

U_i: Velocity-amplitude coefficient of wave component i.

$\langle u \rangle$: Time-averaged horizontal velocity.

u: Instantaneous horizontal velocity.

u': Horizontal turbulent velocity fluctuation.

$\tilde{u}$: Horizontal wave-orbital velocity.

v: Instantaneous transverse velocity component.

w: Instantaneous vertical velocity component.

w': Vertical turbulent velocity fluctuation.

$\tilde{w}$: Vertical wave-orbital velocity.

$\mathbf{W}$: Eigenvectors of the reduced DMD operator.

$\mathbf{X}$: Present-state data matrix.

$\mathbf{X}^+$: Pseudoinverse of the present-state data matrix.

$\mathbf{X}'$: Future-state data matrix.

x: Horizontal spatial coordinate.

z: Vertical spatial coordinate.

α: Intensity parameter of the JONSWAP spectrum.

β: JONSWAP spectral-width parameter.

γ: JONSWAP peak-enhancement factor.

ϵ: Normalized reconstruction error.

λ: Discrete-time eigenvalue of the DMD operator.

$\mathbf{\Lambda}$: Vector of discrete-time eigenvalues.

ρ_f: Fluid density.

$\mathbf{\Sigma}$: Diagonal matrix of singular values.

σ: Singular value.

τ_{sh}: Reynolds shear stress.

τ: Time lag used in the autocorrelation function.

$\mathbf{\Phi}$: High-dimensional DMD eigenvectors.

ϕ: DMD mode.

ϕ_i: Random phase of wave component i.

ψ_{wave}: Number of DMD modes used to reconstruct the wave signal.

$\mathbf{\Omega}$: Vector of continuous-time eigenvalues.

ω: Angular frequency.

ω_p: Peak angular frequency of the wave spectrum.

Chapter 3

$p_{\parallel}$: Length of the particle axis of rotational symmetry.

$p_{\perp}$: Length of the particle axes perpendicular to the axis of rotational symmetry.

b: Reference depth bin.

c_0: Initial or surface particle concentration.

c: Instantaneous particle concentration.

$\langle c \rangle$: Ensemble-averaged particle concentration.

C: Crossing-trajectories parameter.

K_A: Diffusivity estimated from the long-time particle dispersion.

K_C: Diffusivity estimated from an exponential concentration profile.

K_F: Diffusivity estimated from the particle flux.

K_V: Diffusivity estimated from the eddy viscosity.

f: Wave frequency.

f_p: Peak wave frequency.

c_p: Wave phase speed.

Ga: Galileo number.

g: Magnitude of gravitational acceleration.

$\mathbf{g}$: Gravitational acceleration vector.

h: Water depth.

k: Wavenumber.

k_p: Peak wavenumber.

La: Langmuir number.

ℓ_m: Particle mixing length.

ℓ_η: Kolmogorov length scale.

$\hat{\ell}_\eta$: Effective Kolmogorov length scale sampled by the particles.

d_p: Particle diameter or volume-equivalent particle diameter.

$\mathcal{P}$: Particle index.

Re_p: Particle Reynolds number.

w_r: Effective particle rise velocity or drift velocity.

SG: Particle specific gravity.

Sc_t: Turbulent Schmidt number.

u_*: Water friction velocity.

St: Stokes number.

Rv: Non-dimensional rise-velocity parameter.

Sz: Relative particle-size parameter.

t: Time.

u: Horizontal or streamwise fluid velocity.

$\langle u \rangle$: Mean horizontal or streamwise fluid velocity.

u': Horizontal turbulent velocity fluctuation.

u_{rms}: Root-mean-square horizontal turbulent velocity.

U_S: Surface Stokes drift velocity.

v: Spanwise or transverse fluid velocity.

w_f: Vertical fluid velocity along the particle trajectory.

w'_f: Fluctuating vertical fluid velocity along the particle trajectory.

w_p: Vertical particle velocity along the particle trajectory.

w'_p: Turbulence component of fluctuating vertical fluid velocity along the particle trajectory.

$\tilde{w}_p$: Wave component of fluctuating vertical fluid velocity along the particle trajectory.

S_{ww}: Power spectrum of the vertical velocity fluctuations.

$S_{\zeta\zeta}$: Surface-elevation power spectrum.

w_0: Quiescent particle rise velocity.

w_{rms}: Root-mean-square vertical turbulent velocity.

$\hat{w}_{\mathrm{rms}}$: Effective root-mean-square vertical turbulent velocity sampled by the particles.

x: Streamwise horizontal coordinate.

$\mathbf{x}_p$: Particle position vector.

y: Spanwise coordinate.

z: Vertical coordinate.

z_p: Vertical particle position along the particle trajectory.

$\langle \Delta z_p^2(\tau) \rangle$: Mean-square vertical particle displacement.

β: Particle density parameter.

γ: Particle response rate.

ϵ: Relative particle-fluid density difference.

ε: Turbulent kinetic energy dissipation rate.

ζ: Free-surface elevation.

λ_p: Peak wavelength.

ν: Fluid kinematic viscosity.

ν_t: Eddy viscosity.

ρ_f: Fluid density.

ρ_p: Particle density.

τ: Time lag.

τ_η: Kolmogorov timescale.

$\hat{\tau}_\eta$: Effective Kolmogorov timescale sampled by the particles.

τ_p: Particle response/relaxation time.

υ_f: Characteristic fluid velocity scale.

Φ: Particle aspect ratio.

ω: Angular frequency.

ω_p: Peak angular wave frequency.

Chapter 4

a: Wave amplitude.

A: Wave contribution fraction to the total velocity variance.

A_L: Lagrangian wave contribution fraction.

A_E: Eulerian wave contribution fraction.

$\mathcal{B}$: Vertical depth bin.

C: Crossing-trajectories parameter.

K: Total vertical turbulent diffusivity estimated from velocity autocovariance.

K_A: Turbulent diffusivity estimated from the particle mean-square displacement.

K_n: Tracer-baseline diffusivity.

K_t: Turbulent contribution to the total diffusivity.

K_w: Wave contribution to the total diffusivity.

$N(\tau, \mathcal{B})$: Number of valid trajectory samples for lag τ and bin $\mathcal{B}$.

$N_{\mathcal{B}}$: Number of valid lag-time points in depth bin $\mathcal{B}$.

$\mathcal{P}$: Particle-track index.

R: Lagrangian velocity autocovariance.

R_t: Turbulent contribution to the velocity autocovariance.

R_w: Wave contribution to the velocity autocovariance.

$\mathcal{S}_{\mathcal{P},\mathcal{B}}(\tau)$: Set of valid trajectory starting times for particle track $\mathcal{P}$, depth bin $\mathcal{B}$, and lag τ.

t: Time.

t_0: Trajectory time origin or starting time.

$T_{\mathcal{P}}$: Duration of particle trajectory $\mathcal{P}$.

T_L: Total Lagrangian integral timescale.

$T_{t,L}$: Turbulent contribution to the Lagrangian integral timescale.

$T_{w,L}$: Wave contribution to the Lagrangian integral timescale.

Φ_t: Turbulent velocity decorrelation timescale.

Φ_w: Wave velocity decorrelation timescale.

$\Phi_{t,E}$: Eulerian turbulent decorrelation timescale.

$\Phi_{w,E}$: Eulerian wave decorrelation timescale.

$\Phi_{t,L}$: Lagrangian turbulent decorrelation timescale.

$\Phi_{w,L}$: Lagrangian wave decorrelation timescale.

w_w: Vertical wave velocity.

w_p: Fluctuating vertical particle velocity along a trajectory.

w_p': Turbulent component of the particle vertical velocity fluctuation.

$\tilde{w}_p$: Wave component of the particle vertical velocity fluctuation.

x: Horizontal coordinate.

z: Vertical coordinate/depth coordinate.

z_p: Vertical particle position along a trajectory.

$\langle \Delta z_p^2(\tau) \rangle$: Mean-square vertical particle displacement.

Δz_p: Particle vertical displacement.

$\boldsymbol{\theta}$: Vector of fitted autocorrelation-model parameters.

ξ: Normalized autocorrelation-model fitting error.

ρ_{uu}: Lagrangian horizontal velocity autocorrelation.

ρ_{ww}: Lagrangian vertical velocity autocorrelation.

σ^2: Total vertical velocity variance.

σ_t^2: Turbulent vertical velocity variance.

σ_w^2: Wave-only vertical velocity variance.

σ_L^2: Total Lagrangian vertical velocity variance.

$\sigma_{t,L}^2$: Lagrangian turbulent velocity variance.

$\sigma_{w,L}^2$: Lagrangian wave velocity variance.

τ: Time lag.

ϕ: Wave phase lag.

ω_L: Dominant angular frequency in the autocorrelation model.

ω_0: Angular frequency of the illustrative wave.

ω_E: Eulerian dominant wave frequency.

ACKNOWLEDGMENTS

I am deeply grateful to my advisor, Michelle DiBenedetto, for her guidance, support, and encouragement throughout this journey. You have pushed me to become a better scientist, and I have learned not only from your advice, but also from watching you work. You are an exceptionally intelligent scientist, and your example has taught me what it means to approach science with rigor, curiosity, and integrity. Thank you for taking a chance on me and for welcoming me as your student. I will also always remember your wonderfully unfiltered comments that could make the entire lab burst out laughing. I am also very thankful to James Riley for stepping in as a mentor, for being so kind and generous with your time, and for broadening my perspective with your knowledge and advice. Talking to you has always been inspiring, and it became one of my favorite parts of the week.

I am grateful to my lab mates and friends, Lou Baker, Carlos Abarca, and Helena Schreder, for their support and for bringing so many moments of joy along the way. Lou, thank you for being an amazing postdoc, for guiding me through long experiments, and for always being willing to help whenever I came to you with questions, even after you were no longer part of the lab. Beyond the lab, I am especially grateful for your friendship and for all the boba runs, second-hand book hunts, and conversations along the way. Thank you for making my time in the lab (and in Seattle) so much more fun and memorable. Carlos, thank you for being there through the good times and the hard ones, too. We have been through quite a few changes together, and I am grateful that we could always count on each other for support along the way. I will miss your charisma, friendliness, and the Pennsylvania passion and intensity you bring to everything you care about. I will miss our many one-way sports conversations, even if I rarely had much to contribute. More than a lab mate, you have been a great friend, and I am very grateful for that. Helena, I missed having you in the lab, and and I am grateful for the memories we made volunteering together. I appreciate all the new popular culture references and Gen-Z vocabulary Carlos and you taught me, and all the ways you made the lab feel lighter. Even though our group was short lived, we created so many memories, lab stories, and imaginary enemies. I am grateful to have crossed paths with you all.

I am also very grateful to the Environmental Fluid Mechanics community, including the graduate students and faculty who welcomed us so warmly even though our lab was not part of the Civil Engineering department. It has always been a joy to be around them. They made it easy to talk not only about science, but also about life. I will always treasure the memories of learning to play soccer with you and then immediately forgetting the rules of the game.

I am deeply indebted to the Fulbright Fellowship. Without it, I would not have been able to be here. I also want to thank the United States, my home far from home, for giving me the chance to build a life, make family and wonderful friends, and pursue my dream of becoming a scientist. I would also like to thank the Link Foundation, the National Science Foundation, and the University of Washington for their generous support of my work.

Collin, thank you for being my biggest support throughout this journey. Thank you for your patience, your understanding, and for always being there when I needed you. You always seemed to know when I needed encouragement, when I needed someone to listen, and, occasionally, when I needed some no-nonsense honesty. I am so grateful to have had you by my side through all of this, and I could not have asked for a better partner to share this journey with. And last but not least, thank you to Señora Cajun Seasoning, PhD, my involuntary emotional support cat, for tolerating me every day. Thank you for the long naps by my side, the perfectly timed interruptions and for reminding me that, no matter how important a deadline seemed, there was always time for some play time.

DEDICATION

To my family and friends.

Chapter 1
INTRODUCTION

Free-surface boundary layers are ubiquitous in geophysical flows, from the atmospheric surface layer to the ocean's uppermost meters. The transport of small particles within these layers is important to understand a wide range of environmental and climatic processes, from cloud microphysics (Warhaft, 2008) to sea-ice formation (Smedsrud and Jenkins, 2004) as well as address environmental issues such as atmospheric and marine pollution (Weil et al., 1992; van Sebille et al., 2020; DiBenedetto, 2026).

In the ocean, this transport is especially difficult to characterize because particles move in a flow strongly shaped by surface waves and turbulence, all acting and interacting across a wide range of scales (D'Asaro, 2014). These particles span a broad spectrum of shape, size, and composition, from pollutants such as microplastics and oil droplets, as well as natural components such as plankton, marine snow, and frazil ice among others. Many of these particles are *near-neutrally buoyant*, meaning that their densities differ only slightly from that of seawater. This condition can be expressed as

$$\left|\frac{\rho_p - \rho_f}{\rho_f}\right| \ll 1,$$

where ρ_p and ρ_f denote the particle and seawater densities, respectively. Their characteristic sizes span tens of micrometers to several millimeters, and their shapes range from prolate forms, such as rods and fibers, to oblate forms, such as disks (Andrady, 2011). Consequently, simple tracer models do not capture their dynamics; instead, their transport is in a regime that depends on the coupled effects of particle buoyancy, particle inertia, turbulence, and waves (Mathai et al., 2020; Brandt and Coletti, 2022).

Microplastic transport is a particularly important problem in this regime because it can harm

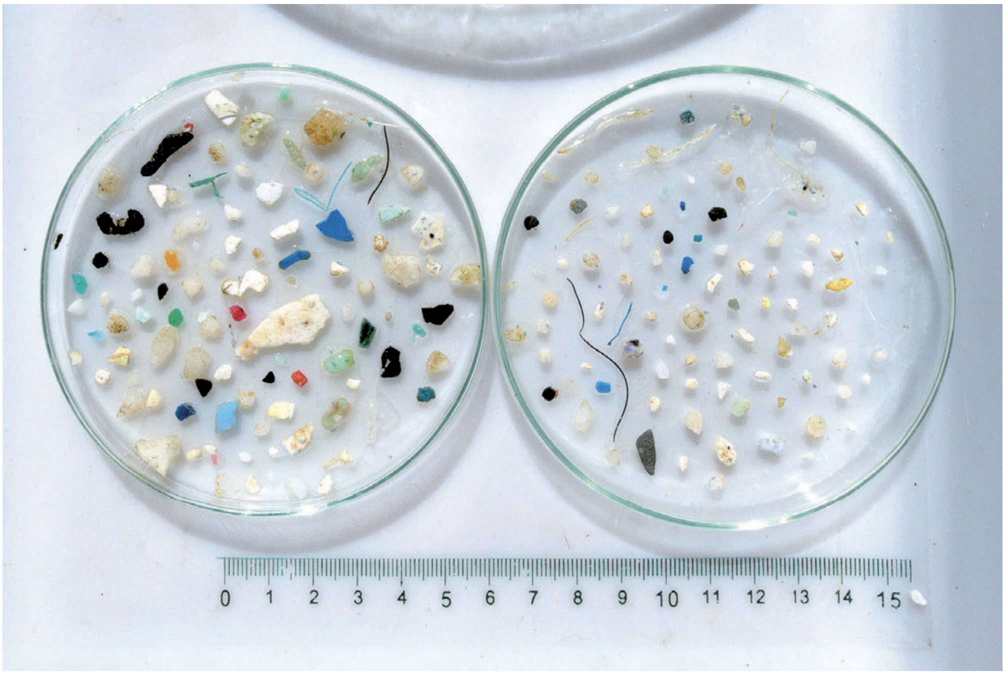

Figure 1.1: Microplastics sampled from the Great Pacific Garbage Patch by Tara Expeditions Foundation (Abreu and Pedrotti, 2019). We can observe a great variety of particle composition, shapes, and sizes.

marine animals (Titmus and David Hyrenbach, 2011) and pose risks to human health (Ragusa et al., 2021). Once released into the environment, their chemical stability allows them to travel long distances before breaking apart into different shapes and sizes. A substantial fraction of these particles in the ocean falls within the 1–5 mm size range (Cózar et al., 2014), as illustrated in figure 1.1. Microplastics span a wide range of densities, and approximately half are slightly less dense than seawater (Bond et al., 2018) which allows them to accumulate at different depths in the water column (Laist, 1987; Kukulka et al., 2012). The depth to which particles are mixed determines their residence time near the surface, where they can degrade due to sunlight exposure (Ward et al., 2019), and can get into the atmosphere due to air-sea exchange processes (Allen et al., 2022). Similarly, vertical position controls the horizontal velocities that particles experience, so small changes in vertical distribution can therefore translate into large differences in horizontal transport and spreading rates (Laxague et al., 2018). Therefore, predicting microplastic transport requires understanding how these particles are vertically distributed in the flow.

1.0.1 Lagrangian and Eulerian descriptions of transport

Vertical particle transport can be studied from either a *Lagrangian* or an *Eulerian* perspective. A Lagrangian description follows individual particles through the flow, whereas an Eulerian description characterizes the mean particle distribution and fluxes at fixed locations, as seen in figure 1.2.

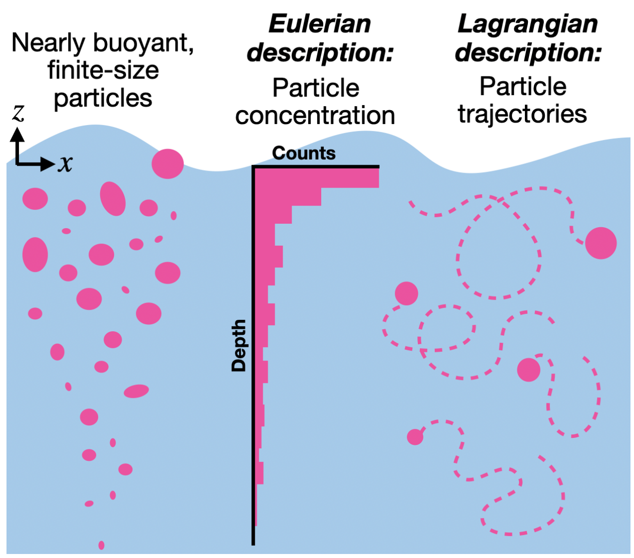

Figure 1.2: Conceptual comparison of Eulerian and Lagrangian descriptions of particle transport. The Eulerian description represents the particle ensemble through a concentration profile measured at fixed spatial locations. The Lagrangian description follows individual particle trajectories and characterizes their displacement and velocity history.

Lagrangian measurements provide direct information about particle trajectories, displacements, and velocity fluctuations. Particle transport can therefore be estimated from the long-time growth of particle spread. Equivalently, particle displacement is obtained from the particle velocity history by integrating particle velocity over time. This temporal memory is quantified by the autocorrelation function of the particle velocity fluctuations and decays with time in turbulent flows (Pope, 2000). A slowly decaying autocorrelation indicates that particles retain memory of their previous motion for longer times, whereas a rapidly decaying autocorrelation indicates faster decorrelation. The integral of the autocorrelation defines a Lagrangian integral time scale, which characterizes the duration over which particle velocity fluctuations remain correlated. Particle mixing therefore depends on both the magnitude of the velocity fluctuations and their temporal persistence (Taylor, 1922; Toschi and Bodenschatz, 2009).

This framework is particularly useful for the present problem because particle buoyancy, inertia, finite size, shape, and wave-turbulence interactions can modify both the velocity fluctuations and their correlation time (Csanady, 1963; Reeks, 1977; Pismen and Nir, 1978). Lagrangian measurements are especially valuable for studying particle dispersion across a range of spatial scales, from laboratory flows to large-scale ocean transport (LaCasce, 2008). Their main limitations are the need for sufficiently long and well-resolved trajectories and the difficulty of obtaining converged statistics in an inhomogeneous flow (Guala et al., 2007; Machicoane and Volk, 2016).

In contrast, Eulerian measurements describe the spatial distribution of particles through fixed locations. Concentration profiles and mean particle fluxes can be interpreted using a simplified advection-diffusion framework, following very restricting assumption about the turbulent mixing and particle rise velocity (Davis, 1983; Kukulka et al., 2012; Chamecki et al., 2019). Eulerian measurements are often easier to obtain making Eulerian methods a popular alternative to estimating particle transport (see for example Kukulka et al., 2012; Brunner et al., 2015; Lebreton et al., 2018; Onink et al., 2022). However, they generally require restrictive closures.

1.0.2 Vertical transport of buoyant particles

The vertical distribution of buoyant particles results from a balance between turbulent mixing and particle buoyant drift (Kukulka et al., 2012). Turbulence mixing redistributes particles throughout the water column and is parameterized by the particle turbulent diffusivity K. For particles concentrated near the free surface, this redistribution produces a net downward flux, whereas buoyant particles move upward with a characteristic rise velocity w_r, as seen in figure 1.3. The

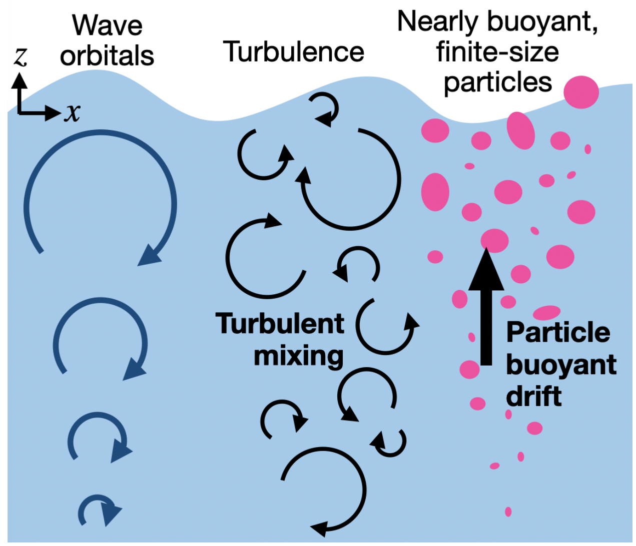

Figure 1.3: Conceptual schematic of the physical system governing the vertical transport of nearly buoyant, finite-size particles in a free-surface boundary layer. The system includes wave orbital motion, turbulence, and particles with finite size and buoyancy.

relative magnitudes of these transport processes determine whether particles remain concentrated near the surface or are mixed into the water column. Many particle-transport models use a prescribed rise velocity and a turbulent diffusivity to describe the distribution of vertical particles (Kukulka et al., 2012; Brunner et al., 2015; Chor et al., 2018a; Chamecki et al., 2019; Onink et al., 2022). However, both quantities are sensitive to the flow and particle properties and, thus, difficult to determine in a wavy free-surface boundary layer (Snyder and Lumley, 1971; Wells and Stock, 1983; Ruth et al., 2021; Li et al., 2023). Existing approaches often calculate the particle rise velocity from measurements in still water and represent turbulent mixing using an eddy-diffusivity closure adapted from sediment transport or passive-tracer models (Rouse, 1937; Kukulka et al., 2012; Kukulka and Brunner, 2015; Chamecki et al., 2019). Furthermore, particles are often assumed to disperse at the same rate as fluid momentum so their diffusivity can be approximated by the momentum diffusivity. These assumptions may be inadequate for nearly buoyant, finite-size particles because the effective rise velocity and diffusivity can differ substantially from their quiescent-fluid or tracer (Csanady, 1963; Nir and Pismen, 1979). Separating the effects of waves and turbulence from these parameters can be challenging but it is important because waves and turbulence drive different processes so their effects on particle transport can be different.

This dissertation is motivated by the need to better understand, quantify, and parameterize the vertical transport of nearly buoyant particles under realistic combinations of waves and turbulence at the free surface. The focus is on fundamental fluid mechanics; in particular, on how the flow and particle properties affect the ensemble transport of particles.

1.1 *The ocean surface boundary layer*: *waves, turbulence, and their interaction*

The ocean surface boundary layer is a highly unsteady environment. Its surface is continuously deformed by waves, and wave-turbulence interactions fundamentally modify boundary-layer structure and energetics compared to the well-studied solid-wall boundary layer (D'Asaro, 2014). The fluid dynamics in this system is shaped by wind-driven mean shear currents, surface gravity waves, and turbulence, all of which interact across a wide range of scales (Teixeira and Belcher, 2002). Together, these processes and their interactions give rise to additional mechanisms that strongly influence particle transport.

Wind can generates surface gravity waves in the open ocean. However, waves may also persist long after the wind has changed, and they can propagate over long distances with relatively little dissipation (Ardhuin et al., 2007). As a result, the wave field observed at a given location may be broadband because it can contain both locally generated waves and swell generated by winds that occurred earlier and elsewhere. Wind stress applied at the free surface also drives a horizontal current whose speed decreases with depth, producing a near-surface shear layer that is the primary source of wind-driven turbulence in the absence of strong wave effects (Thorpe, 1985).

Near the ocean surface, turbulence is generated by several coupled mechanisms, rather than by wind stress alone. Shear instabilities break down the mean flow into turbulent eddies that transport momentum downward and mix tracers, heat, and suspended particles (Thoman et al., 2021). Wave breaking provides an additional source of turbulence by transferring wave energy to subsurface turbulent kinetic energy, injects bubbles and strong intermittency into a thin near-surface layer, and enhancing dissipation rates (Craig and Banner, 1994; Terray et al., 1996; Melville, 1996)

Surface gravity waves generate a net drift of fluid particles, called Stokes drift (Stokes, 1849). Here, a fluid particle denotes an infinitesimal volume of water that follows the local fluid velocity. One explanation is that it arises because the fluid particle moves forward faster near the wave crest than it moves backward near the trough. Thus, over one wave cycle the forward displacement does not cancel exactly, producing a net transport in the direction of wave propagation. Stokes drift is a second-order Lagrangian transport effect associated with the wave motion rather than the mean Eulerian flow (van den Bremer and Breivik, 2017) and is proportional to the square of the wave amplitude, so it is strong near the surface and decays rapidly with depth. The interaction between Stokes drift and the shear-driven current leads to an instability that generates roll vortices (windrows), known as Langmuir circulation (Craik and Leibovich, 1976; Leibovich, 1983; Thorpe, 2004). These structures produce alternating bands of surface convergence and divergence, with strong downwelling jets beneath convergence zones and broader upwelling between them. Beyond the organized windrows, the same wave-current interaction can intensify near-surface turbulence, known as Langmuir turbulence (McWilliams et al., 1997; D'Asaro, 2014), which enhances turbulent kinetic energy, deepens the mixed layer, and changes the structure of vertical velocity fluctuations compared to a purely shear-driven boundary layer (Skyllingstad and Denbo, 1995; D'Asaro, 2014). This turbulence also enhances vertical motions, can submerge buoyant particles, and redistributes debris within the surface layer, sometimes over horizontal scales of tens to hundreds of meters (Kukulka et al., 2012; Brunner et al., 2015; Kukulka and Brunner, 2015).

The combined effect is a boundary layer that is strongly inhomogeneous and anisotropic, where small-scale turbulence and wave orbital motions coexist. Particles in this type of flow experience a superposition of wave orbital motions, Stokes drift, convergence zones, and small-scale turbulence, all of which vary with depth and time. Capturing this physics is essential for realistic models of vertical transport. From the perspective of particle transport, this environment presents several challenges.

1.2 *Flow-particle dynamics*

Adding to the complexity of the free-surface turbulent boundary layer flow, small particles suspended in a flow do not in general move as perfect tracers once their density differs from the fluid, their size is comparable to the characteristic flow scales, or their inertia is not negligible (Balachandar and Eaton, 2010; Brandt and Coletti, 2022). Even when the particle density is close to that of the surrounding fluid, finite size and inertia cause departures from fluid trajectories, which can give rise to several forms of forcing on the particle that influence its motion.

More generally, the motion of a small spherical particle of diameter d_p, mass m_p, and density ρ_p in a nonuniform, unsteady flow with velocity $\mathbf{u}_f(\mathbf{x}_p, t)$ and density ρ_f is described by the Maxey-Riley equation (Maxey and Riley, 1983), ignoring Faxén corrections and lift forces. Neglecting two-way coupling (i.e., the flow influences the particle motion but not the other way), the total force on the particle following its own trajectory can be written as a sum of forces due to drag, gravity and buoyancy, fluid acceleration, added mass, and Basset history force:

$$
\begin{aligned}
m_p \frac{\mathrm{d}\mathbf{u}_p}{\mathrm{d}t} =& \frac{1}{2} C_D \rho_f A_p |\mathbf{u}_f - \mathbf{u}_p| (\mathbf{u}_f - \mathbf{u}_p) + (m_p - m_f)\mathbf{g} \\
&+ m_f \frac{\mathrm{D}\mathbf{u}_f}{\mathrm{D}t} + C_m m_f \left(\frac{\mathrm{D}\mathbf{u}_f}{\mathrm{D}t} - \frac{\mathrm{d}\mathbf{u}_p}{\mathrm{d}t} \right) + \frac{3}{2} d_p^2 \sqrt{\pi \rho_f \mu} \int_0^t \frac{\partial(\mathbf{u}_f - \mathbf{u}_p)}{\partial \tau} \frac{\mathrm{d}\tau}{\sqrt{t-\tau}},
\end{aligned}
\tag{1.1}
$$

where m_f is the displaced fluid mass, $\mathbf{u}_p$ is the particle velocity, C_D is the particle drag coefficient, A_p is the projected particle area facing the flow, $\mathbf{g}$ the gravitational acceleration vector, C_m is the added mass coefficient ($C_m = 1/2$ for spheres), and the fluid dynamic viscosity is μ. The operators $\mathrm{d}/\mathrm{d}t$ and $\mathrm{D}/\mathrm{D}t$ denote particle-following and fluid-following time derivatives, respectively. The velocities $\mathbf{u}_p(t)$ and $\mathbf{u}_f(\mathbf{x}_p, t)$ are evaluated at the particle centroid $\mathbf{x}_p$ and the coordinate system in z is positive upward. In (1.1), the right-hand side includes the forces due to drag, buoyancy, fluid acceleration, added mass, and history, respectively.

The relative importance of the force terms in (1.1) depends on the properties of both the particle and the surrounding flow. In particular, the appropriate drag model depends primarily on the particle Reynolds number, while the validity of the point-particle approximation depends on the particle size relative to the characteristic length scales of the flow. The Stokes-flow approximation is appropriate only when the particle Reynolds number is sufficiently small. For finite particle Reynolds numbers, nonlinear drag must be considered, whereas finite-size effects may require additional corrections to the point-particle description (Clift et al., 2005; Balachandar and Eaton, 2010; Brandt and Coletti, 2022). We therefore define the nondimensional parameters used to identify the relevant particle-flow regime and to assess which physical effects are expected to influence the particle dynamics.

1.2.1 Nondimensional numbers

The particle Reynolds number Re_p characterizes the relative importance of fluid inertial and viscous effects in the flow around the particle and is defined as

$$Re_p = \frac{d_p \left|\mathbf{u}_f - \mathbf{u}_p\right|}{\nu}, \tag{1.2}$$

where d_p is the particle characteristic length scale, $\mathbf{u}_f - \mathbf{u}_p$ is the slip velocity between the fluid and the particle, and ν is the fluid kinematic viscosity. For spherical particles, d_p is the particle diameter.

In a quiescent fluid, the fluid velocity $\mathbf{u}_f$ is zero and the slip velocity is equal to the particle's terminal rise or settling velocity w_0. Therefore, the Reynolds number can be written as

$$Re_p = \frac{d_p w_0}{\nu}. \tag{1.3}$$

In a turbulent flow, however, Re_p should be evaluated using the local, instantaneous slip velocity.

The particle Reynolds number determines the flow regime around the particle and therefore the drag law used to model the drag force. For a spherical particle, the drag force can generally be written as the first term in the right-hand side in equation (1.1). In the creeping-flow regime, $Re_p \ll 1$, viscous forces dominate and

$$C_D = \frac{24}{Re_p}. \tag{1.4}$$

Substitution into the general drag expression gives the linear Stokes drag,

$$\mathbf{F}_D = 3\pi\mu d_p(\mathbf{u}_f - \mathbf{u}_p), \tag{1.5}$$

where μ is the fluid dynamic viscosity. For moderate particle Reynolds numbers, the Schiller-Naumann correlation is commonly used:

$$C_D = \frac{24}{Re_p}\left(1 + 0.15 Re_p^{0.687}\right), \tag{1.6}$$

which is applicable over the range of approximately $Re_p \lesssim 800$ (Clift et al., 2005). Many particles observed at the ocean surface occupy an intermediate Re_p regime, where both inertial and viscous forces are significant. Observations from Pacific net tows, for instance, indicate Re_p values extending up to ~ 300 for particles ranging from 0.5 to 30 mm (DiBenedetto et al., 2023).

Finite-size particles, whose diameters are non-negligible relative to the smallest relevant flow scales, can depart from tracer behavior even in the absence of a density difference with the fluid. This effect is parametrized by the relative particle size Sz, defined as the ratio between the characteristic particle length scale d_p (the particle diameter for spherical particles) and the characteristic length scale of the fluid, ℓ_f. In turbulent flows, the relevant fluid length scale is often the Kolmogorov length scale ℓ_η, which characterizes the smallest turbulent motions and the scale at which viscous dissipation becomes important:

$$Sz = \frac{d_p}{\ell_\eta}. \tag{1.7}$$

When $Sz \ll 1$, the particle is much smaller than the smallest turbulent eddies, and the fluid velocity varies only weakly across its surface. Therefore, the particle can often be treated as a point particle, provided that the particle Reynolds number Re_p is sufficiently small. When $Sz \gtrsim 1$, the particle diameter is comparable in size to, or larger than, the Kolmogorov length scale and consequently samples significant velocity variations across its own size. As a result, the particle cannot be modeled as a point particle because it averages the fluid velocity and pressure over their volume and cannot respond instantaneously to rapid, spatially localized changes in the flow, leading to finite-size effects such as *spatial filtering* (Qureshi et al., 2007; Calzavarini et al., 2009; Salmon et al., 2025). This "filtering" attenuates high-frequency velocity fluctuations, reduces the variance of particle velocity fluctuations relative to that of the fluid, and increases the velocity fluctuation correlation time scale associated with particle motion (Reeks, 1977). At sufficiently large particle Reynolds numbers, finite-size particles may also develop wakes and vortex shedding (Fornari et al., 2016a). In addition, the added-mass and history forces may become increasingly important (Guseva et al., 2016; Li et al., 2023). Microplastics in the ocean typically fall in the range $Sz \sim O(1\text{–}10)$ (DiBenedetto, 2026) while laboratory experiments with marginally buoyant particles in free-surface turbulence have explored ranges of $Sz \sim O(1\text{–}100)$ (Salmon et al., 2025).

Particle buoyancy introduces an additional scale through the quiescent rise (or settling) velocity w_0, which characterizes motion in a quiescent fluid. Analogous to the Rouse number in sediment transport (Rouse, 1937), the balance between buoyancy-driven drift and turbulence-driven mixing in the vertical is expressed by the rise velocity parameter (or floatability parameter) which is the ratio:

$$Rv = \frac{w_0}{w_{\text{rms}}}, \tag{1.8}$$

where w_{rms} is a the characteristic vertical turbulent velocity scale. Small values mean turbulence can move particles vertically faster than they can rise or sink under gravity; large values mean buoyancy dominates their vertical motion. In the ocean mixed layer, near-neutrally buoyant particles experience a flow regime where buoyancy and turbulence are of comparable strength since $Rv \sim O(10^{-1}\text{–}1)$ (Chor et al., 2018b).

Finally, the particle inertia can be quantified from the equation of motion for a particle in unsteady flow. Rearranging equation (1.1) yields:

$$\frac{\mathrm{d}\mathbf{u}_p}{\mathrm{d}t} = \frac{1}{\tau_p}(\mathbf{u}_f - \mathbf{u}_p) + \beta\frac{\mathrm{D}\mathbf{u}_f}{\mathrm{D}t} + (1-\beta)\mathbf{g} + \mathcal{H}\int_0^t \frac{\partial(\mathbf{u}_f - \mathbf{u}_p)}{\partial\tau}\frac{\mathrm{d}\tau}{\sqrt{t-\tau}}, \tag{1.9}$$

where τ_p is the particle response (or relaxation) time, $\beta = (1 + C_m)/(\rho_p/\rho_f + C_m)$ is the density parameter, and $\mathcal{H} = 3d_p^2\sqrt{\pi\rho_f\mu}/2(\rho_p/\rho_f + C_m)$. The β determines the relative importance of fluid acceleration and buoyancy in the particle equation of motion, with $\beta = 1$ for neutrally buoyant particles, $\beta < 1$ for heavy particles, and $\beta > 1$ for buoyant particles.

The particle response time characterizes how fast the particle responds to flow changes and is typically calculated by incorporating both drag and added-mass effects as

$$\tau_p = \frac{4d_p^2(\rho_p/\rho_f + C_m)}{3\nu C_D Re_p}, \tag{1.10}$$

but it can also be related to the still-water rise velocity w_0 as

$$\tau_p = \frac{w_0}{(1-\beta)g}. \tag{1.11}$$

However, these formulations are applicable to spherical point particles and become increasingly difficult to implement when particles exhibit non-spherical shapes, have dimensions comparable to the characteristic flow scales, or are neutrally buoyant, as the latter prevents the definition of a well-defined slip velocity. Some alternatives exist to estimate the response time of nonspherical particles that depend on the particle dimensions and make simplifications about the orientation-dependent drag that the particles experience (Shapiro and Goldenberg, 1993; Zhao et al., 2015).

The ratio of a particle response time τ_p to a characteristic timescale of the flow (Kolmogorov time scale τ_η for turbulent flows) defines the Stokes number

$$St = \frac{\tau_p}{\tau_\eta}. \tag{1.12}$$

The Stokes number quantifies particle inertia relative to turbulent timescales. When $St \ll 1$, particles closely follow the fluid motion; when $St \sim O(1)$, their inertia leads to significant deviations; and when $St \gg 1$, particles barely respond to turbulent fluctuations. In this range particles have sufficient inertia to depart from fluid streamlines. For realistic oceanic flow and particle conditions, DiBenedetto (2026) estimates a Stokes number range of $St \sim O(10^{-4}$–$10^{-1})$ while laboratory experiments involving waves and free-surface turbulence have examined ranges of approximately $St \sim O(10^{-2}$–$10^{-1})$ (Alsina et al., 2020; Salmon et al., 2025). These values indicate weak particle inertia, and microplastics are therefore often approximated as tracers. Nevertheless, even when $St \ll 1$, small deviations from fluid trajectories can accumulate over sufficiently long times and affect particle transport (Ouellette et al., 2008).

To further characterize the vertical transport, we introduce the vertical turbulent Schmidt number, which measures the relative efficiency of turbulent momentum transport and particle transport, analogous to the Prandlt number for heat. It is defined as:

$$Sc_t = \frac{\nu_t}{K}, \tag{1.13}$$

where ν_t is the turbulent momentum diffusivity. Thus, $Sc_t = 1$ implies comparable momentum and particle diffusivities, whereas $Sc_t < 1$ and $Sc_t > 1$ indicate, respectively, more efficient and less efficient particle dispersion than momentum transport. In the present study, Sc_t is relevant because it directly determines the particle diffusivity through $K = \nu_t / Sc_t$ and therefore controls the predicted vertical distribution of buoyant particles in unsteady flows. The turbulent Schmidt number depends on the particle properties, flow regime, concentration, and method used to infer it. Reported values for tracers and non-tracers in many environmental-flow studies range between 0.1 and 4 (for a thorough review, see Gualtieri et al., 2017; Chauchat et al., 2022) although $Sc_t = 1$ is commonly adopted as a baseline assumption when the particle diffusivity is unknown (Kukulka and Brunner, 2015; Onink et al., 2022).

1.2.2 Finite-size particle behaviors

Although these non-dimensional parameters help identify the relevant particle-flow regime, they do not provide a complete description of particle behavior. Additional mechanisms can arise through the coupled effects of inertia, buoyancy, finite size, particle shape, and flow. Thus, the non-dimensional parameters are best viewed as diagnostic tools that help identify the relevant particle-flow regime and organize the possible mechanisms of particle transport.

Inside an eddy, particles tend to accumulate in different regions based on their relative density with respect to the fluid, producing strong small-scale clustering and voids even for statistically homogeneous initial conditions (Maxey, 1987; Squires and Eaton, 1991; Aliseda et al., 2002). This “preferential concentration” (or inertial clustering) is causes by the particle inertia and is thus dependant on St. As St increases, heavy particles tend to be expelled from vortices and accumulate in regions of high strain and low vorticity whereas light particles accumulate in regions of high vorticity and low strain (Balachandar and Eaton, 2010). When $St \sim O(1)$, the settling velocity of heavy particles is enhanced due to “fast-tracking” or “preferential sweeping” since it oversamples down-moving flow (Wang and Maxey, 1993; Dávila and Hunt, 2001; Aliseda et al., 2002).

Conversely, heavy particles can oversample up-moving flows. When $Rv \sim O(1)$, particles cut through vortices moving through up- and down-flow, but they take more time to move through the up-moving part of the flow (Murray, 1970). This behavior can only be captured when nonlinear drag forces are considered in simulations (Wang and Maxey, 1993) whereas preferential sweeping dominates in linear drag regimes (Good et al., 2014). This behavior can modulate settling velocity and depend on St, Rv for small particles but can also depend on Sz (Good et al., 2014). Surface waves can also produce a net vertical effect on particles through preferential sampling of the oscillatory motion. As particles rise or settle, they spend more time in the part of the wave orbit that reinforces their motion, so their average vertical transport is altered in a way that is often described as a vertical Stokes drift (Santamaria et al., 2013; DiBenedetto et al., 2022). Even though this mechanism is kinematic, inertia can strengthen or weaken it by changing the orbital response of the particle (Clark et al., 2020).

Whenever particles have a non-zero mean drift (upward or downward), their trajectories cross eddies. That is, as they drift through the flow, they cross fluid pathlines and their turbulent velocity fluctuations decorrelate more rapidly than those of fluid tracers. This *"crossing trajectories"* effect was first formalized for inertialess, heavy particles in atmospheric turbulence by Yudine (1959) and Csanady (1963), who showed that as Rv increases, particle velocity fluctuations decorrelate faster than those of the fluid. In water, several studies confirmed that a finite settling or rise speed w_d reduces particle dispersion compared to fluid tracers in the same flow (Reeks, 1977; Squires and Eaton, 1991; Wetchagarun and Riley, 2010).

1.3 *Wave, turbulence, and particle effects on vertical transport*

Recall from Section 1.0.2 that vertical particle transport in a boundary layer can be characterized by two parameters: the particle turbulent diffusivity and the particle drift velocity, which corresponds to a rise velocity for buoyant particles and a settling velocity for heavy particles. Existing models commonly represent this transport using a parameterized diffusivity together with a prescribed particle rise or settling velocity. However, estimating these transport parameters in the near-surface region remains difficult to predict because waves, wave breaking, and Langmuir circulation strongly influence the local turbulence. The problem is further complicated by the fact that finite-size particles do not necessarily move with the flow, as seen in section 1.2. In the following section, we examine how the flow and particle characteristics introduced above influence the particle turbulent diffusivity and drift velocity.

The turbulent diffusivity depends on particle properties and the way particles sample the flow velocity fluctuations. When particle properties differ from those of the surrounding fluid, particles may not behave as tracers, making the assumption $Sc_t \approx 1$ inaccurate. Reported values of Sc_t for non-tracer particles vary widely across environmental flows, with both enhanced and reduced particle dispersion relative to momentum transport (Gualtieri et al., 2017). The influence of particle properties can be illustrated using results from small, heavy particles ($Sz \approx 0$) in homogeneous isotropic turbulence. For example, particle diffusivity decreases relative to that of fluid tracers as Rv increases because the crossing-trajectories effect shortens the correlation time of particle velocity fluctuations, even in the absence of particle inertia (Csanady, 1963; Snyder and Lumley, 1971; Wells and Stock, 1983).

In contrast, particle inertia can increase the velocity correlation time and enhance particle diffusivity through spatial filtering (Reeks, 1977; Squires and Eaton, 1991; Wetchagarun and Riley, 2010; Qureshi et al., 2007). Similar results were found for buoyant particles in isotropic turbulence (Gopalan et al., 2008). Experiments with finite-size floating particles in free-surface turbulence, however, found that increasing particle size reduced velocity fluctuations while increasing velocity correlation times, resulting in only a weak dependence of diffusivity on Sz (Salmon et al., 2025). Waves can further influence particle diffusivity indirectly through turbulence distortion (Teixeira and Belcher, 2002; Qiao et al., 2016), breaking waves (Terray et al., 1996; Gerbi et al., 2009; Sullivan and McWilliams, 2010) and Langmuir turbulence (Farmer and Li, 1994; Skyllingstad and Denbo, 1995; McWilliams et al., 1997; D'Asaro, 2014).

The particle drift velocity is affected by both particle properties and flow conditions. It may also be particularly sensitive to waves and coherent structures because these processes can modify the particle-fluid relative motion directly. Buoyant particles can accumulate in zones of surface convergence located above downwelling regions generated by Langmuir circulation (Chor et al., 2018a; Yang et al., 2014) and can also become trapped in vortical structures through inertial effects (Aliseda and Lasheras, 2011), reducing their rise velocity. For heavy particles, Langmuir circulation has been shown to reduce the mean settling velocity by modifying their interaction with coherent turbulent structures (Noh et al., 2006; Chamecki et al., 2019). In wavy flows, particle inertia can also produce preferential sampling of the wave orbital motion, generating a net vertical drift that modifies the settling velocity (Santamaria et al., 2013; DiBenedetto et al., 2022). Surface waves can also directly modulate particle rise velocities (Clark et al., 2020; DiBenedetto et al., 2022).

The particle Reynolds number provides another mechanism for modifying the drift velocity. Nonlinear drag can reduce the drift of particles with finite Re_p. Good et al. (2014) showed through experiments and simulations that heavy-particle settling can be reduced under linear drag, through the loitering effect, as well as under nonlinear drag. Reductions in the mean settling or rise velocity have been reported for near-neutrally buoyant particles (Byron, 2015), slightly heavy particles (Fornari et al., 2016b), and bubbles (Ruth et al., 2021; Liu et al., 2024). Unsteady hydrodynamic forces, discussed in Section 1.2, can further reduce particle drift (Li et al., 2023). Consequently, the rise velocity measured in still water is not necessarily an accurate representation of the mean particle drift in the ocean surface boundary layer. Identifying the mechanisms that reduce particle drift velocity requires co-located measurements of particle and fluid velocities at the particle centroid, which are not available in the present study. We therefore do not investigate wave- and turbulence-induced modifications of the rise velocity.

Taken together, the vertical particle transport cannot, in general, be characterized by tracer diffusivity and the quiescent rise velocity alone. Waves, turbulence and finite-size particle dynamics can modify both the dispersive and mean-drift components of transport. However, it remains unclear how these mechanisms combine for buoyant, finite-size particles in wavy turbulent flows.

1.4 *Structure of the dissertation*

The three chapters in this dissertation aim to build on the current understanding of the transport in a wind-driven, free-surface boundary layer. The main problem is the inherently multiscale and complex interactions between waves and turbulence, which may contribute to near-surface mixing and transport (D'Asaro, 2014; Kukulka and Brunner, 2015; Skyllingstad and Denbo, 1995; McWilliams et al., 1997). Therefore, the wave-coherent motion must be isolated from the broadband turbulent background, but that separation is difficult because the two processes overlap in space, time, and frequency, and may interact nonlinearly (Jiang et al., 1990; Trowbridge, 1998; Gerbi et al., 2008; Young and Webster, 2018; Bian et al., 2018). This makes wave-turbulence separation our first step.

The central question of this dissertation is the following: **how do waves, turbulence, and particle properties together reshape the vertical motion of nearly buoyant, finite-sized particles in a free-surface boundary layer, and how should those effects be represented in models of upper-ocean transport?** In order to answer this, we break down this problem into three questions:

- How can wave motion be separated from turbulence when the two overlap in frequency and interact nonlinearly?

- How do near-neutrally buoyant particle characteristics modulate their vertical transport in a wavy and turbulent boundary layer?

- How do waves and turbulence contribute separately to near-neutrally buoyant particle transport in a free-surface boundary layer?

Because waves and turbulence are simultaneously present in the measurements, the first requirement is to identify and separate their contributions. Therefore, we first attempt to separate waves and turbulence, starting from Eulerian measurements of fluid velocity were both are present. In **Chapter 2**, we introduce a dynamic mode decomposition-based algorithm for wave-turbulence separation. We formulate DMD in a way that is suitable for analyzing Eulerian time series of any quantity, not only velocity measurements. We discuss how to identify wave-coherent modes in the presence of broadband turbulence, and validate the method using synthetic, field, and laboratory data. The resulting decomposition is used in the subsequent chapter of this thesis to interpret vertical-velocity statistics in wavy flows. This addresses an important problem in transport, because any decomposition that mixes wave and turbulence contributions will blur the mechanisms that actually control transport.

Then, we study the vertical transport of finite-sized, nearly buoyant particles under waves and turbulence. For these particles, the relevant quantities are not only the mean rise or settling velocity, but also the vertical diffusivity, and the way these quantities change when particles do not behave as perfect tracers (Taylor, 1922; Csanady, 1963; Squires and Eaton, 1991; Wang and Maxey, 1993; Kukulka et al., 2012; Onink et al., 2022). Lagrangian descriptions of transport are especially useful because they follow individual particles and directly measure how buoyancy, inertia, size, and shape modify dispersion, while Eulerian descriptions are better suited to mean concentration profiles and bulk transport closures (Davis, 1983; Rouse, 1937; Chamecki et al., 2019)

The third and fourth chapters build on this distinction: one focuses on Eulerian vertical diffusivity estimates and their relation to observed particle profiles, while the other examines Lagrangian statistics to quantify how waves and turbulence alter particle autocorrelation, dispersion, and effective transport. In **Chapter 3** we look into the transport of spherical and non-spherical particles in a free-surface boundary layer. We measure their vertical diffusivity and effective rise velocity directly from particle trajectories and compare them to current models that rely on Eulerian measurements and equilibrium assumptions. We also quantify the influence of particle properties on diffusivity and effective rise velocity. Then, in **Chapter 4** we investigate how waves and turbulence modulate the Lagrangian vertical velocity statistics. We develop a simple parametric model for the Lagrangian autocorrelation that captures the combined influence of waves, turbulence, quantify their respective variances and integral time scales, and examine how these combine to determine effective diffusivities.

Finally, **Chapter 5** synthesizes the main findings, emphasizes their implications for parameterizing vertical transport of buoyant particles in the ocean surface boundary layer, and outlines directions for future work. Together, these chapters aim to advance our understanding of how waves, turbulence, and particle properties jointly control the vertical fate of nearly buoyant particles at the ocean surface, and to provide tools for more accurate modeling of their transport in environmental and geophysical flows.

Chapter 2

WAVE AND TURBULENCE SEPARATION USING DYNAMIC MODE DECOMPOSITION

This chapter reproduces material published in: Chávez-Dorado, J., Scherl, I., & DiBenedetto, M. (2025). Wave and Turbulence Separation Using Dynamic Mode Decomposition. Journal of Atmospheric and Oceanic Technology, 42(5), 509-526.

2.1 *Introduction*

As observational advances increase the amount of ocean data available (Smith et al., 2019; Rosa et al., 2021), effectively interpreting and using this information, both in post-processing and real-time analysis, is imperative for gaining insights into the dynamics of the ocean. One ongoing challenge is the interpretation of fluctuating data that is influenced by both turbulence and surface gravity waves. This is common in data obtained from the ocean surface and from the coastal ocean where both turbulence and surface waves are expected to be strong. Separating the turbulence and wave fluctuations in a signal is important for a variety of analyses: e.g., isolating the turbulence fluctuations in any signal is necessary for characterizing the turbulence Reynolds stress or for estimating a scalar eddy covariance flux. And isolating the wave motion is necessary e.g., for quantifying wave energy or for wave energy control strategies (Li et al., 2012; Perez et al., 2020). We refer to this separation process as *wave-turbulence decomposition*.

The difficulties associated with wave-turbulence decomposition lie in the overlapping frequency domains where waves and turbulence exist—and that both can manifest as broadband signals with correlation in space and time. Even asserting that these signals can be effectively decomposed is an assumption, given the nonlinear interactions that can occur between waves and turbulence (Jiang et al., 1990; Magnaudet and Thais, 1995; Guo and Shen, 2013). Over the years, numerous methods have been developed to tackle this problem (Benilov et al., 1974; Jiang et al., 1990; Thais and Magnaudet, 1995; Trowbridge, 1998; Williams et al., 2003; Gerbi et al., 2008; Huang and Wu, 2008; Young and Webster, 2018; Bian et al., 2018). However, the various methods are usually adapted to the specific data at hand (Gerbi et al., 2008; Feddersen and Williams, 2007; Jiang et al., 1990), involve restrictive assumptions (e.g., (Benilov et al., 1974; Bricker and Monismith, 2007)), and/or require multiple and often complex synchronized measurements (Trowbridge, 1998; Doron et al., 2001; Feddersen and Williams, 2007). As a result, we still lack an effective, universal technique for decomposing a general time series.

Our goal is to develop a decomposition method that can be applied to a time series of any type of data. However, for simplicity we will consider a velocity time series as it is the most commonly decomposed signal in this context. Consider the velocity decomposition

$$u(x_i, t) = \langle u(x_i) \rangle + \tilde{u}(x_i, t) + u'(x_i, t), \tag{2.1}$$

where u is the instantaneous horizontal velocity, $\langle u \rangle$ is the time average, $\tilde{u}$ is the wave-orbital velocity and u' is the turbulence velocity fluctuation. In two-dimensions, the result of Reynolds-averaging the Navier-Stokes equations with this decomposition is the Reynolds shear stress:

$$-\frac{\tau_{\mathrm{sh}}}{\rho_f} = \langle \tilde{u}\tilde{w} \rangle + \langle \tilde{u}w' \rangle + \langle u'\tilde{w} \rangle + \langle u'w' \rangle. \tag{2.2}$$

The first term on the right hand side is identically zero for irrotational waves described by linear wave theory but can be non-zero if the coordinate system is rotated, a common source of corrupted Reynolds stress measurements (Trowbridge, 1998). The second and third terms are zero if there are no interactions between the waves and turbulence. The fourth term is the turbulence Reynolds shear stress, which is the only non-zero term as long as the aforementioned assumptions regarding linear wave theory and wave-turbulence interaction hold.

Spectral filtering techniques (Benilov et al., 1974; Bricker and Monismith, 2007; Gerbi et al., 2008; Young and Webster, 2018) are able to estimate bulk turbulence quantities like the Reynolds stress with some accuracy, but they do not allow for a time-series reconstruction of the decomposed velocity signals because they are applied to the velocity power spectrum. Methods based on nonlinear stream functions (Dean, 1965; Jiang et al., 1990; Thais and Magnaudet, 1995, 1996) allow for a time-resolved separation with fewer assumptions but only work for specialized scenarios. More recent approaches involve dimensionality-reduction techniques (Huang et al., 1998, 2009; Bian et al., 2018) that make use of mode decomposition to capture the coherent, oscillating nature of waves. However, it is common for these methods to remove turbulence energy in excess from the wave frequency range. In addition, these methods often require tuning parameters that lack a clear physical intuition. Nevertheless, dimensionality reduction techniques such as proper orthogonal decomposition (POD) (Lumley, 1967), spectral proper orthogonal decomposition (SPOD) (Towne et al., 2018; Schmidt and Colonius, 2020), and dynamic mode decomposition (DMD) (Rowley et al., 2009; Schmid, 2010) have become increasingly popular in fluid dynamics research due to their adaptability and effectiveness in extracting physically interpretable information from complex data. For example, POD has been used in pattern recognition in chaotic flows (Albidah et al., 2021), flow control (Gordeyev and Thomas, 2013), and unsteady, high-Reynolds-number wake flows (Durgesh and Naughton, 2010) and SPOD has been employed in diverse flows such as boundary layers (Tutkun and George, 2017), mixing layers (Braud et al., 2004), wakes (Araya et al., 2017), and jets (Heidt and Colonius, 2023), among others. Similarly, DMD is widely used in the study of wakes (Schmid, 2010), jets (Schmid, 2010; Seena and Sung, 2011; Schmid, 2011; Semeraro et al., 2012), instabilities (Duke et al., 2012; Grilli et al., 2012), and oscillations (Seena and Sung, 2011; Massa et al., 2012; Albidah et al., 2021). However, these methods have yet to be applied to wave-turbulence decomposition, a problem for which they may be well-suited. DMD shows promising filtering characteristics for an accurate wave-turbulence decomposition algorithm for single-point velocity measurements because it is designed to capture the time dynamics of coherent structures present in a signal.

Our approach is to develop a decomposition method that is as general as possible. We seek a signal-agnostic framework, capable of handling one-dimensional time-series data for a broad spectrum of flow parameters. Our methodology does not rely on severe assumptions about wave nor turbulence dynamics, making it adaptable to a variety of ocean and environmental datasets. Thus, we will explore the effectiveness of DMD in a variety of datasets: synthetic data generated with no wave-turbulence interactions, field data collected in a swell-dominated bottom boundary layer, and laboratory data collected in a surface boundary layer under wind-waves.

2.2 *Background*

2.2.1 Wave-turbulence decomposition

Wave-turbulence decomposition is a longstanding challenge that has been approached in a variety of ways. Simpler methods like moving average and band-pass filters are often used (Foster, 1997; Smyth et al., 2002; Williams et al., 2003; Zhu et al., 2016) due to their ease of use and time-resolved output; however, these filters do not distinguish the waves from the turbulence in the overlapping frequency range, resulting in the elimination of turbulent energy.

Many spectral decomposition techniques have been developed that can estimate the Reynolds stress without allowing for a time-series reconstruction; these methods often rely on the correlation between two separate measurements. For example, Benilov et al. (1974) proposed a linear filtration technique that leverages coherence between the pressure and velocity spectra. Similarly, Trowbridge (1998) and Shaw and Trowbridge (2001) proposed a method that leverages the coherence between two synchronized velocity measurements with a finite spacing. With only one velocity measurement, Bricker and Monismith (2007) proposed a method that linearly filters the energy spectrum by assuming an inertial subrange with a $-5/3$ slope. Whereas Gerbi et al. (2008) proposed fitting the measured spectrum to an empirical spectrum model to separate the waves and turbulence. While these methods are also frequently used due to their relative simplicity, they assume no wave-turbulence interactions and do not directly allow for a reconstructed time series (unless further approximations are made, e.g. see Cowherd et al. (2021)). Additionally, some of the methods require multiple synchronized measurements which further restricts their use.

Some researchers sought a more rigorous characterization of the interaction of wave and turbulence by using the nonlinear wave stream function (Dean, 1965), which imposed fewer assumptions and allowed for a time reconstruction of the filtered signal. Jiang et al. (1990) developed a method based on this work that consists of solving, in a least squares sense, the stream functions at the free surface. Similarly, the triple decomposition method from Thais and Magnaudet (1995, 1996) also used a stream function to decompose the instantaneous velocity into turbulent fluctuation, irrotational wave, and rotational wave components. Although these methods allow the construction of separate wave and turbulent velocity time series, they are most well-suited to laboratory conditions where dispersive effects can be neglected (Thais and Magnaudet, 1995).

More recently, data-driven dimensionality-reduction techniques have been proposed to separate waves and turbulence. Ensemble Empirical Mode Decomposition (EEMD) is the foundation of the method developed by Huang and Wu (2008). It is based on the empirical mode decomposition (EMD), which decomposes the signal into intrinsic mode functions (IMFs), defining a basis dictated by the data (Huang et al., 1998). While successful at separating a time series into different components, the method suffers because a single IMF can contain several oscillatory modes or a single mode can be split into several IMFs. Huang and Wu (2008) proposed the EEMD to overcome this issue by introducing noise in the original signal in order to properly organize the different scales in the time series. The limitations of this improvement are that a large number of iterations are needed to remove the effects of the noise and obtain an accurate decomposition. In addition, ensemble-averaging may affect the physical significance of the IMFs by artificially redistributing some energy among the IMFs. More recently, Bian et al. (2018) proposed the synchrosqueezed wavelet transform (SWT)-based method (Daubechies et al., 2011; Thakur et al., 2013), which decomposes the signal into a number of components separated in the time-frequency plane. This method forces the data to conform to a basis set determined *a priori* and tends to underestimate the turbulence in the wave frequency range. The EEMD and SWT are modal decomposition techniques that can be applied to a single time series and allow for a time-resolved signal reconstruction. For these reasons, we use them to compare the outputs of our DMD-based method in section 2.5.

To summarize, traditional decomposition methods applied in spectral space are limited to scenarios with no wave-turbulence interactions, often require more specific assumptions and do not directly give a time-series reconstruction. To address these limitations, methods based on modeling waves using stream functions were developed, but they are only effective under ideal conditions that are not commonly found in nature. Finally, newer modal decomposition methods have been successful in generating a time-resolved filtered signal, but they can have a significant impact on the turbulence in the wave frequency range.

2.2.2 Modal decomposition of flow data

In this section, we present a summary of relevant modal decomposition algorithms; for a more in-depth reference, see Schmid (2022). Modal decomposition refers to the identification and separation of *modes*, or pattern, in data from a dynamical system. This type of decomposition is favorable because the general motion of a system, even nonlinear, nonstationary systems, can be approximated by a linear superposition of its modes. In the context of fluid dynamics, modal decomposition refers to the identification and separation of features in flow data (e.g., generated from Particle Image Velocimetry). The singular value decomposition (SVD) is the basis for the implementation of several dimensionality-reduction techniques such as proper orthogonal decomposition (POD) (Lumley, 1967) and dynamic mode decomposition (DMD) (Schmid, 2010).

Singular value decomposition (SVD) and proper orthogonal decomposition (POD)

The SVD decomposes a matrix, $\mathbf{M} \in \mathbb{R}^{m \times n}$ into the product of three matrices

$$\mathbf{M} = \mathbf{U}\mathbf{\Sigma}\mathbf{V}^T,$$

where $\mathbf{U} \in \mathbb{R}^{m \times m}$ and $\mathbf{V} \in \mathbb{R}^{n \times n}$ are unitary matrices, and $\mathbf{\Sigma} \in \mathbb{R}^{m \times n}$ is a diagonal matrix with non-negative real values. The singular values that make up the diagonal values $\sigma_k \in \mathbf{\Sigma}$ are in descending order and weight the modes. In other words, they are ordered based on how much of the total energy of the original data matrix they possess. The columns of $\mathbf{U}$ (expressed as $\mathbf{u}_k$) and the columns of $\mathbf{V}$ (expressed as $\mathbf{v}_k$) are known as the left singular vectors and right singular vectors of $\mathbf{M}$, respectively. A reduced-order approximation of the matrix $\mathbf{M}$ can be achieved by truncation as

$$\mathbf{M}_r \approx \sum_{k=1}^{r} \sigma_k \mathbf{u}_k \mathbf{v}_k^T,$$

where $\mathbf{M}_r$ is a rank r approximation of $\mathbf{M}$ using the $r \leq \min(m, n)$ most energetic singular modes.

The POD is simply an SVD applied to a specifically constructed $\mathbf{M}$ matrix. It was introduced in fluid mechanics by Lumley (1967, 2007), Sirovich (1987a,b,c), and Aubry et al. (1988). The matrix $\mathbf{M}$ is constructed as follows: given n snapshots of flow data in a discrete spatial grid of m points, each consecutive snapshot is reshaped into a corresponding column vector of a data matrix, $\mathbf{M} \in \mathbb{R}^{m \times n}$, where the k-th column of $\mathbf{M}$, denoted as $\mathbf{x}_k$, contains all the spatial data of a singular snapshot at time $k\Delta t$ or, similarly, each row contains a time series of the flow data at a single point in space (Scherl et al., 2020). Thus we have,

$$\mathbf{M} = \begin{bmatrix} | & | & | & & | \\ \mathbf{x}_1 & \mathbf{x}_2 & \mathbf{x}_3 & \dots & \mathbf{x}_n \\ | & | & | & & | \end{bmatrix}.$$

Dynamic Mode Decomposition (Schmid, 2010) is used to determine the temporal periodicity of coherent structures present in flow data. DMD captures the system dynamics in the eigenvectors (modes) and eigenvalues of an infinite-dimensional linear operator, known as the Koopman operator. DMD can separate system dynamics into modes that evolve over time. Additionally, DMD is tailored to recover oscillating dynamics without any prior knowledge of the system.

To compute DMD, one begins with n time steps of data across m dimensions. Each time step is shaped into a column vector of a present-state data matrix, $\mathbf{X} \in \mathbb{R}^{m \times (n-1)}$ that contains time steps 1 to $n-1$, and a future-state data matrix, $\mathbf{X}' \in \mathbb{R}^{m \times (n-1)}$ that contains time steps 2 to n. Thus we have,

$$\mathbf{X} = \begin{bmatrix} | & | & | & & | \\ \mathbf{x}_1 & \mathbf{x}_2 & \mathbf{x}_3 & \dots & \mathbf{x}_{n-1} \\ | & | & | & & | \end{bmatrix} \quad \text{and} \quad \mathbf{X}' = \begin{bmatrix} | & | & | & & | \\ \mathbf{x}_2 & \mathbf{x}_3 & \mathbf{x}_4 & \dots & \mathbf{x}_n \\ | & | & | & & | \end{bmatrix}.$$

Similar to POD, the k-th column of either $\mathbf{X}$ or $\mathbf{X}'$, denoted as $\mathbf{x}_k$, contains all the data of a single time step at time $k\Delta t$ or, similarly, each row contains a time series of the data for a single dimension. The DMD algorithm attempts to find the best-fit linear operator $\mathbf{A} : \mathbf{X} \mapsto \mathbf{X}' \in \mathbb{R}^{m \times m}$

that advances the current state of the system, $\mathbf{X}$, one time step into the future, $\mathbf{X}'$, as

$$\mathbf{X}' \approx \mathbf{A}\mathbf{X}. \tag{2.3}$$

The solution to equation 2.3 can be approximated by a matrix $\mathbf{A}$ that minimizes $\|\mathbf{X}' - \mathbf{A}\mathbf{X}\|_F$ as

$$\mathbf{A} = \mathbf{X}'\mathbf{X}^{+}, \tag{2.4}$$

where $\|\cdot\|_F$ is the Frobenius norm, and $\mathbf{X}^{+}$ is the pseudo-inverse of the matrix $\mathbf{X}$. Instead of directly finding the pseudo-inverse, the SVD of $\mathbf{X}$ yields $\mathbf{X} = \mathbf{U}\mathbf{\Sigma}\mathbf{V}^T$ where $\mathbf{U}$, $\mathbf{\Sigma}$, and $\mathbf{V}$ are unitary and, therefore, can be used to express the pseudo-inverse as $\mathbf{X}^{+} = \mathbf{V}\mathbf{\Sigma}^{-1}\mathbf{U}^T$, which yields

$$\mathbf{A} \approx \mathbf{X}'\mathbf{V}\mathbf{\Sigma}^{-1}\mathbf{U}^T, \tag{2.5}$$

where the eigenvalues and eigenvectors (DMD modes) of $\mathbf{A}$ capture the dynamics of the system. The eigenvalues of $\mathbf{A}$ are complex numbers that capture the growth/decay and oscillation of its corresponding DMD modes in their real and imaginary components, respectively. The DMD modes of $\mathbf{A}$ capture the spatial oscillatory patterns.

Typically, calculating $\mathbf{A}$ directly would be computationally intractable. Instead, a truncation of the matrices $\mathbf{U}$, $\mathbf{\Sigma}$, and $\mathbf{V}$ to retain only the first r singular values results in the reduced-rank matrices $\mathbf{U}_r$, $\mathbf{\Sigma}_r$, and $\mathbf{V}_r$ and yields a best-fit linear operator $\tilde{\mathbf{A}} \in \mathbb{R}^{r\times r}$ by projecting $\mathbf{A}$ onto the spatial modes $\mathbf{U}_r$

$$\tilde{\mathbf{A}} = \mathbf{U}_r^T\mathbf{A}\mathbf{U}_r = \mathbf{U}_r^T\mathbf{X}'\mathbf{V}_r\mathbf{\Sigma}_r^{-1}. \tag{2.6}$$

The operator $\tilde{\mathbf{A}}$ has the same discrete-time eigenvalues, $\mathbf{\Lambda}$, as $\mathbf{A}$. The eigenvectors, $\mathbf{W}$, of $\tilde{\mathbf{A}}$ can be calculated as $\tilde{\mathbf{A}}\mathbf{W} = \mathbf{W}\mathbf{\Lambda}$ and converted to the high-dimensional eigenvalues, $\mathbf{\Phi}$, of $\mathbf{A}$, as follows (Tu et al., 2014)

$$\mathbf{\Phi} = \mathbf{X}'\mathbf{V}_r\mathbf{\Sigma}_r^{-1}\mathbf{W}. \tag{2.7}$$

From the leading eigenvalues, $\mathbf{\Lambda}$, and eigenvectors, $\mathbf{\Phi}$, the solution of the system can be recreated as

$$\mathbf{X} = \mathbf{\Phi}\exp(\mathbf{\Omega}t)\mathbf{b} = \sum_{k=1}^{r}\phi_k \exp(\omega_k t) b_k, \tag{2.8}$$

where $\mathbf{\Omega} = \log(\mathbf{\Lambda})/\Delta t$ is the continuous-time eigenvalue of $\mathbf{A}$, and $\mathbf{b} = \mathbf{\Phi}\backslash\mathbf{X}(t_0)$ is the initial condition of the system.

2.3 *Methods*

Figure 2.1 shows a diagram summarizing the algorithm workflow, which is described below. For the method we propose, the input matrix contains a one-dimensional time series of discrete, point-wise flow measurements such as one velocity component (u, v, or w), or other variables like water elevation, scalar concentration, pressure, etc. These measurements are collected at a sampling frequency f_s over a specified duration T, for $N = Tf_s$ total observations in the given time series. Our approach is to use DMD to extract the most coherent features of the signal, which we assume to be the waves, as low-rank structures and subtract them from the raw signal to isolate the turbulence. Although other order-reduction techniques exist, they have limitations. For example, POD identifies correctly the rank of the system but since this method is based entirely on energy (or contained variance), the modes are not temporally orthogonal. In other words, POD can hierarchically rank coherent features in the signal based on their energy content but it cannot offer insights into how these patterns evolve over time. This is not ideal for our problem because we expect waves to be represented as modes that have coherent oscillations in time. In contrast, DMD can separate the dynamics in the system and can identify their temporal oscillation frequency. This allows us to identify a specific frequency per mode that we can associate with wave motion (Kutz et al., 2016).

In frequency space, waves can be narrow-banded when compared with turbulence, but their energy can still span over multiple orders of magnitude in frequency. The broader the wave frequency range, the larger the number of DMD modes will be needed to represent the waves. However, the number of modes that DMD can extract is limited by the rank of the input data matrix. Because we want to extract a range of wave modes, we need to increase the rank of our time series before we apply DMD.

Hence, we propose to address this problem and increase the rank of the input data matrix by constructing a delay embedding of the time-series signals, i.e.,

$$\mathbf{H} = \begin{bmatrix} x_1 & x_2 & x_3 & \dots & \dots & x_n \\ x_2 & x_3 & & & & \vdots \\ x_3 & & & & & \vdots \\ \vdots & & & & & x_{N-2} \\ \vdots & & & & x_{N-2} & x_{N-1} \\ x_m & \dots & \dots & x_{N-2} & x_{N-1} & x_N \end{bmatrix}, \tag{2.9}$$

where $m = N - n$ is the number of time lags, and n is the number of columns. Note that the matrix $\mathbf{H}$ can have multiple rows besides the time-delay process if one has multiple data series (e.g., see Filho and Lopes dos Santos (2019), Fujii et al. (2019), and Lydon et al. (2023)). The introduction of the time delay serves a crucial role in increasing the rank of the data by increasing the "information" content of the matrix (Takens, 1981). Physically, this increase in rank can be analogous to Taylor's frozen turbulence hypothesis, since the time observations of the signals are converted to spatial observations.

In order to filter the signal using DMD, we first need to determine the wave frequency range, the dimension of the time-delayed matrix $\mathbf{H}$, and the rank truncation r. Visual inspection of the signal's power spectrum helps determine the wave frequency range by identifying the points where the wave peak meet the expected turbulence energy spectrum. For the construction of the time-delayed matrix, the number of columns n needs to be large enough to capture the lowest wave frequencies of interest in each row. Based on our sensitivity analysis described below, we find that a good rule of thumb is within the range $n/N \approx [1/3, 1/2]$; however, in our data the decomposition is not as sensitive to this parameter as it is to the rank truncation r, especially given a sufficiently long time series. In general, we suspect that this parameter might require some tuning in order to determine the appropriate dimensions of $\mathbf{H}$. From this new configuration $\mathbf{H}$ of the input data, the present and future-state matrices $\mathbf{X}$ and $\mathbf{X}'$ are constructed as indicated in section 2.2.2 as input for the DMD algorithm. To determine the rank truncation r we perform a POD decomposition of $\mathbf{H} = \mathbf{U}_H \mathbf{\Sigma}_H \mathbf{V}_H^T$ and compute the spectral density of each column $\mathbf{v}_j \in \mathbf{V}_H$ (known as time expansion coefficients) as $\mathbf{C}_j = |\mathcal{F}\{\mathbf{v}_j\}|^2/(f_s N)$, where $\mathcal{F}\{\cdot\}$ is the Fourier transform operator. The vector $\mathbf{C}_j$ contains the energy content at each frequency of the j-th POD mode of $\mathbf{H}$ (Towne et al., 2018). Plotting the energy content of each singular value mode $\mathbf{C}$ as a function of frequency helps us visualize which modes contain wave and/or turbulence energy. Next, we identify and discard the modes that do not contain wave energy. The parameter r consists of the lowest modes that contain wave energy. This truncation allows us to remove the higher-frequency turbulence from the data directly.

DMD is then applied to $\mathbf{H}$, using the rank truncation r that we just determined. Following the procedure outlined in the previous section, we obtain the eigenvalues $\mathbf{\Lambda}$, eigenvectors (or modes) $\mathbf{\Phi}$, and amplitudes $\mathbf{b}$, which capture the coherent structures in the matrix $\mathbf{H}$. The j-th DMD mode ϕ_j and its corresponding eigenvalue λ_j have a distinct oscillation frequency f_j that can be calculated as

$$f_j = \frac{\mathrm{Im}[\log(\lambda_j)]}{2\pi\Delta t}. \tag{2.10}$$

The modes with frequencies within the wave range are referred to as wave modes and are transformed to the time domain as a wave time series using equation 2.8. The wave time series is then subtracted from the raw signal, leaving the turbulence component of the signal.

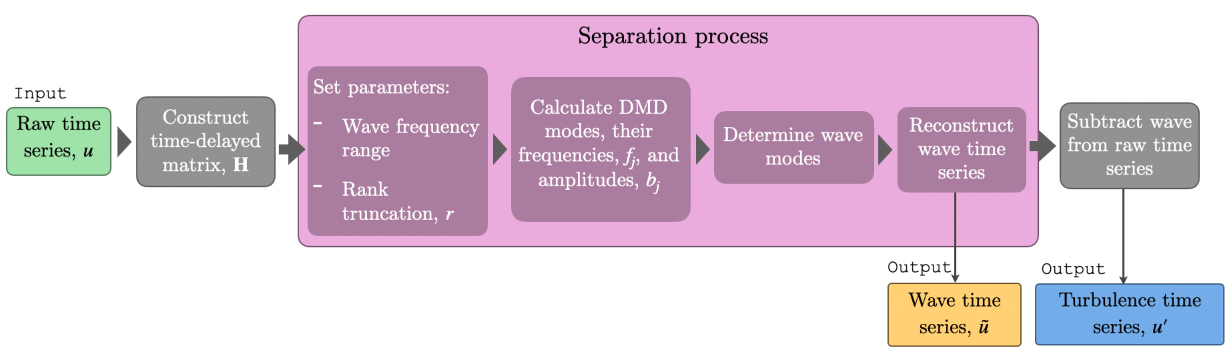

Figure 2.1: Workflow of the proposed DMD wave-turbulence separation methodology.

2.4 *Dataset descriptions*

We test our method on three distinct datasets to show its broad applicability: a synthetic dataset with known wave and turbulence components; a field dataset collected on a swell-dominated coastal shelf in a bottom boundary layer published in Reimers and Fogaren (2021), and laboratory data we collected in a surface boundary layer in a wind-driven wave tank. Table 2.1 shows some flow and DMD parameters used in our proposed decomposition method for each dataset. Additionally, table 2.2 shows the relative wave intensity $\tilde{u}_{\mathrm{rms}}/u'_{\mathrm{rms}}$, which is estimated as the ratio of the wave to the turbulence root-mean-square velocity obtained from the DMD-based decomposition. Note that we cover a range of wave intensities and that the field and laboratory waves are the most and least intense, respectively.

Data type	N	f_s (Hz)	T_p (s)	Wave range (Hz)
Synthetic	10000	10	5	0.117 – 0.6
Field	7200	8	14.29	0.031 – 0.175
Laboratory, u	18000	30	0.5	1.02 – 3.16
Laboratory, w	18000	30	0.5	1.02 – 3.16

Table 2.1: Summary of dataset characteristics including some input and output parameters from the wave-turbulence decomposition. Characteristics include length of time series N, sampling frequency f_s, wave peak period T_p, and wave frequency range.

2.4.1 Synthetic data

Synthetic data allows us to test our wave-turbulence decomposition by comparing our decomposed velocities to the ground-truth signals directly. To create the dataset, we linearly add a wave $\tilde{u}$ and turbulence u' velocity time series. In this case, wave-turbulence interactions are exactly zero and $\tau/\rho_f = -\langle u'w' \rangle$. The turbulence data come from a streamwise velocity time series collected with hot-wire anemometry in a wind tunnel sampled at 60 kHz (Castro and Vanderwel, 2021). The turbulence spectrum has a developed inertial range between 0.13 Hz to 0.6 Hz.

The wave amplitude spectrum $S(\omega)$ was generated using a Joint North Sea Wave Project

Data type	m	n	r	ψ_{wave}	r/n	ψ_{wave}/r	$\tilde{u}_{\text{rms}}/u'_{\text{rms}}$
Synthetic	3000	5911	173	104	0.029	0.601	1.91
Field	5700	1500	48	34	0.027	0.708	8.05
Laboratory, u	13000	5000	1000	506	0.200	0.506	0.30
Laboratory, w	12500	6500	1300	732	0.200	0.563	0.72

Table 2.2: Summary of the optimal number of rows m and columns n of the time-delayed matrix $\mathbf{H}$, the optimal rank truncation r used and the number of wave DMD modes ψ_{wave}, including the relative rank r/n used to separate high frequency turbulence unaffected by the wave and ψ_{wave}/r used to reconstruct the wave time series. The final column reports the relative wave intensity $\tilde{u}_{\text{rms}}/u'_{\text{rms}}$ using the DMD-separated velocities. For the synthetic data, the true wave intensity is $\tilde{u}_{\text{rms}}/u'_{\text{rms}} = 1.81$.

(JONSWAP) model (Hasselmann et al., 1973)

$$S(\omega) = \frac{\alpha g^2}{\omega^5} \exp\left[-\frac{5}{4}\left(\frac{\omega_p}{\omega}\right)\right] \gamma^{\exp\left[-\frac{(\omega/\omega_p - 1)^2}{2\beta^2}\right]}, \tag{2.11}$$

where $\alpha = 0.01$ is the intensity of the JONSWAP spectrum, g is the acceleration of gravity, ω is the angular frequency, ω_p is the angular frequency of the peak of the spectrum, $\gamma = 3.3$, and the factor $\beta = 0.07$ for $\omega \leq \omega_p$ and $\beta = 0.09$ for $\omega > \omega_p$. The peak period T_p was chosen to be 5 seconds, which results in $\omega_p = 0.2$ Hz. At a point below the surface where $x = 0$, and $z = -2$m, linear wave theory was used to generate the velocity time series from the sum of $N_w = 500$ wave components:

$$\tilde{u}(x, z, t) = \sum_{i=1}^{N_w} U_i \cos(k_i x - \omega_i t + \phi_i) \exp(k_i z), \tag{2.12}$$

where $U_i = a_i \omega_i$ is the wave velocity amplitude vector, $a_i = \sqrt{2S(\omega_i) d\omega}$ is the amplitude of the spectrum at frequency ω_i, $k_i = \omega_i^2/g$ is the wave number that satisfies the deep-water linear dispersion relation, and ϕ_i is the phase which is randomly sampled from the interval $[0, 2\pi)$.

The turbulence time series was decimated from 60 kHz to 10 Hz to match the sampling frequency of the JONSWAP waves time series. The total detrended horizontal component of velocity u is obtained from adding the wave and turbulence components of horizontal velocity, defined in equation 2.1, as $u = u' + \tilde{u}$. The power spectrum of u, shown in figure 2.2b, preserves the turbulence developed inertial range between 0.13 Hz to 0.6 Hz and shows that the wave energy is concentrated around the wave peak frequency at 0.2 Hz.

2.4.2 Field data

The field data consists of long waves measured in a turbulent boundary layer above the coastal shelf. The data comes from a published dataset in Reimers and Fogaren (2021). We are analyzing their acoustic Doppler velocimeter (ADV) data collected during a campaign to measure oxygen eddy covariance. The ADV captures a time series of the three perpendicular velocity components and pressure at a single point in space. We analyze only a time series of u velocity components from their data. The measurements were collected from a lander deployment along the Oregon shelf above a sandy seafloor. The ADV probe's sampling volume was 30 cm above the bottom of the sea floor in 80 m of water and was sampling at a frequency of $f_s = 64$ Hz, which was then downsampled to $f_s = 8$ Hz. Each deployment was broken down into 15-min (7200 observations) long bursts, and we consider only one burst in our study. The mean current of the analyzed burst time series is 0.11 m/s, the peak wave period T_p is 14.28 seconds (see figure 2.8b) and for reference, the significant wave height was estimated to be 3.4 m. We chose this specific burst because it presented a mix of high and low amplitude waves, as shown in figure 2.8c. For further details about the data acquisition, please consult the original study (Reimers and Fogaren, 2021).

2.4.3 Laboratory data

To contrast the bottom-boundary layer field data, we collected laboratory data in a wind-driven surface boundary layer with short intermittently breaking waves. The data was collected during experiments conducted in the Washington Air-Sea Interaction Facility (WASIRF) which is a 12.2 m long, 0.91 m wide wind-wave tank. Tap water was filled to a depth of 0.6 m leaving 0.6 m of headspace above for air circulation. To create wind, a suction fan propelled air through the test section's headspace and recirculated it via an overhead duct. See Baker and DiBenedetto (2023) for more details on the facility.

We collected a timeseries of 3-dimensional velocity at a height of 19 cm below the water surface with an ADV (Nortek Vectrino) under a wind speed of 16 m/s at a fetch of 7.5 m. The data was collected over 20-minutes at a sampling frequency f_s = 30 Hz. The wave energy spans the frequency range of 1 to 3 Hz, with a peak at 2 Hz (figures 2.9b and 2.10b). We post-processed the data using the despiking method proposed by Goring and Nikora (2002). Even after despiking the data, there is still some noise present in the data due to intermittent wave-breaking which generated large bubbles and affected the data quality. This noisy data provides another challenge to the decomposition. We apply our decomposition method to both the horizontal and vertical components of velocity because they present contrasting conditions. The horizontal velocity data has high turbulence fluctuations when compared to the wave velocities, whereas the vertical velocity has wave and turbulence fluctuations with similar magnitude (see Table 2.2). Finally, we note that due the complex nature of the strongly wind-sheared flow and the intermittent wave-breaking, we see some deviations from the expected -5/3 slope in the inertial range (figure 2.9b).

2.5 *Results and Discussion*

In this section, we present the results obtained from analysing the synthetic, laboratory, and field data with our proposed DMD method. We demonstrate our DMD decomposition by applying it to all three datasets after first conducting a sensitivity analysis on the synthetic data. Next, we compare our results to the other two time-resolved mode-based decomposition methods: EEMD (Qiao et al., 2016; Huang et al., 2009) and Synchrosqueezed Wavelet transform (SWT) (Bian et al., 2018). After assessing the decomposition in both spectral and time space, we analyze the temporal autocorrelation of the decomposed turbulence signal, further demonstrating how our DMD method outperforms the other methods.

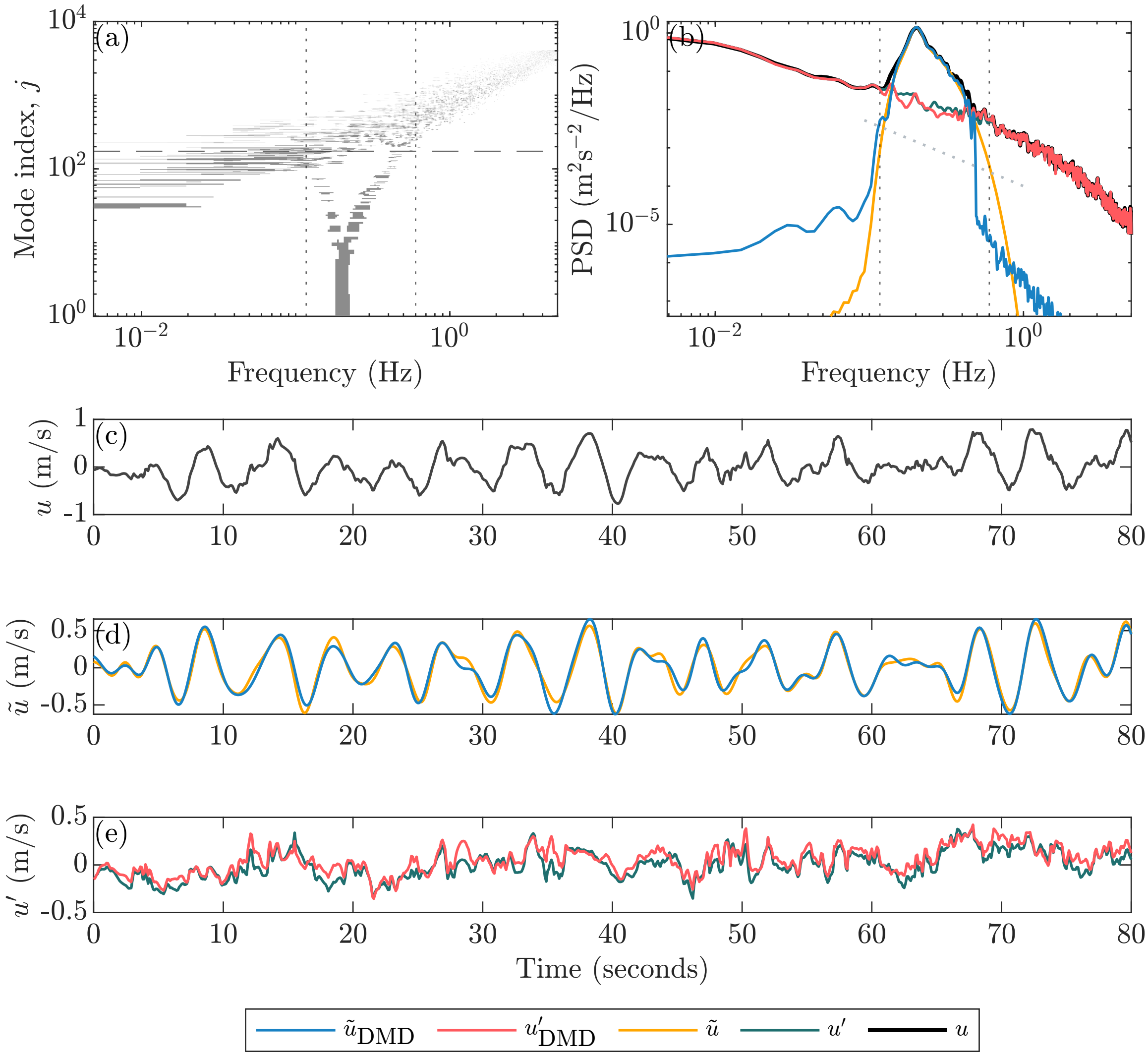

Figure 2.2: DMD wave-turbulence decomposition of u-component velocity of synthetic data. (a) POD spectrum of time-delayed matrix $\mathbf{H}$. (b) Power spectra of the original data and DMD-separated wave and turbulence. A -5/3 slope line is plotted for reference. In (c) we plot a portion of the original time series, (d) the true and separated wave components using 104 DMD modes, (e) and the true and separated turbulence components.

2.5.1 Synthetic data decomposition

The first step of our decomposition method is constructing the time-delayed matrix $\mathbf{H}$ and identifying the wave frequency range, as described in section 2.3 and shown in table 2.1. Next, we determine the rank truncation r by plotting the POD spectrum of $\mathbf{H}$ of the synthetic u data (figure 2.2a) and selecting the modes that contain wave energy. We observe two strong features in this plot: (1) the higher modes contain energy in monotonically increasing frequencies across the entire domain due to turbulence, showing the energy decreasing from low to high frequencies, consistent with the inertial range, and (2) a coherent high energy signal in lower modes between the frequency range of 0.13 and 0.6 Hz, indicated by the vertical dotted lines. This “dip” in the POD spectrum indicates an energetic range associated with the wave energy and accounts for a significant part of the variance in the time series. We use the location of the dip to inform the rank truncation. As indicated with the horizontal dashed line, we truncate at the $r = 173$ mode; that is, we take only the first 173 modes for the next step in the DMD. We see that while most of the wave energy is contained in these first r modes, there is also energy associated with low-frequency turbulence in these lowest modes. This clearly shows how POD alone fails at separating waves and turbulence since it can only isolate the high-frequency turbulence from the waves, not the low-frequency turbulence.

After determining the rank truncation, we are able to decompose the signal using DMD. Figure 2.2b shows the spectra of the DMD-filtered wave and turbulence time series which we compare with the true wave and turbulence spectra. Within the wave-frequency range, the DMD-filtered wave spectrum $\tilde{u}_{\mathrm{DMD}}$ closely follows the wave peak. Outside the wave-frequency range, the $\tilde{u}_{\mathrm{DMD}}$ spectrum falls sharply, capturing a similar shape to the true wave spectrum for multiple orders of magnitude before levelling off. The mismatch in the signals is clearer to see in the u'_{DMD} spectrum, which slightly underpredicts the turbulence in the wave-frequency range.

Figures 2.2(c-e) show the full u time series and the decomposed $\tilde{u}$ and u' time series alongside their true counterparts. We see overall agreement between the decomposed and true time series, however some mismatch exists. While the turbulence time-series plot shows that the separated signal accurately captures the low frequency turbulence fluctuations, there is stronger disagreement in the fluctuations with frequencies in the wave-range. Given that the wave signal was generated with 500 discrete wave signals and that the DMD resolution only resolved 104 modes, we do not expect a perfect reconstruction. In this method, the DMD is always discretizing a continuous wave frequency range, so we will always expect some mismatch. Column r/n in table 2.2 shows the ratio of the number of modes used to truncate the input matrix normalized by the number of columns used to construct the input matrix. For the synthetic data, the low rank-to-column ratio indicates that the dominant wave patterns in the signal were reconstructed using fewer modes compared to the other datasets.

Parameters	Length of raw time series, N			
	2500	5000	7500	10000
r_{opt}	210	165	155	173
$r_{\text{opt}}/n_{\text{opt}}$	0.179	0.061	0.043	0.029
n_{opt}	1175	2700	3900	5911
n_{opt}/N	0.47	0.54	0.52	0.59
ϵ	0.2737	0.2109	0.1894	0.1586

Table 2.3: Summary of sensitivity analysis from figure 2.3.

Method	ϵ	α (m/s)	α/u'_{rms}
DMD	0.159	0.039	0.24
EEMD	0.268	0.065	0.40
SWT	0.325	0.079	0.49

Table 2.4: Comparison of errors from DMD and other modal decomposition methods applied to the longest time-series length of $N = 10000$.

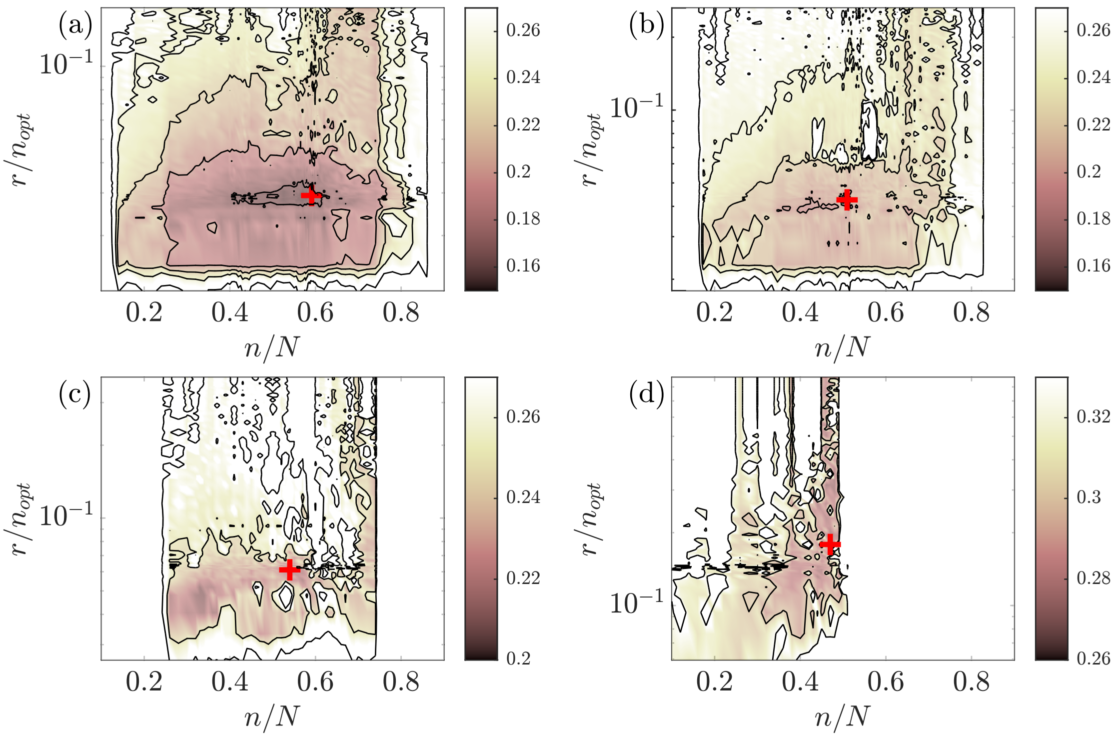

Figure 2.3: Sensitivity analysis to asses the separation performance of the DMD-based algorithm for different time series length, N. A measurement of error, ϵ, was calculated for every combination of normalized rank truncation, r/n_{opt}, and normalized number of columns, n/N, in the time-delayed matrix, $\mathbf{H}$, where n_{opt} is the optimal number of columns and the optimal combination is indicated by a red cross. (a) $\epsilon = 0.1586$, at $r_{\text{opt}}/n_{\text{opt}} = 0.029$, $n_{\text{opt}}/N = 0.5911$ ($N = 10000$), (b) $\epsilon = 0.1894$, at $r_{\text{opt}}/n_{\text{opt}} = 0.043$, $n_{\text{opt}}/N = 0.509$ ($N = 7500$), (c) $\epsilon = 0.2109$, at $r_{\text{opt}}/n_{\text{opt}} = 0.061$, $n_{\text{opt}}/N = 0.540$ ($N = 5000$), and (d) $\epsilon = 0.2737$, at $r_{\text{opt}}/n_{\text{opt}} = 0.179$, $n_{\text{opt}}/N = 0.470$ ($N = 2500$).

Sensitivity analysis on decomposition parameters

We conducted a sensitivity analysis on the decomposition based on the two main tuning parameters: the rank truncation r and the number of columns of the time-delayed input matrix n in order to identify the optimal r_{opt} and n_{opt} for the decomposition. In addition, we also varied the length of the time series N and repeated the sensitivity analysis to assess how r and n vary with N. We quantified the accuracy of the decomposition by minimizing the normalized error ϵ, which is defined as follows:

$$\epsilon = \frac{\|u'_i - u'_{i,\mathrm{DMD}}\|_2}{\|u'_i\|_2}, \tag{2.13}$$

where u'_i and $u'_{i,\mathrm{DMD}}$ are the true and decomposed turbulence time series (here the notation refers to DMD, but we also calculate this error for the EEMD and SWT methods), respectively, at time t_i, and $\|\cdot\|_2$ is the L_2 norm. For comparison, we also measured the mean absolute error α defined as

$$\alpha = \frac{1}{N}\sum_{i=0}^{N} |(u'_i - u'_{i,\mathrm{DMD}})|. \tag{2.14}$$

We conduct the sensitivity analysis across four different time-series lengths to assess the importance of the length of the dataset. Figures 2.3(a-d), show the results of the sensitivity analysis for $N = 10000, 7500, 5000,$ and 2500, respectively. We plot the norm-based error ϵ for different combinations from the space of normalized r/n_{opt} and normalized number of columns n/N. The optimal combination (n_{opt}/N, $r_{\mathrm{opt}}/n_{\mathrm{opt}}$) is indicated by a red cross.

Overall, the optimal n/N ratio is not too sensitive and ranges between 0.5 and 0.6, while the optimal r minimizes the error only in a narrow range of values. This indicates that, at least for this simple case, the preferential dimension of the input time-delayed matrix is an approximately square matrix. This might be due to the fact that for a large dataset we have enough physical information to resolve coherent features in the time domain n and the "spatial" domain m that we constructed via time-delaying. However, when there is limited information by the shortened time-series, as in the case of figure 2.3d, the preferential input matrix shape is a tall, skinny matrix. This suggests a preference for "spatial" information over temporal information, and that meeting a critical column length is more important than increased row length. We can observe that the optimal r shows a small decrease with N (except for $N = 2500$) but overall is fairly stable. Selecting an appropriate rank truncation is essential for accurately capturing the waves in the time series. If r is too low, some waves may be missed by the DMD algorithm, leading to an incomplete reconstructed time series. Conversely, if r is too high, it may lead to overestimation of the wave energy.

Table 2.3 summarizes the different tuning parameters for all time-series length N and their associated errors. We see a decrease of the norm-based error ϵ with N which makes sense since the DMD is a data-based algorithm, and more data generally improves performance. However, as the data increases so does the computational cost of performing the decomposition. We compare the DMD method to EEMD and SWT in table 2.4, where we see that given the same time-series length, our DMD method outperforms the other modal decomposition methods. While the EEMD outperforms the SWT, they both have higher errors than the DMD method, even when DMD was applied to only half the data ($N = 5000$). Overall, our method seems to be perform the best when applied to this dataset. At the end of this section, we compare the methods in more detail by applying them to all of the datasets.

In our analysis, we use the ratio r/n to understand how effectively the first step of our algorithm, the rank truncation, separates waves from turbulence. A low r/n indicates a more effective rank truncation. This ratio measures how well we can isolate the wave energy from the higher frequency turbulence that does not overlap in the frequency space. Essentially, this step resembles a low-pass filter, in the sense that most of the truncated modes correspond to high frequency motion. We don't expect r/n to be universal because the shape of the spectra can vary; e.g., narrow-banded waves at lower frequencies would likely result in a lower r/n relative to wide-banded waves with the same intensity that occupy higher frequencies, given the same turbulence spectrum. In addition, the number of columns n in the input matrix controls the lowest resolvable frequencies, and therefore will depend on the location of the wave frequency peak in frequency domain; higher-frequency waves might require a smaller n compared to low-frequency waves in order to capture the peak wave frequency. Our observations show that r/n generally increases as wave intensity decreases, indicating that the rank truncation is less effective at isolating wave energy when the waves are weaker.

We then consider ψ_{wave}/r to evaluate the effectiveness of the second step of our decomposition (see table 2.2). This ratio represents the proportion of DMD modes used to reconstruct the waves relative to all modes remaining after the initial truncation. Higher wave intensity usually corresponds to a higher ψ_{wave}/r because most of the modes retained are wave modes. Essentially, to summarize the two main steps of the algorithm: first the rank truncation initially identifies the modes containing the relevant frequency content, and second the DMD step extracts the wave components from this subset. By quantifying r/n and ψ_{wave}/r, we can compare the effectiveness of each step in the separation process.

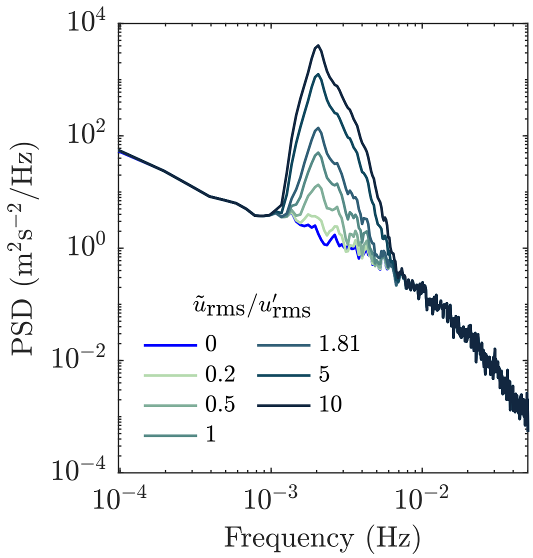

Figure 2.4: Synthetic spectra used for sensitivity analysis on wave intensity $\tilde{u}_{\mathrm{rms}}/u'_{\mathrm{rms}}$. Wave intensity of zero represents the raw turbulence signal, u'.

Sensitivity analysis on wave intensity

Additionally, we performed a sensitivity analysis on the effect of relative wave intensity $\tilde{u}_{\mathrm{rms}}/u'_{\mathrm{rms}}$. We scaled the synthetic wave time series amplitudes linearly to adjust the wave intensity, keeping the frequency and phase components of the synthetic wave signal constant. This results in the wave spectrum moving up or down relative to the turbulence spectrum, as shown in Figure 2.6. This also changes the apparent width of the wave spectral peak which overlaps the inertial range; a change that is due to the weaker wave energy away from the peak frequency being overshadowed by the turbulence. We chose the wave intensities $\tilde{u}_{\mathrm{rms}}/u'_{\mathrm{rms}} = [0.2, 0.5, 1, 5, 10]$, in addition to the wave intensity $\tilde{u}_{\mathrm{rms}}/u'_{\mathrm{rms}} = 1.81$ that we used in the previous single-case analysis (figure 2.6), to cover a wide range of scenarios. This range also covers the high and low intensities present in the field and laboratory data, respectively.

Figure 2.5 presents the norm-based reconstruction errors for waves and turbulence across

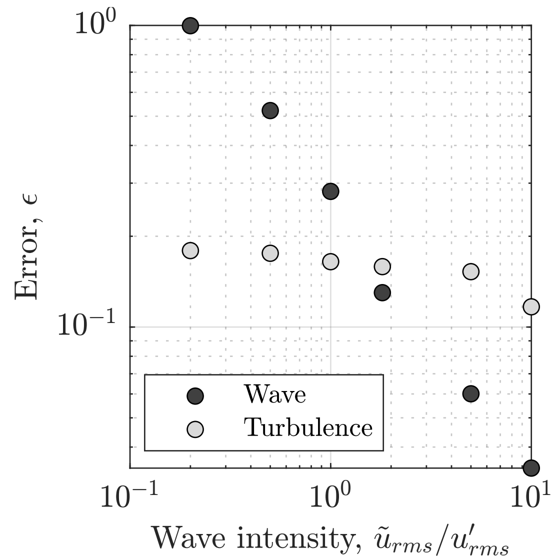

Figure 2.5: Reconstruction error from wave and turbulence at the different wave intensities in the sensitivity analysis.

varying wave intensities. We expect a decrease in the reconstruction error as wave intensity increases because the DMD algorithm will be able to more effectively identify the coherent features of wave motion as distinct from the turbulence. Conversely, as wave intensity decreases, the performance of our decomposition method is expected to decline. We note that the error in turbulence reconstruction decreases more slowly with increasing wave intensity, relative to the wave reconstruction error. This is because the turbulence reconstruction is less sensitive to the decomposition because most of the turbulence in the signal is unaffected by the waves due to it occurring at frequencies outside the wave range.

In Figure 2.6, we plot the decomposed wave spectra relative to the input spectra and the true wave spectra to further evaluate the effectiveness of the decomposition. We see that in all cases, the wave peak above the turbulence spectra is well represented by the decomposition. However, as the wave intensity decreases and more of the wave spectrum falls below the turbulence spectrum, we see the decomposition struggles to recover the shape of the original wave spectrum accurately. This is especially clear in the lowest wave intensity case, which has a large wave reconstruction error due

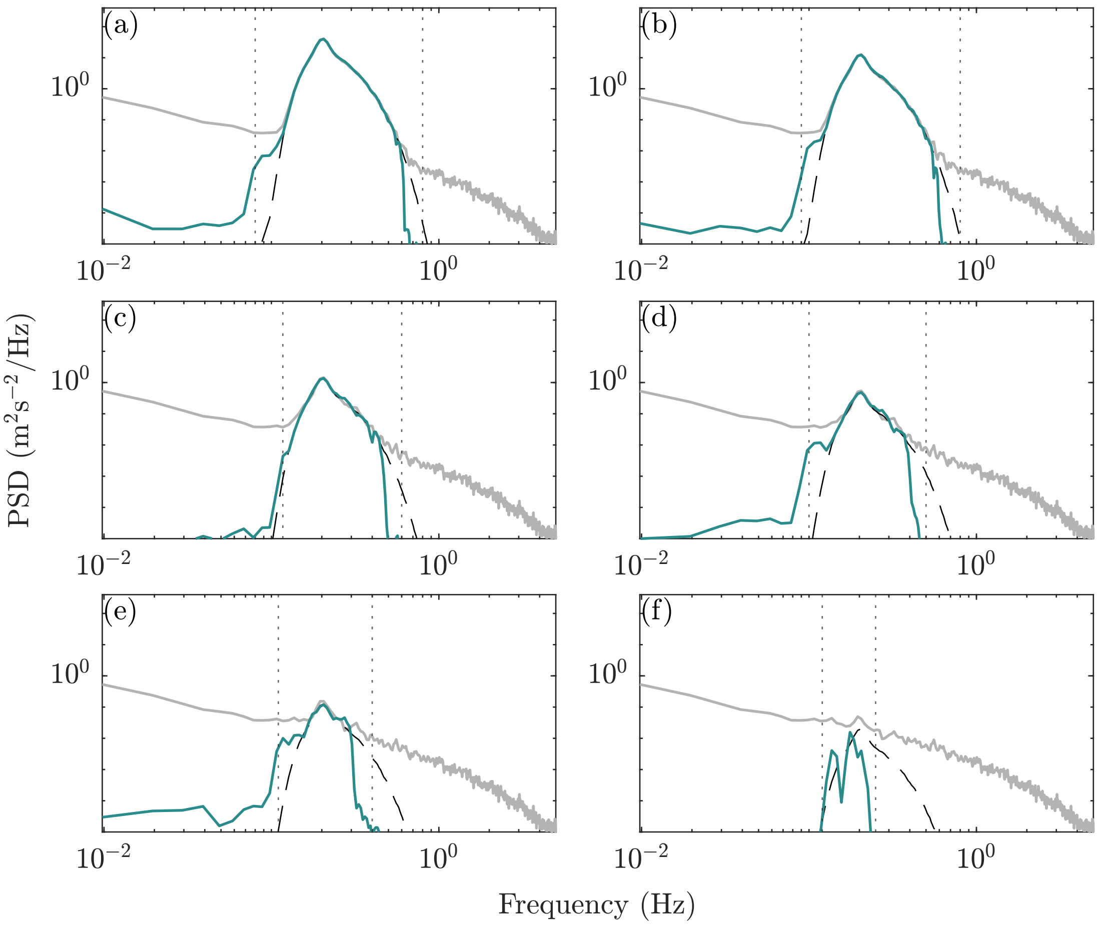

Figure 2.6: Comparison of the DMD-separated wave spectrum (solid teal line) to the true wave spectrum (dashed black line) and the combined wave and turbulence spectrum (solid grey line). Each figure correspond to a wave intensity: (a) $\tilde{u}_{\mathrm{rms}}/u'_{\mathrm{rms}} = 10$; (b) $\tilde{u}_{\mathrm{rms}}/u'_{\mathrm{rms}} = 5$; (c) $\tilde{u}_{\mathrm{rms}}/u'_{\mathrm{rms}} = 1.81$; (d) $\tilde{u}_{\mathrm{rms}}/u'_{\mathrm{rms}} = 1$; (e) $\tilde{u}_{\mathrm{rms}}/u'_{\mathrm{rms}} = 0.5$; (f) $\tilde{u}_{\mathrm{rms}}/u'_{\mathrm{rms}} = 0.2$.

to the poor reconstruction of the wave and the small norm of the true wave signal. Additionally, we see that the DMD method tends to overestimate the wave energy at the lower end of the wave frequency range, while underestimating the wave energy at the higher end. Although, these errors are small compared to the overall spectral energy in the combined wave and turbulence signal. In summary, the DMD method works best when the wave intensity is high and fails when the wave intensity is low; therefore, we recommend our method for cases when the wave energy is similar or larger in magnitude than that of the turbulence and for when there exists a clear wave peak in the power spectrum of the raw signal.

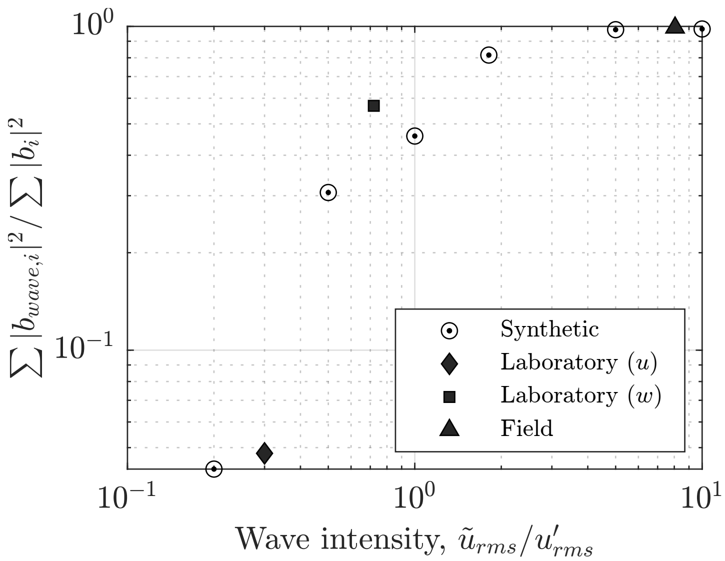

Figure 2.7: Relative energy contained in the DMD modes that each wave intensity case requires to resolve the coherent features in the signal. The y axis is the energy of the DMD wave modes relative to the energy contained in the entire signal, where b_i represents the amplitude of the i-th DMD mode, while $b_{\text{wave},i}$ represents the amplitude of the subset of DMD modes associated with wave motion and used in the reconstruction of the wave signal.

To further evaluate how the decomposition performs across wave intensity, we consider the relative energy of the DMD wave modes. Figure 2.7 shows a direct correlation between the amount of wave energy in the signal and the corresponding DMD mode energy required to accurately reconstruct the wave signal. The expression $\sum |b_{\text{wave},i}|^2 / \sum |b_i|^2$ in the y axis in figure 2.7 quantifies the ratio of the energy contributed by the subset of wave-containing DMD modes to the total energy from all DMD modes. Values close to unity mean that the wave modes dominate the dynamics of the system, while values close to zero mean that the contribution of the wave modes is small compared to the overall dynamics. Figure 2.7 also shows a general trend across data sets and wave intensities. When waves and turbulence are similar in intensity ($\tilde{u}_{\text{rms}}/u'_{\text{rms}} = 1$), the waves account for approximately half of the energy in the DMD modes. However, as the wave intensity nearly doubles ($\tilde{u}_{\mathrm{rms}}/u'_{\mathrm{rms}} = 1.81$), the proportion of DMD mode energy associated with waves increases significantly, indicating a strong dominance of wave energy in the reconstruction. Conversely, when the wave intensity is halved, waves contribute only about 30% of the DMD mode energy, highlighting the reduced influence of weaker wave signals.

2.5.2 Field data decomposition

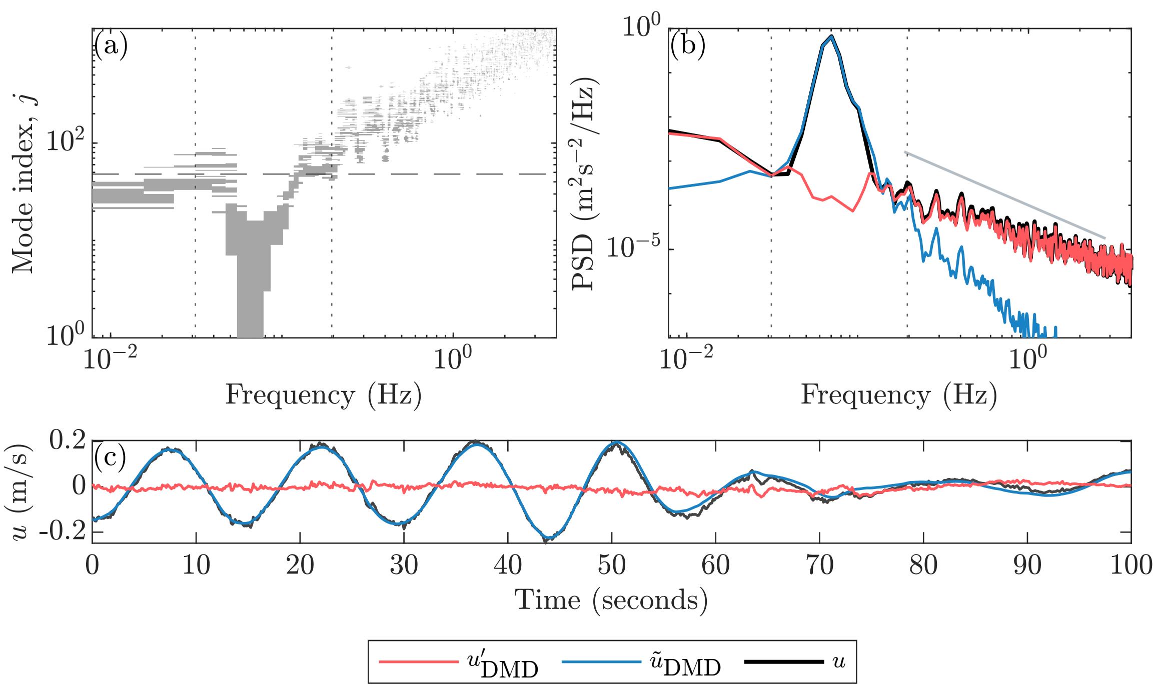

Figure 2.8: DMD wave-turbulence decomposition of u-component velocity of field data. (a) POD spectrum of time-delayed matrix $\mathbf{H}$. (b) Power spectra of the original data and DMD-separated wave and turbulence. A gray -5/3 slope line is plotted for reference. (c) A portion of the time-series of the original and decomposed signals. The wave motion was reconstructed using 34 DMD modes.

We plot the POD spectrum of the field data (figure 2.8a), and find that similar to the synthetic data in figure 2.2a, there are two features: one associated with the turbulence energy that is seen across the frequency range, and a dip in the energetic modes associated with the the wave energy concentrated between 0.04 and 0.16 Hz, marked with the vertical dotted lines. It is worth noting that in this case, there is not a well-defined turbulence signal in the wave frequency range. Wave and turbulence interactions present in real data, as compared with the synthetic data, may reduce the effectiveness of the POD modal separation in the overlapping frequency range. This further supports why POD alone cannot always isolate waves and turbulence. Based off the location of the dip, we rank-truncate to $r = 48$ modes to preserve the energy in the wave frequencies and remove the high frequency turbulence. The final filtered velocity spectra are shown in figure 2.2b alongside the raw signal spectrum. We see that the DMD method is able to isolate the wave energy and flatten the turbulence spectrum under the wave peak. While the wave spectrum contains nonzero energy in the frequencies outside the wave range, the energy is small enough to not affect the turbulence spectrum.

In Figure 2.2c, we present a portion of the separated time series over the raw signal. This portion of data was chosen to highlight a potentially difficult section to decompose where the wave amplitude sharply decreases over time. We expect the decomposition to perform best when the wave energy is large relative to that of the turbulence. While we see strong agreement with the wave signal during the first half of the plot, we see the mismatch increases once the wave amplitude decreases in the second half of the plot, however the decomposed wave velocity is still able to capture the transition moderately well and maintain the shape of the waves. When we later compare this decomposition to other methods, we find it has similar performance to the EEMD and SWT methods because this is the dataset with the largest relative wave energy, i.e., it is theoretically the easiest signal to decompose. Additionally, table 2.2 indicates that this is the dataset with the highest relative wave intensity $\tilde{u}_{\mathrm{rms}}/u'_{\mathrm{rms}}$ and also the lowest r/n values. This indicates that the wave motion present in the signal can be captured using a smaller number of modes relative to the total rank.

2.5.3 Laboratory data decomposition

The laboratory data represents a case with weak wave energy relative to the turbulence, and therefore we expect it to be the most challenging to decompose. The data is also more noisy than the field and

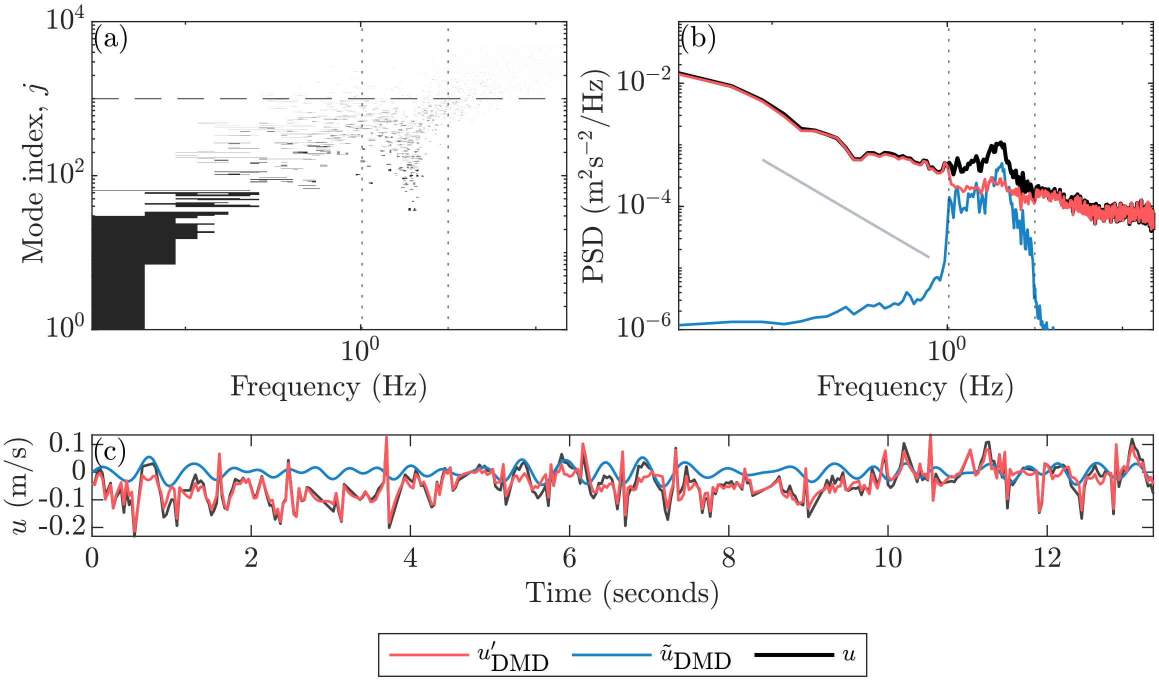

Figure 2.9: DMD wave-turbulence decomposition of u-component velocity of laboratory data. (a) POD spectrum of time-delayed matrix $\mathbf{H}$. (b) Power spectra of the original data and DMD-separated wave and turbulence. A gray -5/3 slope line is plotted for reference. (c) A portion of the time-series of the original and decomposed signals. The wave motion was reconstructed using 506 DMD modes.

synthetic data, but it is also the longest dataset of the three. We start by considering the POD spectra of both u and w (figures 2.9a and 2.10a) which show that the wave energy is contained within the frequency range of 1 to 3 Hz. What is interesting in these POD spectra, unlike in those of the synthetic and field data, is that the low number modes only contain low frequency turbulence, and that the wave energy is contained in intermediate modes. Based off the POD spectra, we truncate at $r = 1000$ and $r = 1300$ modes for u and w respectively.

The fully decomposed spectra are plotted in figures 2.9b and 2.10b. We see that the DMD method separated and removed most of the wave energy from the turbulence in both cases. First considering the u spectrum (figure 2.9b), we see that the majority of the wave peak is removed

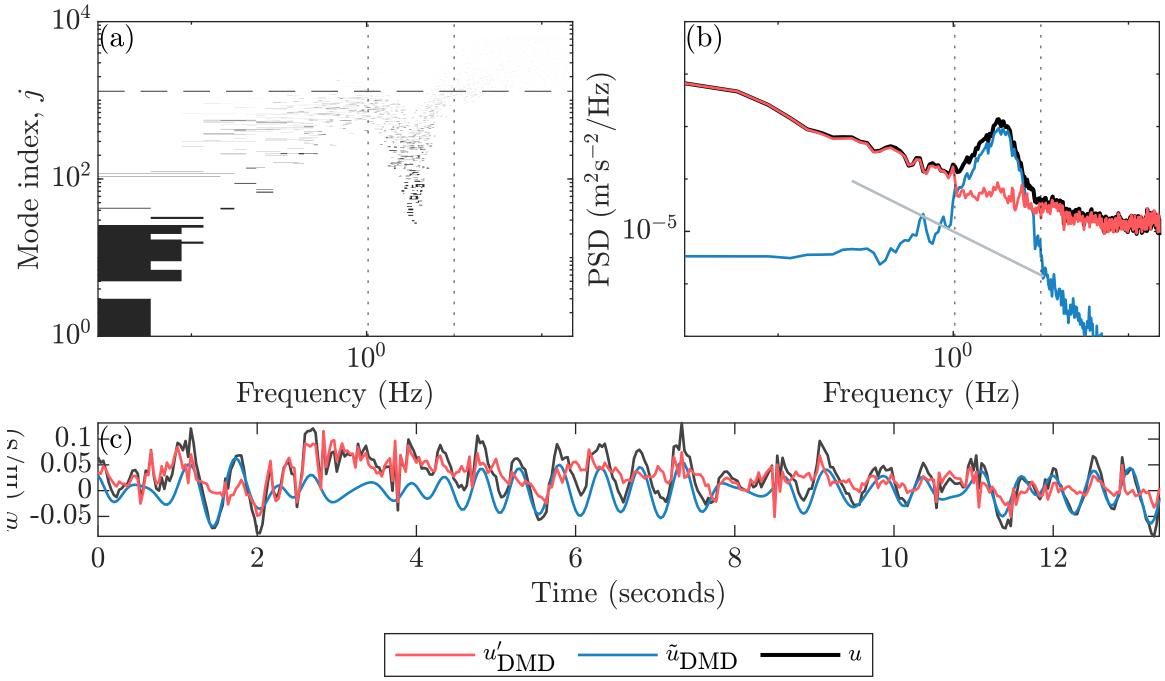

Figure 2.10: DMD wave-turbulence decomposition of w-component velocity of laboratory data. (a) POD spectrum of time-delayed matrix $\mathbf{H}$. (b) Power spectra of the original data and DMD-separated wave and turbulence. A gray -5/3 slope line is plotted for reference. (c) A portion of the time-series of the original and decomposed signals. The wave motion was reconstructed using 732 DMD modes.

from the turbulence spectrum, and that the wave spectrum has less energy than the turbulence spectrum at almost all frequencies, confirming that this is a turbulence dominated flow. The time-series reconstruction in figure 2.9c again shows the small wave velocity amplitude compared to the turbulence fluctuations. We also see some noise spikes in the data which have been isolated to the turbulence time series.

Next, we consider the w decomposition in figure 2.10b where we observe a cleanly separated turbulence and wave spectra. Note the difference between this and the u spectra, specifically how they have similar wave energy but the w spectra has much weaker turbulence. The time-series reconstruction in figure 2.10c show that the separated waves closely follow the trend of the raw data, and that both the high and low frequency turbulence fluctuations are isolated to the turbulence time series. In table 2.2, we see that this is the dataset with the lowest wave intensity relative to the turbulence. This low wave intensity is a challenge for our decomposition, however by using a long enough time-series and a high r/n truncation, the DMD method is able to give a better separation when compared with other methods.

In order to further assess the decomposition results, we compare the mean Reynolds stress $\langle u'w' \rangle$ from the raw signal with those from the decomposed turbulence and wave components. We expect the Reynolds stress associated with waves to be significantly lower than that generated by turbulence. Consistent with this expectation, our analysis shows that the wave Reynolds stress is over an order of magnitude smaller than the residual turbulence Reynolds stress. We find the Reynolds stress values to be -5.1×10^{-4}, -4.5×10^{-4}, and -0.19×10^{-4} (m/s)^2 for the raw, decomposed turbulence, and decomposed wave signals respectively. This confirms that the wave momentum flux is inefficient compared to that of the turbulence, and that the DMD decomposition can successfully isolate wavelike motions from turbulence.

Additionally, we visualize the time series of $\tilde{u}_{\mathrm{DMD}}$ and $\tilde{w}_{\mathrm{DMD}}$ together in figure 2.11. We expect the horizontal and vertical wave velocities to have a 90° phase shift in time and for them to have similar amplitudes given that they were deep water waves (short waves relative to the depth of the tank). The initial section of figure 2.11 shows a disagreement between both the expected wave magnitudes and the phase shift, which might be caused by the presence of strong turbulence; however, the rest of the time series shows good agreement with the expected wave characteristics from theory. Throughout the time series, the $\tilde{u}_{\mathrm{DMD}}$ velocity amplitude is slightly underpredicted when compared with the $\tilde{w}_{\mathrm{DMD}}$ signal; this is likely due to the u decomposition underperforming due to the stronger turbulence. Overall, we find that the DMD method is able to decompose the signals fairly well, even given a noisy dataset with relatively weak, irregular waves under intermittent wave-breaking.

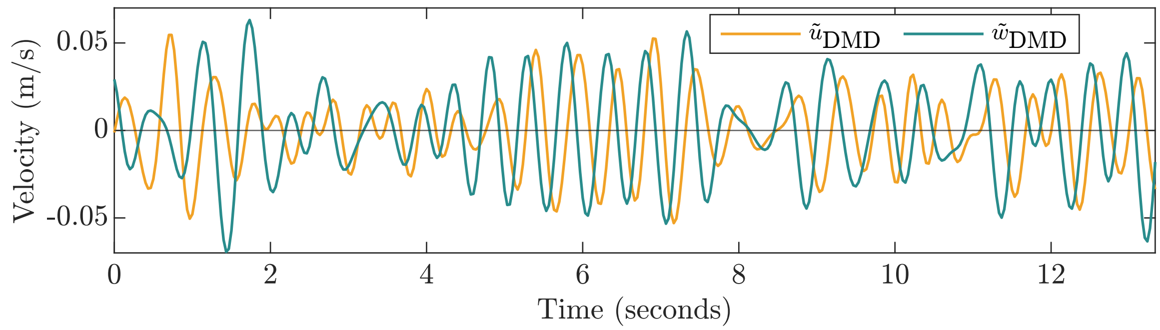

Figure 2.11: The u and w velocity components of DMD-separated wave time series of the laboratory data.

2.5.4 Comparison with other decomposition methods

We compare our decomposition method to the EEMD and SWT, two other modal decomposition techniques that work with a single time series. To compare the methods, we plot the separated turbulence spectra using each method for each dataset in Figure 2.12. Across all four plots, we see that the SWT tends to excessively remove energy from the turbulence in the wave-range, causing significant dips in the turbulence spectra. In contrast, the EEMD generally performs as well as the DMD method for the synthetic and field data in figures 2.12a and 2.12b, respectively. We note though that the EEMD has caused some turbulence energy redistribution, adding energy into the turbulence in the field data, as seen in figure 2.12b between 0.2 to 0.4 Hz. Finally, the laboratory data (figures 2.12c and 2.12d) is the hardest to decompose due to its weak, irregular waves, and that is where we clearly see that the DMD outperforms the other two methods. The DMD filtered spectra is able to closely follow the expected slope of the turbulence spectra for both the u and w velocity spectra.

The methods show the most similar decomposition for the field data, which is the dataset with the highest wave intensity. This is unsurprising and suggests that the stronger the wave intensity, the easier the signal should be to decompose using any method. Even though the synthetic data has exactly no wave-turbulence interactions which should in theory mean it is relatively easy to decompose, its lower wave-intensity causes issues for the SWT method. Finally, the laboratory data

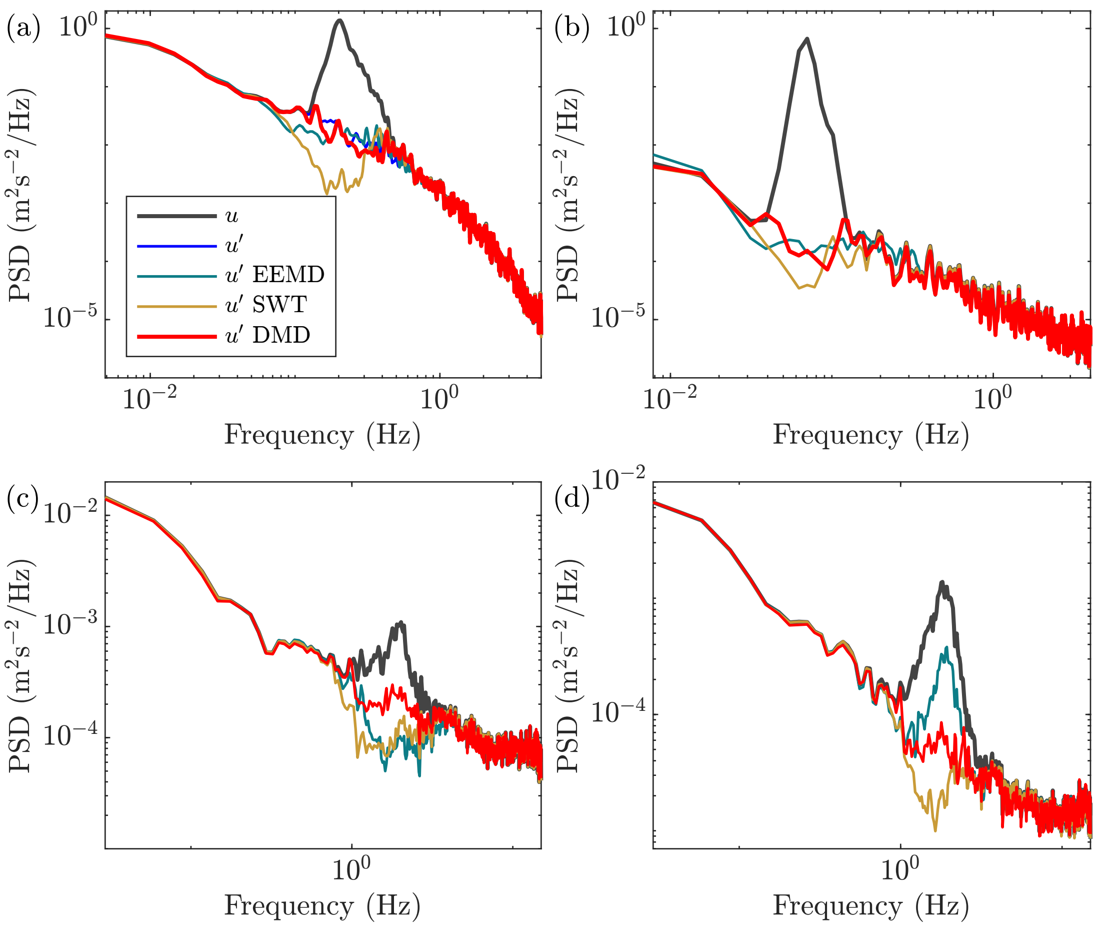

Figure 2.12: Comparison of modal decomposition methods, showing the spectra of the original data and the decomposed turbulence data. (a) Synthetic data u velocity, (b) field data u velocity, (c) and (d) laboratory data u and w velocity, respectively.

has the lowest wave-intensity, and this is where the benefits of the DMD-method are the clearest. One reason the SWT may underperform is because it determines its basis *a priori*; the method tries to fit the data to a wavelet basis, which might not always be a good descriptor of the dynamics of the system. Alternatively, the EEMD uses IMFs as an *a posteriori* basis, that is, they adapt to the data being analyzed. However, it seems that the IMFs might not be separating the waves from the turbulence completely, resulting in mixed modes which contain both turbulence and wave energy. The utility of this method is further hindered by the fact that the number of IMFs is determined by the EEMD algorithm which removes a tuning parameter.

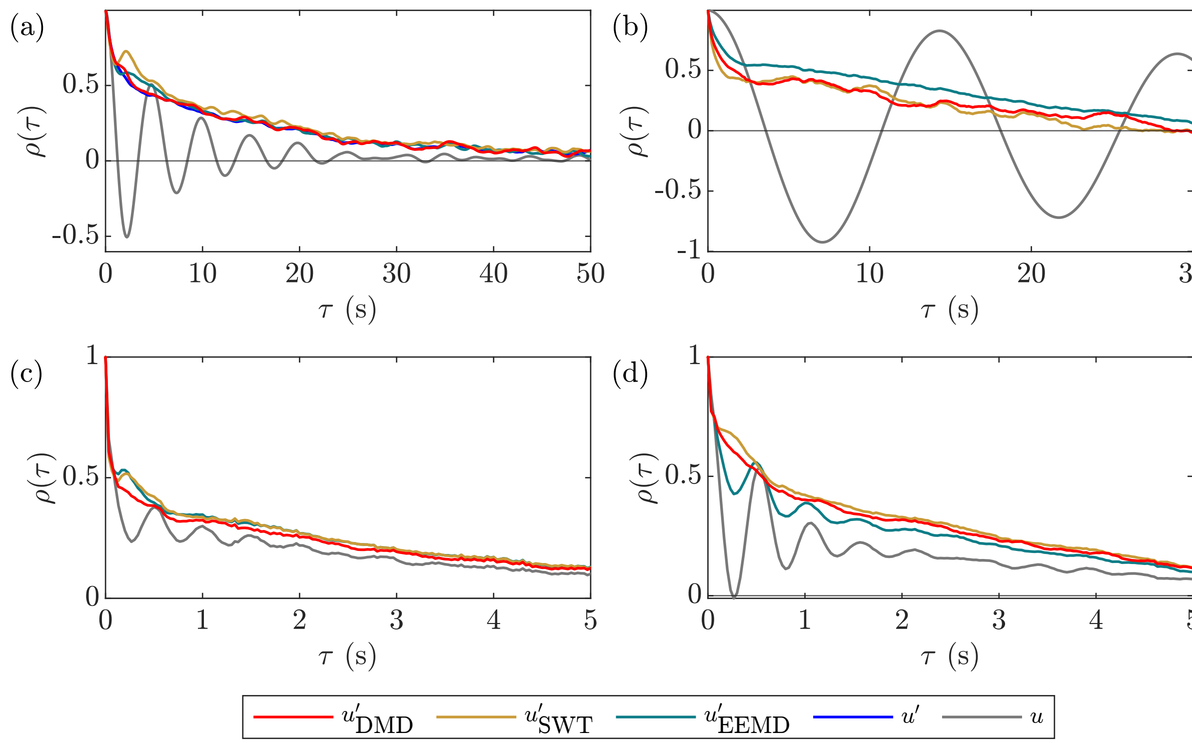

Figure 2.13: Normalized autocorrelation of raw (u), DMD-filtered turbulence (u_{DMD}), EEMD- and SWT-filtered turbulence (u_{EEMD} and u_{SWT}, respectively) signals. (a) Synthetic data u velocity, the black line is the true turbulence, u'. (b) Field data u velocity. (c) and (d) Laboratory data u and w velocity, respectively.

We further compare the methods by computing the normalized autocorrelations $R(\tau)$ of the filtered turbulence velocity across the different datasets, as shown in figure 2.13. The raw autocorrelations, plotted in gray for reference, show a clear periodic wave signal across all datasets. Successfully isolating the turbulence from the waves would remove all time periodicity and preserve the exponential decay expected as the turbulence fluctuations decorrelate over time. We see that in most cases, the methods are all able to remove the majority of the wave signal. With respect to the synthetic data (figure 2.13a), we know what the true turbulence signal is, and we see that while all the methods follow the true turbulence autocorrelation closely, shown with a black line, the SWT performs the worst, as shown by the small peak in the signal after the initial decrease. In figure 2.13b, the field data autocorrelations all remove the wave, and it is unclear which performs best here from visual inspection. Recall that the EEMD method had added energy into the turbulence spectra, so it's likely that its higher autocorrelation values are inaccurate. Finally, in the laboratory data (figures 2.13c and 2.13d), we clearly see the DMD method performs the best. It is able to remove all wave peaks while still capturing the long-time temporal decorrelation of the turbulence. This analysis clearly shows the strength of the DMD-method across a variety of datasets and demonstrates how it can be used for more than just spectral analysis, particularly under conditions that pose challenges to other decomposition methods.

2.6 *Conclusion*

While many wave-turbulence decomposition methods have been developed over the years, they are typically limited in their use case. For example, they may be restricted to the spectral domain precluding a time-series construction, they may require multiple synchronized measurements, or they may have restrictive assumptions such as no wave-turbulence interactions. In many scenarios, this assumption can easily break, especially because waves and turbulence do interact across different time scales (Guo and Shen, 2013). Given these challenges, newer modal decomposition methods have been developed, such as the EEMD and the SWT. These methods still have their drawbacks. For example, the SWT uses a predetermined basis to project the data that is not flexible for highly nonlinear data whereas the EEMD introduces noise as a filter to differentiate scales in the time series which can lead to a more accurate separation of the time series' intrinsic modes. However, this process can still result in shifts in how the energy is distributed across the IMFs due to the artificial noise introduced to the decomposition process.

These approaches are not optimal for highly nonlinear data, resulting in either poor or excessive wave energy separation. To address these limitations, we developed a new wave-turbulence decomposition method using DMD, leveraging its data-driven adaptive basis and minimal assumptions. Our method applies DMD to a single time-series, assisted by a time-delay embedding. It is able to isolate the wave-components without significantly affecting the turbulent signal at similar frequencies. In the case of velocity data, we show how the method is able to recover the inertial range scaling below the wave peak. The main assumptions that underlie this method are that the waves and turbulence can be separated and that waves are the most coherent feature of the time-series, which are reasonable assumptions considering the dynamics of the system. We applied our method to synthetic, field, and laboratory data which covered a range of wave intensities. Our method clearly outperformed the SWT and EEMD when applied to the synthetic and laboratory data; whereas all methods performed similarly when applied to the field data. This may be due to the fact that the field data had the largest wave intensity, and therefore the wave motion was relatively easy to isolate from the turbulence across all of the methods. A sensitivity analysis on the effect of wave intensity shows that the DMD method performs best when the wave energy is equal or greater than that of the turbulence. And given that the decomposition relies on isolating the coherent wave motion, the decomposition performs the worst for low wave intensity because the method is unable to identify the wave motion once it is overshadowed by stronger turbulence fluctuations.

The proposed method does require some manual tuning: specifically the user needs to input the shape of the time-delay matrix, the rank truncation, and the wave frequency range of interest. However, we argue that the parameters are physically related to the signal, especially compared to other methods such as the SWT and EEMD which have somewhat arbitrary tuning parameters. The rank truncation is discernible in the POD spectrum of the time-delayed input matrix, and the wave-frequency range is clearly visible in the power spectrum of the signal. While the number of time-delays is less clear, our sensitivity analysis shows that it is not as important to the accuracy of the decomposition, especially when the time-series length is long enough. We recommend future work to examine this parameter more closely and relate it directly to the wave spectrum. The reported parameters in table 2.2 can be a starting point for users of the method. Overall, the proposed DMD-based decomposition method is successful at decomposing wave and turbulence motion with minimal tuning and only one component of data, which is valuable for time-series measurements of flow parameters.

We have demonstrated that DMD is powerful for this application, and some fine tuning may need to occur as it is adopted for this problem. Future work can focus on more robust DMD schemes and alternative ways of determining the number of modes necessary to reconstruct the wave motion. A few examples include the extended DMD (Williams et al., 2015) which attempts to circumvent certain constraints of the (linear) DMD technique when decomposing data from nonlinear systems, and sparsity-promoting DMD (Jovanović et al., 2014) that can reduce the complexity of the calculations by identifying a smaller set of important DMD modes.

Chapter 3

DISPERSION AND RISE VELOCITY OF NEARLY-BUOYANT PARTICLES IN FREE-SURFACE BOUNDARY LAYER

This chapter is based on a manuscript in preparation: Chávez-Dorado, J., Baker, L., Riley, J., & DiBenedetto, M., "Vertical Transport of Nearly-Buoyant Particles in Free-Surface Boundary Layer," 2026.

3.1 *Introduction*

Particle transport in boundary layer flows is common in the environment, from sediment transport along river beds to bubbles and plastics at the ocean surface. While sediment transport in a bottom boundary layer is a well-studied system, the transport of buoyant particles in a wind-driven, free-surface boundary layer has received comparatively less attention. Even less studied are near-neutrally buoyant, but finite-size particles such as microplastics (DiBenedetto, 2026) and oil droplets (Boufadel et al., 2020). Understanding the vertical transport of these particles is especially important because it regulates shear-induced horizontal dispersion (Laxague et al., 2018) and determines their residence times at the surface, controlling exposure to sunlight and thereby photodegradation (Ward et al., 2019).

Predicting the vertical transport of buoyant particles typically requires accurate models for two quantities: the particles' turbulent diffusivity and their effective rise velocity. With respect to diffusivity, established models exist for diffusivity profiles throughout the mixed layer, but the near-surface wave layer remains challenging due to wave orbital motion, wave breaking, and Langmuir circulation (Qiao et al., 2016; Gerbi et al., 2009; D'Asaro, 2014). Additionally, the diffusivity of finite-size particles is not necessarily the same as that of fluid tracers. This difference is quantified by the turbulent Schmidt number $Sc_t = \nu_t/K$, the ratio of the eddy viscosity to the particle diffusivity.

In the sediment-transport literature, contrasting studies have reported both $Sc_t > 1$ and $Sc_t < 1$ (Gualtieri et al., 2017). This discrepancy can partly be attributed to the ways in which diffusivity is inferred from measurements. For example, when the diffusivity is indirectly measured from concentration profiles by assuming a still-water settling velocity, diffusivity can be over-estimated (Chauchat et al., 2022; Li et al., 2023). When the diffusivity is measured via direct measurements of the turbulent particle flux, one finds lower diffusivities and $Sc_t = 3 - 4$ for settling sand (Chauchat et al., 2022). This study also implies that the effective particle settling velocity is reduced relative to the quiescent value. Thus, the diffusivity estimates must be measured without assuming a settling (or rise) velocity.

With respect to the rise velocity, the quiescent rise velocity w_0 is not necessarily the same as the effective rise velocity of the particles in a flow. Several mechanisms can modify it. For example, buoyant particles can preferentially sample downwelling parts of the flow, either kinematically, by collecting in zones of surface convergence above downwelling (Stommel, 1949; Chor et al., 2018a; Yang et al., 2014) or dynamically, through inertial vortex trapping (Aliseda and Lasheras, 2011). Nonlinear drag can also reduce the drift of particles with finite particle Reynolds number (Good et al., 2014; Ruth et al., 2021), unsteady forces reduce it further for particles larger than the Kolmogorov scale (Li et al., 2023), and waves can modulate it directly (Clark et al., 2020; DiBenedetto et al., 2022). Large-eddy simulations of Langmuir turbulence with heavy non-inertial particles have shown reduced settling velocities due to the coherent structures (Noh et al., 2006; Chamecki et al., 2019). Thus, assuming a quiescent rise velocity may be inaccurate at the ocean surface.

For buoyant particles in steady state, the vertical concentration profile is set by a balance between upward advection due to the particles rising and downward turbulent flux due to mixing (Kukulka et al., 2012). A measured concentration profile therefore constrains only the ratio of rise velocity to the diffusivity, and any error in assumed rise velocity will map directly onto the inferred diffusivity (and vice versa). Transport by large coherent structures (e.g., Langmuir circulations) can enter this balance either as additional mixing via a nonlocal flux or as a change in the effective rise velocity (Smyth et al., 2002; Giordani et al., 2020). Thus, measurements of only concentration profiles can obscure the relevant processes affecting the particles; this motivates our use of particle tracking in our experiments. The diffusivity of particles is modulated by their interactions with the flow. For example, particles with a net drift (e.g. settling or rising due to gravity) experience the *crossing-trajectories* effect: they cross fluid pathlines as they drift causing their turbulent velocity fluctuations to decorrelate faster than that of a tracer particle, reducing their diffusivity even in the absence of particle inertia (Csanady, 1963). The drift velocity relative to the turbulent fluctuations, here defined as Rv (where Rv stands for rise velocity, but is identical to the Sv number commonly used to describe a non-dimensional settling velocity), is therefore a controlling parameter for the particle diffusivity. In contrast, particle inertia filters rapid fluctuations in the flow, which can increase the velocity decorrelation time and thereby enhance the particle's diffusivity relative to a tracer (Reeks, 1977; Squires and Eaton, 1991; Wetchagarun and Riley, 2010). These effects are commonly characterized by the Stokes number $St = \tau_p/\tau_\eta$, the ratio of the particle response time to a characteristic fluid timescale, and the size ratio $Sz = d_p/\ell_\eta$, the ratio of the particle size to the characteristic flow length scale. Most experiments on particle diffusivity mainly concern small, heavy particles in homogeneous isotropic turbulence (Balachandar and Eaton, 2010; Brandt and Coletti, 2022). Near-neutrally buoyant, finite-size particles are outside this regime; their density ratio makes inertial filtering weak (Berk and Coletti, 2024), but their size means they will filter the flow spatially (Qureshi et al., 2007). With respect to buoyant particles, buoyant droplets in isotropic turbulence showed reduced diffusivity consistent with the crossing-trajectories effect (Gopalan et al., 2008), and reduced rise velocities (Friedman and Katz, 2002), while finite-size floating particles in free-surface turbulence had reduced velocity fluctuations but longer correlation times, leading to only a weakly size-dependent diffusivity (Salmon et al., 2025). However, it remains to be seen how these results translate to buoyant particles in a wavy, turbulent flow.

In practice, particle diffusivity is estimated in one of two ways. Lagrangian methods follow the particles; e.g., Taylor (1922) relates the long-time (asymptotic) growth of particle displacements to the velocity correlation along their trajectories. This framework provides a direct measure of dispersion with no assumptions about the particle drift. However, this method requires measuring long trajectories to achieve converged statistics, measurements that are difficult to obtain in the field. Eulerian measurements instead interpret concentration profiles through the flux balance above, following sediment transport theory (Rouse, 1937). This approach has been adapted for microplastics at the ocean surface (Kukulka et al., 2012), where the near-surface diffusivity is often parametrized from wind and wave conditions or from large-eddy simulations, and the drift velocity is prescribed as the quiescent rise velocity (Kukulka and Brunner, 2015; Chor et al., 2018b; Chamecki et al., 2019). These inherently Eulerian models are widely used to interpret microplastics observations, but they have yet to be verified in the lab. Thus, we aim to study how the assumptions associated with these Eulerian closures compare against direct Lagrangian measurements.

In this study, we measure the vertical turbulent diffusivity of near-neutrally buoyant particles in a laboratory wind-driven, free-surface boundary layer directly from particle trajectories. We focus on the regime where particle rise velocity and turbulent fluctuations are similar in magnitude ($Rv \sim 1$), so that the particles are able to partially mix below the surface. We find that particle buoyancy is the primary control on the diffusivity, and that the crossing-trajectories theory of Csanady (1963) describes our measurements well, even for finite-size and non-spherical particles in the presence of waves. In contrast, we find that the quiescent rise velocity is a poor descriptor of the mean advective transport, and that the effective rise velocity is reduced far below w_0. The remainder of the paper is structured as follows: Section 3.2 outlines Lagrangian and Eulerian diffusivity estimations; Section 3.3 details the experimental setup, flow conditions, and particle properties; Section 3.4 presents and discusses the findings; and Section 3.5 summarizes the key results and their transport modeling implications.

3.2 *Background*

In this section, we review the approaches that we use to estimate particle turbulent diffusivity in our experiments, summarized at the end of this section in Table 3.1. The Lagrangian approach uses particle trajectories to estimate the diffusivity from the particle mean-square displacement (MSD). The Eulerian approaches use concentration profiles to estimate the diffusivity from the one-dimensional flux balance. We note that, while a true *Lagrangian* (or *fluid*) particle moves exactly with the flow and thus behaves as a tracer, here we use the term Lagrangian more loosely to refer to quantities defined along a particle trajectory, whether the particle is a tracer or not. Throughout, we assume the flow is statistically stationary and horizontally homogeneous, and we focus on the vertical dynamics with z positive upward and $z = 0$ defined at the mean water level.

First, we define the relevant particle velocities we refer to below. The quiescent rise velocity w_0 is the particle's terminal velocity in still water. The drift velocity w_r is the mean velocity of the particles relative to the mean velocity of the fluid; it is commonly assumed that $w_r = w_0$. For our particles, the effective rise velocity w_r is the drift velocity we infer from our measurements (§3.4.3). Finally, $\langle w_p \rangle$ is the measured ensemble-mean particle velocity, which vanishes in a statistically steady, vertically bounded system (§3.4.1).

3.2.1 (Lagrangian) particle trajectory approach

Dispersion is an inherently Lagrangian phenomenon. For a given particle, we denote its instantaneous vertical position by $z_p(t)$, and its displacement as

$$\Delta z_p(t) = z_p(t + t_0) - z_p(t_0), \tag{3.1}$$

where $z_p(t_0)$ is the initial position of the particle at time t_0. The most direct measure of the spread of an ensemble of particles comes from the long-time growth of the particle MSD, i.e., dispersion.

Einstein (1905) showed that the spread of a cloud of particles with uncorrelated motion, as measured by the MSD $\langle \Delta z_p^2(t) \rangle$, will grow linearly with time for sufficiently long times:

$$\langle \Delta z_p^2(t) \rangle \sim 2Kt, \tag{3.2}$$

where K is the particle diffusivity and $\langle \cdot \rangle$ denotes an ensemble average. Taylor (1922) extended this to particles with finitely correlated motion. To demonstrate, we define the displacement as the time-integral of the particle's vertical velocity $w_p(t)$:

$$\Delta z_p(t) = \int_0^t w_p(t')\, dt'. \tag{3.3}$$

Next, we decompose the velocity into the mean and fluctuation $w_p(t) = \langle w_p \rangle + w_p(t)$. For a statistically stationary flow with no mean vertical particle velocity ($\langle w_p \rangle = 0$), the MSD can be expressed in terms of the velocity autocovariance $\langle w_p(t) w_p(t+\tau)\rangle$:

$$\langle \Delta z_p^2(t)\rangle = 2\int_0^t (t-\tau)\langle w_p(t) w_p(t+\tau)\rangle \, d\tau. \tag{3.4}$$

We note that even in flows with zero mean, finite-sized particles can preferentially sample the flow, which can yield a non-zero mean drift $\langle w_p\rangle \neq 0$ in an unbounded flow. We will revisit these implications later in this section.

We can relate the MSD to the Lagrangian integral time scale T_L which is defined as

$$T_L = \int_0^\infty \rho_{ww} \, d\tau, \quad \text{where} \quad \rho_{ww} = \frac{\langle w_p(t) w_p(t+\tau)\rangle}{\langle w_p^2\rangle} \tag{3.5}$$

is the Lagrangian velocity autocorrelation. From this expression we see the two classic limiting regimes for (3.4): the *ballistic* and the *diffusive* regimes. In the ballistic regime ($t \ll T_L$), the velocity remains correlated ($\rho_{ww} \approx 1$), and the MSD grows quadratically in time, $\langle \Delta z_p^2\rangle \approx 2\langle w_p^2\rangle\, t^2$. In the diffusive ($t \gg T_L$) regime, the velocity fluctuations become uncorrelated and the MSD grows linearly in time, $\langle \Delta z_p^2\rangle \approx 2\langle w_p^2\rangle\, T_L t$. The time derivative of the MSD thus approaches a constant over sufficiently long times:

$$\lim_{t\to\infty} \frac{d}{dt}\langle \Delta z_p^2(t)\rangle = \int_0^\infty \langle w_p(t) w_p(t+\tau)\rangle \, d\tau = 2K. \tag{3.6}$$

This yields an asymptotic definition of turbulent (vertical) diffusivity based on particle dispersion:

$$K_A = \lim_{t\to\infty} \frac{1}{2}\frac{d}{dt}\langle \Delta z_p^2(t)\rangle. \tag{3.7}$$

Equivalently, from (3.5) and (3.6), the diffusivity can be expressed in terms of the Lagrangian integral time scale as

$$K = \int_0^\infty \langle w_p(t) w_p(t+\tau)\rangle \, d\tau = \langle w_p^2\rangle T_L. \tag{3.8}$$

Equations 3.7 and 3.8 are equivalent definitions of the same diffusivity, assuming statistical stationarity (the autocorrelation depends only on the time lag τ), homogeneity (a single K characterizes the region sampled by the particle trajectories), and the existence of a diffusive regime. These assumptions can break down in boundary layers where ρ_{ww} and T_L can vary with depth.

Effects of drift velocity

Next, we consider turbulent diffusivity in the context of particles with a mean drift. Non-fluid particles can have a mean vertical drift velocity associated with gravity. Alternatively, the flow may have a non-zero mean flow. In either case, equation 3.3 becomes:

$$\Delta z_p(t) = \langle w_p \rangle t + \int_0^t w_p(t')\, dt',$$

where $\langle w_p \rangle$ is some constant, consistent with the assumptions of homogeneity and stationarity above. Therefore, (3.4) generalizes to:

$$\langle \Delta z_p^2(t) \rangle = \langle w_p \rangle^2 t^2 + 2 \int_0^t (t - \tau) \langle w_p(t) w_p(t + \tau) \rangle \, d\tau, \tag{3.9}$$

and the diffusive limit is

$$\frac{1}{2} \frac{d}{dt} \langle \Delta z_p^2(t) \rangle = \langle w_p \rangle^2 t + \int_0^t \langle w_p(t) w_p(t') \rangle \, dt'. \tag{3.10}$$

The drift term $\langle w_p \rangle^2 t$ represents the "ballistic" contribution to the variance of the particle position relative to the origin, caused by the non-zero mean drift and/or a non-zero mean flow. If the MSD is calculated relative to a frame of reference moving with the drift, this term vanishes and we recover the Taylor result.

There are now two conditions to be met for (3.7) to be used to compute the diffusivity K. The first is that time t is large enough that the integral in (3.10) has become a constant, i.e., approximately, $t > T_L$, and the second is that time is short enough so that the first term in (3.10) does not dominate the second, i.e., approximately $\langle w_p^2 \rangle T_L > \langle w_p \rangle^2 t$. Taken together, these conditions give:

$$\frac{\langle w_p^2 \rangle}{\langle w_p \rangle^2} T_L > t > T_L, \tag{3.11}$$

or, since $t > T_L$ is necessary,

$$\frac{\langle w_p^2 \rangle}{\langle w_p \rangle^2} > 1. \tag{3.12}$$

We evaluate this condition for our experiments in §3.4.1.

Additionally, the crossing-trajectories effect becomes important when particles experience a net drift velocity relative to the fluid (Yudine, 1959; Csanady, 1963). This effect is governed by the velocity ratio

$$Rv = \frac{w_0}{v_f}, \tag{3.13}$$

where v_f is a characteristic velocity scale of the flow (in our experiments, we use $v_f = w_{\mathrm{rms}}$). A finite drift velocity causes a particle to travel through an eddy more quickly than a fluid element, reducing its correlation time and hence the diffusivity. Csanady (1963) showed that, for dispersion in the drift direction, the crossing-trajectories effect can be captured by a ratio of particle-to-fluid diffusivity K/K_f:

$$\frac{K}{K_f} = \left(1 + \frac{C^2 w_0^2}{\langle w_f'^2 \rangle}\right)^{-1/2}. \tag{3.14}$$

Here, C can be interpreted as the ratio between the Lagrangian memory time of the fluid and the time required for drift to carry a particle across an Eulerian turbulent structure. This means that a larger C produces a stronger reduction in diffusivity because the particle crosses an Eulerian correlation length faster than the fluid Lagrangian correlation time. The constant C is not universal and reported values ($C = 0.3$–22) span orders of magnitude across flows (see Snyder and Lumley, 1971; Wells and Stock, 1983; Sato and Yamamoto, 1987; Burnage and Huilier, 1990; Mazzitelli and Lohse, 2004; Aiyer and Meneveau, 2022, for specific values).

Effects of inertia and finite-size

In addition to drift, particle inertia and finite size can modify diffusivity by changing the two parameters in (3.8). Inertia and finite size can filter high-frequency fluctuations, reducing the velocity variance $\langle w_p^2 \rangle$ while increasing the correlation time T_L, so the net effect on K can be of either sign.

In homogeneous isotropic turbulence, inertia alone can increase the diffusivity of heavy particles at low Stokes numbers (Reeks, 1977), with a weak decrease for $St \gtrsim 1$ (Wetchagarun and Riley, 2010). Nir and Pismen (1979) extended the analysis by Csanady (1963) and Reeks (1977) to include both a steady drift and inertia (via a linear drag), showing that the crossing-trajectories effect dominates, reducing the vertical diffusivity. A further extension showed that nonlinear drag can further reduce the drift and diffusivity (Mei et al., 1997). These results are generalized to arbitrary inertia, although no closed-form expression exists (Boi et al., 2018).

For near-neutrally buoyant particles, however, inertial filtering is expected to be weak regardless of the response time. As the density ratio approaches unity, added-mass and pressure-gradient forces become relatively large and a small particle's frequency response approaches that of a tracer (Zhang et al., 2019; Berk and Coletti, 2024). Considering finite size, a particle of size d_p averages the fluid motion over its volume and filters eddies smaller than itself, a spatial rather than temporal filtering (Qureshi et al., 2007; Bec et al., 2007; Toschi and Bodenschatz, 2009). We therefore expect drift, rather than inertia, to dominate the modulation of diffusivity in our regime, with finite size acting as a secondary effect. We define the corresponding dimensionless parameters (St, Sz) with the appropriate flow scales for our finite-size particles in §3.3.3.

3.2.2 (Eulerian) concentration-profile methods

In practice, sediments and other particulate phases are typically modeled with an Eulerian conservation equation. Neglecting molecular diffusion (large Péclet number), the ensemble-averaged conservation equation for the vertical concentration of an ensemble of particles $c(z,t)$ is

$$\frac{\partial \langle c \rangle}{\partial t} + \frac{\partial}{\partial z}\big(\langle w_p \rangle \langle c \rangle + \langle w_p c' \rangle\big) = 0, \tag{3.15}$$

where $c = \langle c \rangle + c'$ and $w_p = \langle w_p \rangle + w_p$ are the Reynolds decompositions of concentration and vertical particle velocity, and the mean vertical particle velocity accounts for the combined effects of the mean fluid velocity and the particle drift, $\langle w_p \rangle = \langle w_f \rangle + w_r$.

Next, we parametrize the turbulent flux $\langle w_p c' \rangle$ via the gradient-diffusion closure

$$\langle w_p c' \rangle = -K \frac{\partial \langle c \rangle}{\partial z}, \tag{3.16}$$

assuming that the turbulent flux is proportional to the local concentration gradient. This, however, might not hold if larger scale motions (e.g., Langmuir circulation) exist, which can contribute to nonlocal vertical mixing (Farmer and Li, 1994). Assuming zero mean fluid velocity ($\langle w_f \rangle = 0$) and constant drift w_r, we have

$$\frac{\partial \langle c \rangle}{\partial t} + w_r \frac{\partial \langle c \rangle}{\partial z} = \frac{\partial}{\partial z}\left(K \frac{\partial \langle c \rangle}{\partial z} \right), \tag{3.17}$$

where $K(z,t)$ is an effective vertical eddy diffusivity.

We note that the Eulerian description above and the Lagrangian MSD approach are two representations of the same transport process (see Appendix 3.6.3). The diffusivity in (3.17) equals the long-time growth rate of the MSD (Majda and Kramer, 1999) for a cloud of dispersing particles. This equivalence is related to the assumptions of gradient diffusion and the existence of a diffusive regime. When these assumption holds and the drift velocity is known, the Lagrangian and Eulerian estimates should agree. Disagreement is therefore due to a failure of the underlying assumptions or an error in the drift velocity, rather than a difference in how the diffusivities are defined. We will compare these approaches in §3.4.

Eulerian approaches to diffusivity

Next, we assume steady state, such that equation 3.17 becomes

$$w_r \frac{\partial \langle c \rangle}{\partial z} = \frac{\partial}{\partial z}\left(K \frac{\partial \langle c \rangle}{\partial z} \right). \tag{3.18}$$

Given the condition of no net flux through the boundaries, the vertical flux throughout the water column is zero:

$$0 = w_r \langle c \rangle - K \frac{d\langle c \rangle}{dz}. \tag{3.19}$$

Now, we can use equation 3.19 to estimate diffusivity K_F, which we refer to as the flux-estimate:

$$K_F = \frac{w_r \langle c \rangle}{d\langle c \rangle / dz}. \tag{3.20}$$

This diffusivity K_F can be calculated directly from the concentration profile over depth, given w_r. When w_r is not known, the quiescent rise velocity is typically used (Kukulka et al., 2012; Brunner et al., 2015).

The steady-state concentration profile is found by integrating (3.19),

$$\langle c \rangle(z) = c_0 \exp\left(\int_0^z \frac{w_r}{K}\, dz\right). \tag{3.21}$$

Further assuming that w_r and K are constant over depth (i.e. $w_r = w_0$) yields the closed form solution

$$\langle c \rangle(z) = c_0 \exp\left(\frac{w_0 z}{K}\right), \tag{3.22}$$

where c_0 is the surface concentration. Equation 3.22 describes a profile with maximum concentration of particles at the surface decaying with depth at the rate w_0/K, which defines a single mixing length scale ℓ_m

$$\ell_m = \frac{K}{w_0}, \tag{3.23}$$

characterizing the vertical extent over which the particles are mixed. If we fit an exponential profile to the particle concentration and know w_0, we have another method to estimate the turbulent diffusivity

$$K_C = \ell_m\, w_0. \tag{3.24}$$

We refer to this as the concentration profile estimate. In principle, another way to estimate directly K is from inverting the gradient-diffusion closure (3.16) using the measured turbulent flux $\langle w_p c' \rangle$ rather than the mean flux. However, $\langle w_p c' \rangle$ is challenging to measure because it requires simultaneous measurements of velocity and concentration fluctuations at the same location, with sufficient averaging to reduce noise; we do not attempt it here.

Finally, the particle diffusivity is often parameterized from the momentum transport using the Reynolds analogy, which relates K to the eddy viscosity ν_t via the turbulent Schmidt number $Sc_t = \nu_t/K$, such that

$$K_V = \frac{\nu_t}{Sc_t}, \tag{3.25}$$

where, in the absence of a measured or modeled value, Sc_t is typically set to unity assuming that turbulence tends to mix all things equally. This approach is useful in sediment transport because well-established turbulence models already exist to parametrize the eddy viscosity in a solid-wall boundary layer. Since comparable models are not established for free-surface boundary layers, we can estimate ν_t directly from the momentum flux and the mean shear as

$$\nu_t = -\frac{\langle u'w' \rangle}{\partial \langle u \rangle / \partial z}. \tag{3.26}$$

While this direct estimation avoids empirical modeling biases, it assumes that the turbulent flux is driven by the local gradient, and it is susceptible to singularities where the shear vanishes.

3.2.3 Summary

Formula	Principle	Assumptions	Input Data
$K_A = \frac{1}{2}\frac{d\langle \Delta z_p^2 \rangle}{dt}$	*Asymptotic*: Long-time growth rate of particle mean-square displacement	Homogeneous, stationary turbulence; $w_0/w_{\mathrm{rms}} \ll 1$; diffusive regime for $t \gg T_L$	$z_p(t)$
$K_C = \ell_m w_0$	*Concentration-profile*: Balance between upward buoyant drift and downward turbulent mixing	Constant K; diffusive mixing	$\langle c \rangle(z)$; w_0
$K_F = \frac{w_r \langle c \rangle}{d\langle c \rangle / dz}$	*Flux*: Balance between local buoyant flux to the local turbulent gradient flux	Steady state; local equilibrium (flux proportional to gradient)	$\langle c \rangle(z)$; $d\langle c \rangle/dz$; w_r
$K_V = \frac{\nu_t}{Sc_t}$	*Viscosity*: Particle turbulent diffusivity proportional to momentum turbulent diffusivity	Gradient diffusion holds; known eddy viscosity; Sc_t often assumed	$\nu_t(z)$; Sc_t

Table 3.1: Summary of core formulas, principles, and input data to estimate vertical turbulent diffusivity K in our experiments.

The approaches above estimate the same vertical turbulent diffusivity K from different data under different assumptions. The Lagrangian method (K_A) uses particle trajectories and requires no model for the particle drift velocity or turbulent flux. The Eulerian approaches (K_F, K_C, K_V) use concentration profile data and/or velocity statistics and assume a gradient diffusion model. K_F and K_C also assume a prescribed drift velocity (typically $w_r = w_0$). Thus, these estimates can fail if the particle's effective rise velocity deviates from its quiescent value, or if the nonlocal diffusion becomes important. Table 3.1 summarizes the core formulas, underlying physical principles, necessary assumptions, and required input data for each method we test in our study.

3.3 *Methodology*

3.3.1 Experimental setup

Our experiments take place in the Washington Air-Sea Interaction Research Facility, a water channel with a test section 12.2 m long, 0.91 m wide, and 1.22 m high. The channel is filled with tap water to a depth of 0.6 m leaving 0.6 m of headspace for airflow from the closed-loop wind tunnel above. Wind stress on the surface generates a young sea state with deep-water waves and drives a slow mean current. We install a sloped foam beach at the downstream end to absorb wave energy and to minimize reflections.

Because we are studying particle vertical dispersion, we require observations of vertical particle displacements over long times. Thus, we need to measure particle trajectories over a sufficiently large field of view. We use large-scale shadow tracking (LSST), a technique introduced in Baker and DiBenedetto (2023), which measures 2D projections of particle trajectories within a 3D volume by tracking particle shadows from a collimated light source. With this technique, we can directly measure the particles' streamwise and vertical positions (x and z), while the spanwise (y) position remains unknown. Note, we define $z = 0$ to be the mean free surface with z positive upward. The LSST system uses four cameras to form a 1 m $\times$ 0.45 m field of view with an average resolution of 9 pixels/mm such that we can resolve the shadows of particles with diameters as small as 2 mm. The light source is a 470 nm light-emitting diode (LED) collimated through a large Fresnel lens (1 m $\times$ 0.7 m) positioned on the glass sidewall of the tank. The field of view is located 7 m downstream from the test-section inlet, and we capture images at a rate of 30 Hz. We only can measure submerged particles, and therefore trajectories terminate once particles reach the surface. For further setup and equipment details, see Baker and DiBenedetto (2023).

Because LSST only measures projections of particle trajectories, we characterized the flow separately. We measured vertical profiles of all three fluid velocity components (u, v, and w) collected at multiple depths using a Nortek Vectrino acoustic Doppler velocimetry profiler (ADV). The ADV was mounted above the tank centered within the LSST volume. At each measurement point, the ADV resolves the flow at eight vertical cells spaced 4 mm apart, and a Cartesian robot traversed the ADV across the full water depth. At each measurement location, we sampled at 50 Hz for 2 minutes. To avoid bias in the Reynolds stress estimates (Trowbridge, 1998), the ADV's coordinates were rotated into the laboratory frame using a rotation matrix obtained from a singular value decomposition of calibration-run velocity measurements, with the principal axis of maximum variance defining the streamwise direction. We denoised the velocity signals using signal-to-noise ratio and correlation thresholds of 5 and 40, respectively, and rejected measurements within 6 mm of the free surface (detected by the acoustic backscatter) to avoid contamination by surface echoes. We additionally measured the free-surface elevation ζ using single-point U-GAGE T30X acoustic wave gauge, located at the upstream edge of the LSST volume. It recorded continuously for 5 minutes at a sampling rate of 400 Hz, and then it was decimated to 100 Hz during postprocessing.

3.3.2 Flow characterization

Here, we characterize both the turbulence and the wave field. We plot the power spectral density for the surface elevation $S_{\zeta\zeta}$ and the vertical velocity fluctuations S_{ww} (depth-averaged over the upper 30 cm) in figure 3.1 for each wind speed. The spectra were estimated using Welch's method (segment averaging with a Hanning window and 50% overlap). The elevation spectra (figure 3.1a) peak at 2.34 Hz (12 m/s) and 1.95 Hz (16 m/s). The velocity spectra (figure 3.1b) peak at 2.15 Hz (12 m/s) and 1.66 Hz (16 m/s). Note that the velocity spectra peak at slightly lower frequencies because of the depth-averaging. The 16 m/s wind speed case has a broader spectrum with more energy at lower frequencies, consistent with a more developed wave field. The higher harmonics are consistent with bound harmonics of the steep waves at the peak frequency, but also

Wind speed (m/s)	12	16
h (cm)	60.0 ± 1.0	60.0 ± 1.0
H_s (m)	3.0 ± 0.9	5.3 ± 0.9
a_s (cm)	1.5 ± 0.5	2.6 ± 0.5
f_p (Hz)	2.34 ± 0.02	2.05 ± 0.02
c_p (m/s)	0.67 ± 0.02	0.80 ± 0.03
k_p (rad/m)	22.01 ± 0.04	16.89 ± 0.04
λ_p (m)	0.28 ± 0.02	0.41 ± 0.02
$k_p h$ (–)	13.22 ± 0.50	9.21 ± 0.50
U_S (cm/s)	7.5 ± 0.2	15.6 ± 0.2
u_* (cm/s)	2.6 ± 0.4	3.2 ± 0.4
La (–)	0.6 ± 0.2	0.5 ± 0.2

Table 3.2: Wave and turbulence parameters for experiments conducted at wind speeds of 12 and 16 m/s. Wave properties and uncertainties are estimated from the vertical velocity spectra, while turbulence statistics and uncertainties are computed from near-surface fluid velocity time series.

potentially representative of wave-modulated turbulence (Thais and Magnaudet, 1996; Guo and Shen, 2013).Figure 3.1b also shows a $-5/3$ power-law decay at higher frequencies, characteristic of a developed turbulent inertial range.

The peak frequency f_p is identified as the peak of the surface elevation power spectrum $S_{\zeta\zeta}(f)$ in figure 3.1a. We also compute the peak angular wave frequency $\omega_p = 2\pi f_p$, the peak wavenumber $k_p = \omega_p^2/g$ (using the deep-water wave dispersion relation), the peak wavelength $\lambda_p = 2\pi/k_p$, and peak the wave phase speed $c_p = g/\omega_p$. We also measure the significant wave height $H_s = 4(\int S_{\zeta\zeta}(f)\, df)^{1/2}$. These parameters are reported in the upper part of table 3.2; their uncertainties were obtained from the 95% confidence interval of the averaged spectral estimates.

Next, we calculate the mean and turbulent flow statistics. We obtain the mean velocity pro-

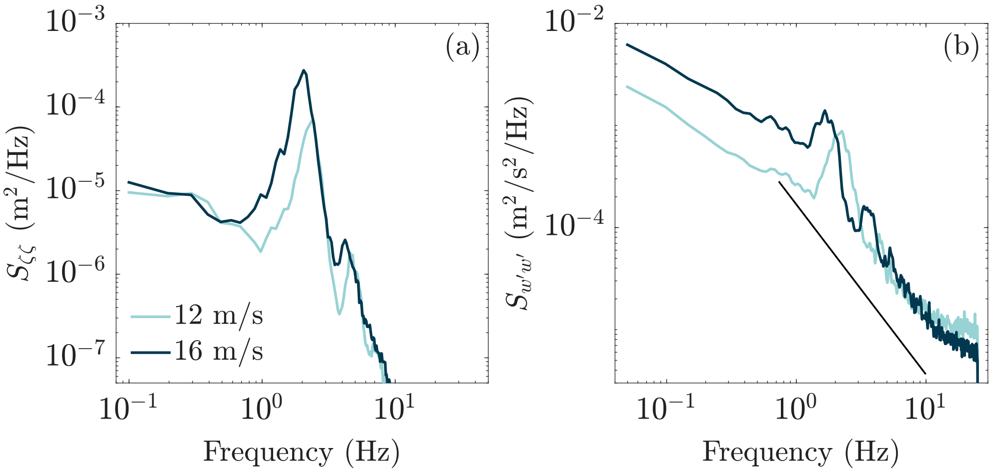

Figure 3.1: Power spectrum of (a) surface elevation $S_{\zeta\zeta}$ and (b) depth-averaged vertical velocity S_{ww} for experiments conducted under 12 m/s and 16 m/s wind conditions. The straight black line in (b) has a $-5/3$ slope.

files $\langle u \rangle$ and $\langle w \rangle$ directly from the velocity time series. However, to characterize the turbulent fluctuations, we need to first isolate them from the wave fluctuations. Our approach is to remove wave-induced motion from the velocity signals using a dynamic mode decomposition (DMD)-based wave-turbulence separation method that we developed in Chávez-Dorado et al. (2025). Given a 1-D velocity time series, this separation method first constructs a Hankel-like delay matrix to overcome dimensionality limitations of DMD and then applies DMD to decompose the matrix into a set of modes with well-defined complex frequencies where the coherent modes around the dominant wave frequency are identified as the wave component. Subtracting these reconstructed wave modes from the original time-series yields a residual time-series dominated by turbulence. For our data, we constructed time-delay matrices with shape 4000×2000 from the u and w time series and reconstructed the wave signal from the first 200 DMD modes. Figure 3.2 shows that this separation algorithm is able to successfully isolate the wave frequency band including higher harmonics, while preserving the turbulence. From these turbulence velocity signals we quantify profiles of the horizontal and vertical velocity fluctuation root-mean-square (RMS) u_{rms}, w_{rms} and the Reynolds stress $\langle u'w' \rangle$.

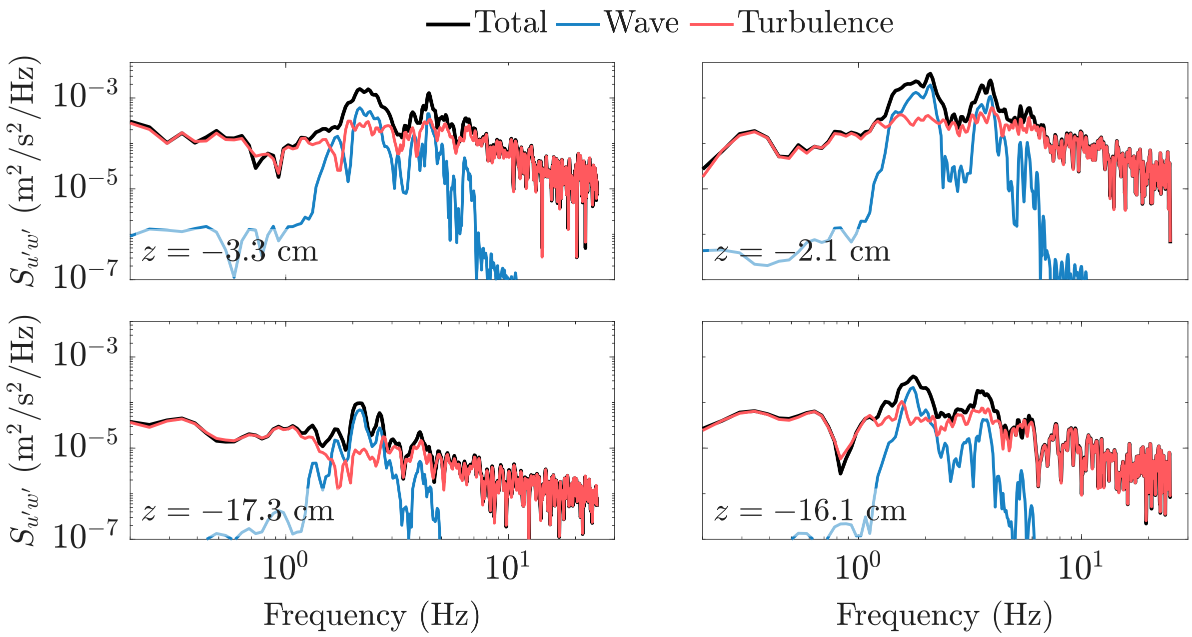

Figure 3.2: Power spectrum of Reynolds stress from the raw, wave-, and turbulence-only contribution used to assess the effectiveness of the DMD-based separation algorithm. The spectra were checked at two different depths, seen in the lower left corner of each subfigure, for 12 m/s (left column) and 16 m/s (right column).

We plot the mean horizontal velocity profile in figure 3.3a where we see a sheared mean current with a reverse current near the bottom that sets up due to the confinement of the tank. For this reason, we restrict our analysis to the upper 30 cm of the water column. Below this depth, the mean velocity gradient (needed for the eddy viscosity estimation) approaches zero and changes sign because of the flow reversal, making the eddy viscosity physically uninterpretable. We apply the same depth restriction to all statistics to maintain a consistent sampling domain. In figure 3.3b we plot the vertical profiles of turbulent RMS velocities, showing the highest turbulent fluctuations near the surface. We plot the Reynolds shear stresses over depth in figure 3.3c, showing both the components due to the waves and the turbulent fluctuations separately. As expected, the main contributions to the shear stress come from the turbulence and not the waves, consistent with similar wind-driven flows (Cheung and Street, 1988; Thais and Magnaudet, 1996; Terray et al., 1996). Note

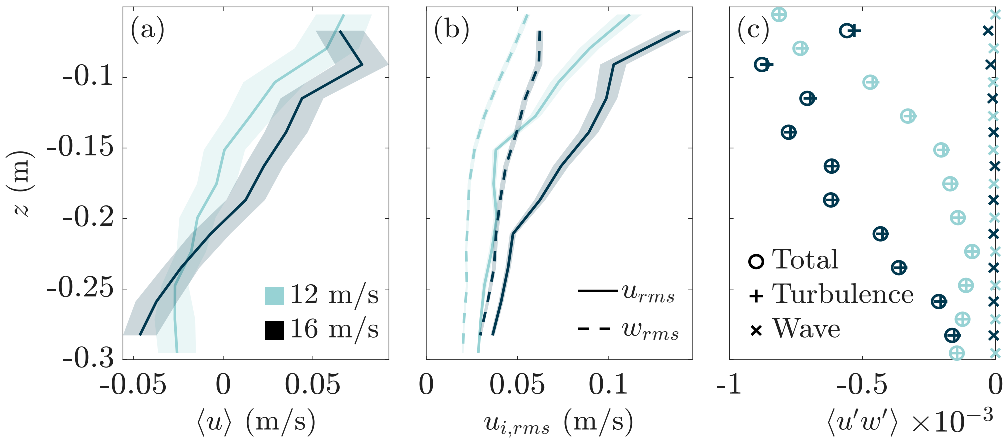

Figure 3.3: Mean velocity profiles for experiments conducted under 12 m/s and 16 m/s wind conditions. The shaded regions show the 95% confidence interval derived from bootstrapping. (a) Time-averaged streamwise and vertical velocity profiles $\langle u \rangle(z)$ and $\langle w \rangle(z)$, respectively, for wind forcing at 12 and 16 m/s. (b) Corresponding streamwise and vertical velocity RMS profiles $u_{\text{rms}}(z)$ and $w_{\text{rms}}(z)$.

that this result also helps show the success of our wave-turbulence decomposition.

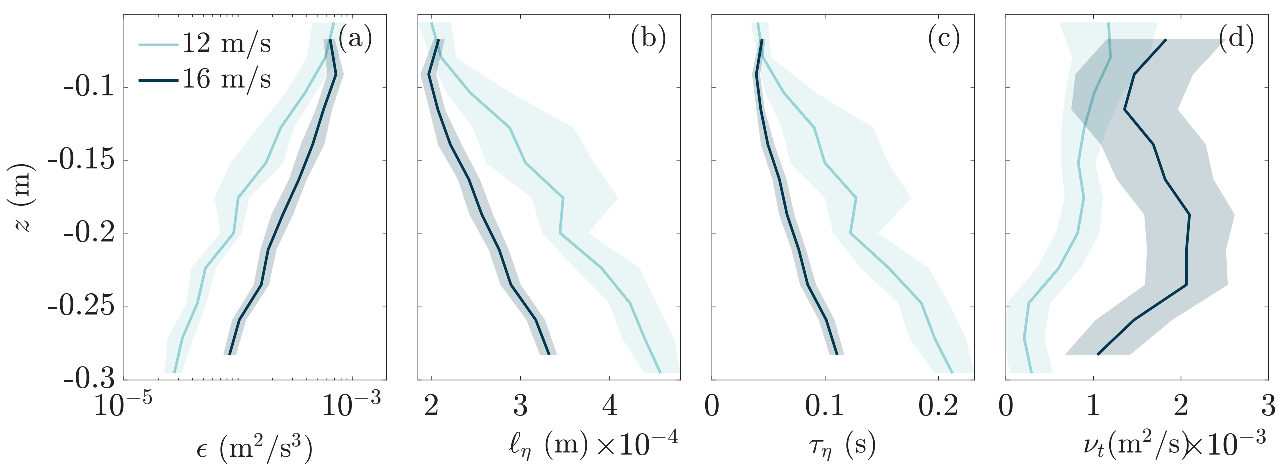

Figure 3.4: Vertical profiles of (a) turbulent dissipation using (Gerbi et al., 2009), (b) Kolmogorov length scale and (c) time scale and (d) eddy viscosity from (3.26).

In figure 3.4 we plot estimates of the turbulent dissipation, Kolmogorov length and timecales, and eddy viscosity. We estimate the dissipation rate ε as a function of depth using inertial-subrange spectral fitting following Terray et al. (1996) and Gerbi et al. (2009). Given the kinematic viscosity $\nu = 10^{-6}$ m^2/s, we also calculate the Kolmogorov lengthscale $\ell_\eta = \left(\frac{\nu^3}{\varepsilon}\right)^{1/4}$ and timescale $\tau_\eta = \left(\frac{\nu}{\varepsilon}\right)^{1/2}$. We estimate eddy viscosity ν_t with equation 3.26. As expected, we see that in figure 3.4, ε decreases with depth given that turbulence is generated near the water surface. Thus, ℓ_η and τ_η both increase with depth, indicating that the smallest scale eddies occur near the surface, as expected. These dissipation values are consistent with field measurements in 14 m/s winds (Gemmrich and Farmer, 2004). In contrast, we see that ν_t is relatively constant over depth. This differs from a classic wall scaling, but is instead consistent with the more uniform mixing expected under a wave layer (Gerbi et al., 2009; Kukulka and Brunner, 2015; Craig and Banner, 1994).

Finally, we characterize the relative importance of waves and turbulence with the Langmuir number $La = (u_*/U_S)^{1/2}$, defined with the water friction velocity u_* and the surface Stokes drift velocity U_S. We estimate the friction velocity $u_* = \sqrt{|\langle u'w' \rangle|}$,using values measured at 5 cm below the mean water level to avoid contamination by the wave layer. The Stokes drift velocity is estimated from the wave amplitude spectrum:

$$U_S = 2 \int \omega k S_{\zeta\zeta}(f)\, df, \tag{3.27}$$

as in Kumar et al. (2017). Small values of La indicate that waves dominate over shear-driven turbulence, whereas large values indicate a shear-dominated regime. For reference, we report u_*, U_S, and La for each wind speed in table 3.2. We find La values of $0.5 - 0.6$, indicating wave influence, but no fully developed Langmuir circulation. For reference, Li et al. (2005) concludes that, for a developed flow, Langmuir turbulence dominates for $La \lesssim 0.3$. Compared to equilibrium open-ocean conditions which often have more wave influence with $La \approx 0.2$–0.5 (Fisher and Nidzieko, 2024), our values are near the shear-dominated regime. In our experiments, the La values suggests that Langmuir turbulence is not expected to be a strong effect.

3.3.3 Particles

[htb!]

We use buoyant particles chosen to target an intermediate regime where their buoyancy is strong enough relative to the turbulence that they do not behave as uniformly-mixed tracers, yet weak enough that the turbulence is able to mix them below the free surface. The particles are high-density polyethylene (HDPE) particles with specific gravity $SG = \rho_p/\rho_f = 0.96$ in three shapes (spheres, rods and disks). We also use particles that we made out of Carnauba-wax ($SG = 0.997$) that approximate a tracer and here on referred to as *neutral* particles.

The particles' shape is characterized by the aspect ratio $\Phi = p_{\parallel}/p_{\perp}$, where $p_{\parallel}$ denotes the length of the axis of rotational symmetry and $p_{\perp}$ the characteristic length of the perpendicular axes. The spheres (aspect ratio $\Phi = 1$) have diameters of 2.0 mm, 2.5 mm (precision spheres, Cospheric) and 3.9 mm (nurdles, McMaster-Carr). The rods (prolate, $\Phi > 1$) were made by cutting 3D-printer filament with a 1.75 mm diameter into segments with average length 10.7 mm and 20.2 mm, giving aspect ratios of 6.1 and 11.5. The disks (oblate, $\Phi < 1$) were die-cut from 0.79 mm-thick HDPE sheets with diameters of 5.0 mm, 7.0 mm and 10.0 mm, corresponding to aspect ratios of 0.16, 0.11 and 0.08. The neutral particles are cylinders with both an equal height and diameter of 2.7 mm ($\Phi = 1$). For non-spherical particles we define them by their volume-equivalent diameter, $d_p = (1.5 p_{\perp}^2 p_{\parallel})^{1/3}$. The particle properties are summarized in table 3.3. Because the particles are hydrophobic, before each experiment we soak them in water with a few drops of dish soap to prevent air bubbles from adhering when we introduced them to the tank.

We measured the particles' terminal rise velocity in quiescent water. We released particles one at a time in a rectangular tank measuring 25 cm × 25 cm × 100 cm high. For each particle shape and size, 15 realizations were performed by selecting particles at random with replacement from a set of 20 (where each particle class had at least 50 total particles). After removing any attached air bubbles, we lowered the particle to the bottom of the tank using a claw grabber and released it after the fluid had come to rest. The rods and disks oscillated laterally during their rise due to shedding vortices given their intermediate Reynolds number. We recorded the particles at 30 fps over a 15 x

Wind speed	Parameter	Small spheres	Medium spheres	Large spheres	Small disks	Medium disks	Large disks	Medium rods	Large rods	Neutral
0 m/s	d_p (mm)	2.0 ± 0.1	2.5 ± 0.1	3.9 ± 0.3	3.1 ± 0.1	3.9 ± 0.1	4.9 ± 0.1	3.7 ± 0.1	4.6 ± 0.2	2.7 ± 0.3
	w_0 (cm/s)	2.7 ± 0.1	3.7 ± 0.1	5.5 ± 0.1	2.3 ± 0.1	2.5 ± 0.1	2.6 ± 0.1	3.5 ± 0.1	3.7 ± 0.1	0.1 ± 0.1
	ρ_p (kg/m^3)	960 ± 1	960 ± 1	960 ± 1	960 ± 1	960 ± 1	960 ± 1	960 ± 1	960 ± 1	997 ± 1
	τ_p (ms)	97 ± 3	136 ± 4	203 ± 6	86 ± 3	92 ± 3	97 ± 5	129 ± 4	136 ± 4	69 ± 4
	Re_p (–)	60 ± 3	104 ± 6	243 ± 27	71 ± 7	95 ± 9	301 ± 10	129 ± 5	128 ± 7	4 ± 3
	Ga (–)	69 ± 5	97 ± 5	190 ± 17	114 ± 5	151 ± 6	216 ± 7	134 ± 3	217 ± 3	22 ± 4
12 m/s	St_c (–)	0.3 ± 0.1	0.4 ± 0.1	0.6 ± 0.1	0.3 ± 0.2	0.2 ± 0.2	0.2 ± 0.2	0.4 ± 0.1	0.4 ± 0.1	0.1 ± 0.1
	Rv (–)	0.9 ± 0.3	1.2 ± 0.3	1.9 ± 0.5	0.7 ± 0.1	0.8 ± 0.3	0.8 ± 0.3	0.9 ± 0.5	1.1 ± 0.4	0.06 ± 0.30
	Sz (–)	9 ± 3	11 ± 3	22 ± 3	13 ± 4	15 ± 5	19 ± 6	16 ± 4	20 ± 6	9 ± 3
16 m/s	St_c (–)	0.4 ± 0.1	0.4 ± 0.2	0.5 ± 0.1	0.3 ± 0.1	0.2 ± 0.1	0.2 ± 0.1	0.3 ± 0.1	0.3 ± 0.1	0.2 ± 0.1
	Rv (–)	0.6 ± 0.2	0.8 ± 0.2	1.0 ± 0.3	0.5 ± 0.2	0.5 ± 0.1	0.5 ± 0.2	0.7 ± 0.2	0.7 ± 0.3	0.03 ± 0.10
	Sz (–)	9 ± 2	12 ± 2	20 ± 3	13 ± 3	16 ± 3	21 ± 4	16 ± 3	20 ± 3	12 ± 3

Table 3.3: Summary of the particle characteristics in quiescent water and wind-driven surface boundary layer for 12 and 16 m/s. For quiescent conditions (0 m/s), the error bounds represent the measurement tolerances for particle physical properties (such as diameter and density) and confidence intervals of terminal rise velocity across multiple releases of particles in still water. The uncertainty for the non-dimensional parameters is calculated through error propagation. For wind-driven conditions (> 0 m/s), the error bounds represent standard deviation due to the spread of the particles' vertical positions through the water column.

15 cm field of view centered 15 cm below the free surface. We computed the time-averaged vertical velocity of each realization within the field of view, checking that the temporal standard deviation was small relative to the mean (less than 10% for all cases) ensuring that the particles had reached their terminal velocity. We report the average terminal velocities of the particles in Table 3.3.

We characterize the particles and estimate relevant non-dimensional parameters in both still fluid and the turbulent flow in the experiments. We begin with the still fluid characterization, calculating both the particle Reynolds number $Re_p = w_0 d_p/\nu$ and the Galileo number $Ga = \sqrt{|\rho_p/\rho_f - 1|\, g\, d_p^3}/\nu$. Re_p quantifies the relative importance of inertial to viscous forces in the fluid surrounding a particle, and Ga quantifies the relative importance of particle buoyancy to viscous forces. We also compute the density parameter $\beta = (1 + C_m)/(\rho_p/\rho_f + C_m)$, where C_m is the orientation-averaged added mass coefficient. For each particle shape, we estimate the C_m from the classical solution for spheroids in potential flow (Lamb, 1930). We report these values for all particle geometries and wind speeds in table 3.3. The Re_p ranges from 4 (neutral) to 301 (large disk) and indicates that for many of the cases, the drag is in a nonlinear regime. This range is similar to reported values for real microplastics, which also have variable shape (DiBenedetto et al., 2023). For the nonspherical particles, the Galileo numbers ($Ga \approx 100$–220) indicates path instabilities (Fernandes et al., 2007), consistent with the wobbling trajectories observed during the terminal velocity measurements. The resulting β values fall within a narrow range close to one ($\beta = 1$–1.02, within experimental uncertainty), which means that particle inertia effects in turbulence are likely to be minor, as shown in Berk and Coletti (2024).

Next, in order to compare each particle with the turbulent flow statistics it actually experiences, we define effective flow scales sampled by the particles. We weight the vertical profiles of w_{rms}, ℓ_η, and τ_η (section 3.3.2) by the measured particle vertical distribution $\hat{w}_{\mathrm{rms}} = \langle w_{\mathrm{rms}}(z_p(t))\rangle$, $\hat{\ell}_\eta = \langle \ell_\eta(z_p(t))\rangle$, and $\hat{\tau}_\eta = \langle \tau_\eta(z_p(t))\rangle$, accounting for the particles' non-uniform distribution with depth. These are effective mean scales sampled by the particle ensembles rather than instantaneous values, and thus will serve as the basis for comparing bulk transport statistics across particle types.

From these effective flow scales, we define three non-dimensional parameters that govern the particle-turbulence interactions: the non-dimensional rise velocity $Rv = w_0/\hat{w}_{\mathrm{rms}}$ (similar to a

Rouse number), the relative particle size $Sz = d_p/\hat{\ell}_\eta$, and the Stokes number $St = \tau_p/\hat{\tau}_\eta$. Here, we defined the particle relaxation time with the measured terminal rise velocity: $\tau_p = w_0/((1-\beta)g)$. We report the range of values in table 3.3, where the uncertainty is a measure of the particle sampling spread along the water column. We find that particle buoyancy is comparable to or stronger than turbulent fluctuations ($Rv \approx 0.5$–1.9 for buoyant particles), whereas the neutral tracer has $Sv \approx 0$. Also, the particles are much larger than the Kolmogorov length ($Sz \approx 9$–22), so finite-size effects may be important for all shapes. Given the finite size, the Stokes number based on the Kolmogorov time scale $\hat{\tau}_\eta$ is not an appropriate measure of particle inertia since particles with diameter d_p are more strongly couple with eddies of comparable size (Xu and Bodenschatz, 2008). Following Xu and Bodenschatz (2008), we define a corrected Stokes number $St_c = St/Sz^{2/3}$, which replaces the Kolmogorov time scale by the eddy turnover time at the particle scale $(d_p^2/\varepsilon)^{1/3} = \hat{\tau}_\eta Sz^{2/3}$. The corrected Stokes numbers range from 0.1 to 0.6, showing that particle inertia is weak relative to the eddies at the particle scale.

3.3.4 Particle experiments

Before each run, we let the wind run for approximately 15 min to ensure that the flow reached steady state. Each run lasted 2 minutes, and we released approximately 70-90 particles per run across all particles. We released particles immediately below the water surface at $x_r \approx 5$ m upstream of the field of view. Before the particles enter the field of view to be measured, they must also have enough time to reach their vertical equilibrium state. To verify this, we compare the horizontal advective transit time $T_{adv} = x_r/\langle\hat{u}\rangle$ with the turbulent mixing time scale $T_{mix} = \ell_m^2/K_A$. Here, $\langle\hat{u}\rangle$ is the streamwise velocity. If $T_{mix} < T_{adv}$, the particles have enough time to reach an equilibrium state before being measured. Using the 16 m/s wind speed case as a conservative estimate, we have $\langle\hat{u}\rangle \approx 5$ cm/s near the surface, giving $T_{adv} \approx 100$ s. For T_{mix}, we use the particles with the largest ℓ_m^2/K_A because they are the slowest to reach equilibrium. From section 3.4, we have $T_{mix} \approx 77$ s. Thus, even the slowest particles should reach equilibrium by the time they reach the experiment field of view.

Given that our analysis and estimates of diffusivity from the particle concentration profiles rely on assumptions of horizontal homogeneity and steady state, we compare the concentration profiles upstream and downstream in the field of view and at different times in the experiment to confirm these assumptions. For the few instances where homogeneity or steady-state conditions were not met for certain particle types, the non-steady portions of the data have been omitted from the analysis. For a detailed discussion see Appendix 3.6.1.

3.4 *Results and Discussion*

In this section, we present our results for vertical diffusivity of buoyant particles using (1) a Lagrangian approach via the asymptotic estimation of diffusivity K_A obtained from the particle MSD; (2) an Eulerian approach via two estimations from the particle concentration profiles: K_C from an assumed mean profile and K_F from the mean flux profile; and (3) the estimation K_V from the eddy viscosity ν_t which also serves as a reference for estimating the Schmidt number.

3.4.1 Diffusivity measured asymptotically from particle dispersion

We first estimate the turbulent diffusivity directly from the time evolution of the particles' vertical dispersion. This Lagrangian estimate is a direct, kinematic measurement and requires no assumptions about either the particle rise velocity or the turbulent flux. This will serve as the reference diffusivity against which we test the Eulerian, concentration profile-based methods in §3.4.2.

We recall that, as discussed in §3.2.1, a nonzero ensemble-mean vertical velocity would add a ballistic contribution to the MSD and affect our ability to observe a diffusive regime. However, we verified that the particle concentration profiles are statistically steady (see Appendix 3.6.1). Consistent with this, we measure $\langle w_p \rangle \approx 0$ for all particle types and wind speeds. A vanishing mean vertical velocity does not mean that the particles are not rising relative to the fluid. In steady state, the upward buoyant drift is exactly balanced by the downward turbulent flux, such that the mean velocity of particles at any depth is zero. Thus, the Taylor method described in §3.2.1 can be applied to measure the diffusivity from the dispersion directly.

To calculate dispersion, each particle trajectory is re-referenced to its own initial time t_0 and

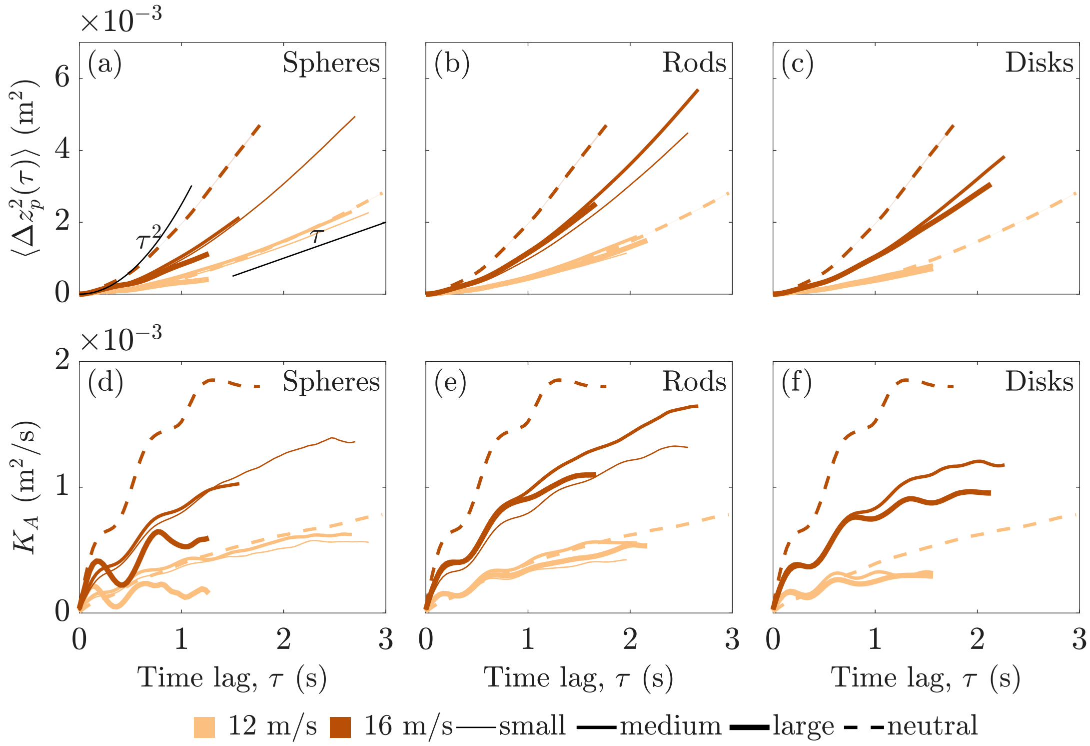

Figure 3.5: Time evolution of (a-c) particle vertical dispersion and (d-f) instantaneous diffusivity $K_A = 0.5\, d\langle \Delta z_p^2(\tau)\rangle / d\tau$ for all experiments.

depth $z_p(t_0)$, and the vertical displacement at time lag τ is defined as $\Delta z_p(\tau) = z_p(t_0 + \tau) - z_p(t_0)$. The dispersion $\langle \Delta z_p^2(\tau)\rangle$ is then obtained by ensemble averaging over all available trajectories. Because particle trajectories end when they reach the surface, longer trajectories are biased toward deeper particles. To correct this bias, we implement a weighting scheme where each trajectory's contribution is adjusted at every time lag τ such that the sampled distribution matches the stationary distribution for each experiment (Appendix 3.6.2). The result is an effective, depth-averaged dispersion, rather than a local dispersion at a specific depth.

We plot the vertical dispersion for all particles for both wind speeds in Figure 3.5a-c. In all cases we observe the dispersion following the expected ballistic to diffusive transition, where at short lags the dispersion scales as $\langle \Delta z_p^2(\tau)\rangle \propto \tau^2$, and $\langle \Delta z_p^2(\tau)\rangle \sim \tau$ at longer lags, with higher wind speeds corresponding to higher dispersion. The instantaneous diffusivity $K(\tau) = 1/2d\langle \Delta z_p^2(\tau)\rangle/d\tau$ is plotted in Figure 3.5d-f. We see the initial rise in K in the ballistic regime followed by a leveling off in the diffusive regime. There are also oscillations in the diffusivity due to the waves which are strongest at short time lags. Note, the most buoyant particles (the large spheres) have the shortest trajectories because they spend less time underwater.

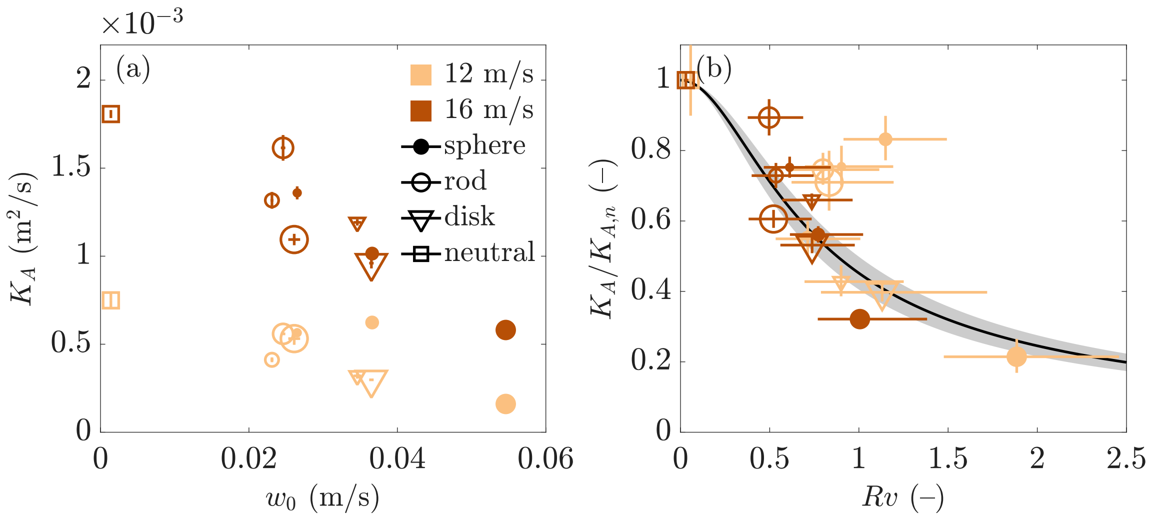

Figure 3.6: (a) Depth-averaged estimations of long-time diffusivity K_A from the asymptotic method. (b) Ratio of bulk diffusivity from the asymptotic method for each particle class to that of the nearly neutrally buoyant particles, $K_A/K_{A,n}$, versus the velocity parameter Rv. The solid line is Csanady's prediction in equation 3.14, where the shaded region represents the 95% confidence interval of the nonlinear least-squares fit to the data.

We estimate the asymptotic diffusivity K_A by averaging the diffusive plateau of $K(t)$ in Figure 3.5d-f. We plot K_A as a function of the particle quiescent rise velocity w_0 in Figure 3.6a, where we see that K_A decreases by a factor of three to four between the neutral particles and the most buoyant ones. This decrease in diffusivity shows that buoyant particles disperse slower. To compare across the different wind speeds, we normalize K_A by the neutral particle value and plot it as a function of Rv in Figure 3.6b. Here, the normalized diffusivity $K_A/K_{A,n}$ decreases with increasing buoyancy, and is well-described by the crossing-trajectories prediction of Csanady (1963) (Equation 3.14 with best-fit $C = 1.9 \pm 0.2$) and values reported in the literature varying widely across studies. This lies within the range reported for slightly buoyant particles in a jet by Aiyer and Meneveau (2022), who obtained $C = 0.85$–2. The agreement with the crossing-trajectories theory means particles with higher rise velocity will have a shorter decorrelation timescale as they move through the turbulent eddies, resulting in a reduced diffusivity. Thus, in this regime, buoyancy is the primary control on vertical particle diffusivity, with particle shape playing only a secondary role and mainly contributing through its effect on w_0.

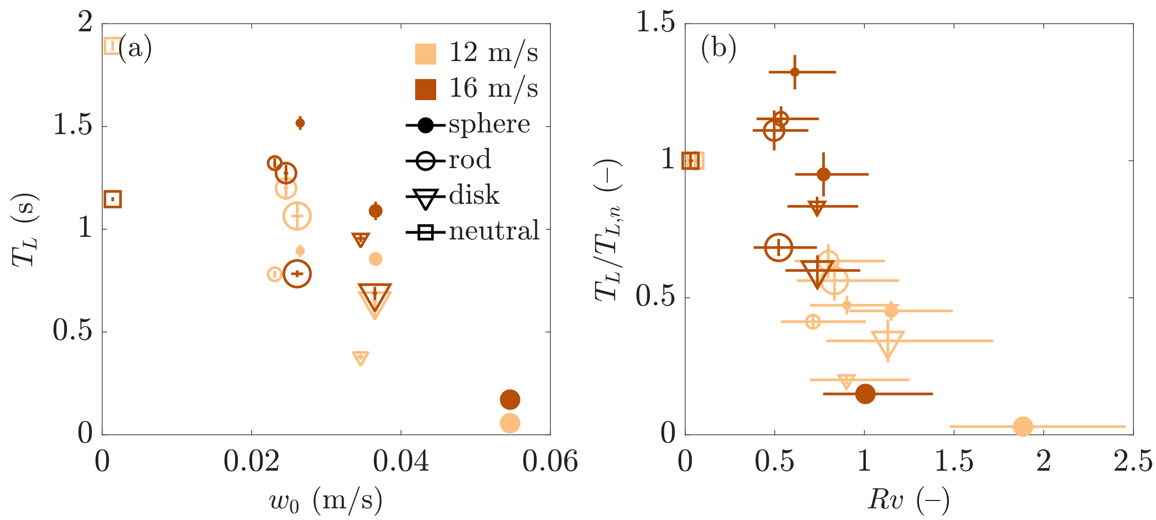

Figure 3.7: (a) Depth-averaged decorrelation time scale T_A as a function of the quiescent particle rise velocity w_0. (b) Decorrelation time scale normalized by the corresponding neutral-particle value, $T_A/T_{A,n}$, as a function of the velocity parameter Rv. Error bars denote the uncertainty of the fitted diffusivity.

To further support this hypothesis, we examine the fitted Lagrangian decorrelation time scale T_L by fitting the Taylor (1922) diffusivity solution

$$K(t) = \frac{1}{2}\frac{d\langle \Delta z_p^2(\tau)\rangle}{dt} = K_A(1 - e^{-t/T_L}),$$

to the K_A curves in figures 3.5d-f where both K_A and T_L are fitting parameters. Figure 3.7a shows a decrease in the fitted T_L with increasing particle rise velocity, confirming that the particles' velocity decorrelate more rapidly from the surrounding flow as buoyancy increases. Similar to figure

3.6b, the normalized T_L in Figure 3.7b decreases with Rv. This trend is consistent with crossing trajectories effect because increasing Rv causes particles to sample higher frequency turbulence, thus reducing their Lagrangian decorrelation time.

3.4.2 Diffusivity estimated from particle concentration profiles

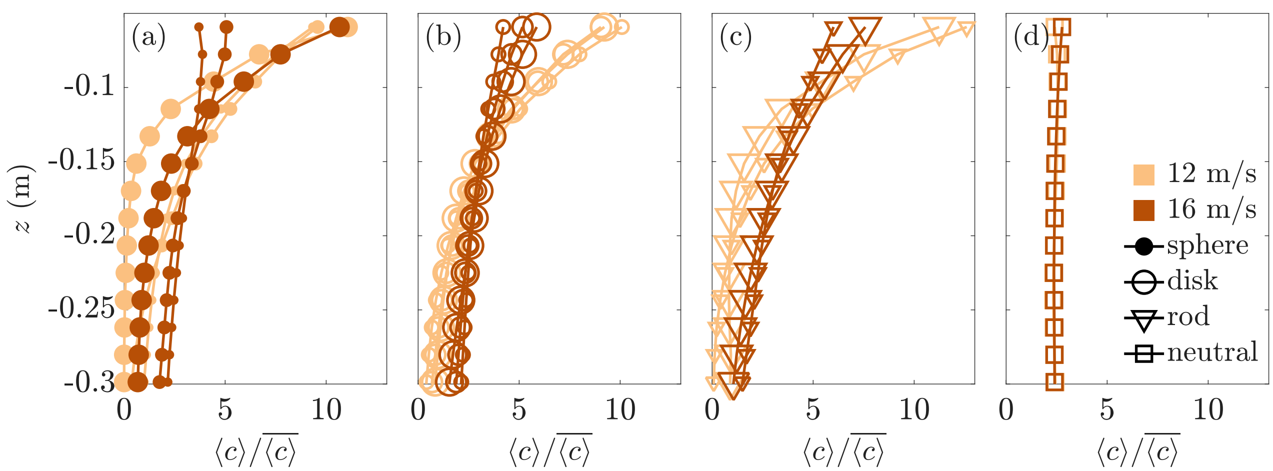

Figure 3.8: Normalized concentration profiles across different particle types and flow conditions. Each subfigure corresponds to a different particle group. Larger marker sizes indicate larger particle size.

We next evaluate the vertical diffusivity using the Eulerian concentration profiles $\langle c \rangle$ which we have plotted in Figure 3.8, normalized by the depth-integrated concentration $\overline{\langle c \rangle} = \int_{-h}^{0} \langle c \rangle \, dz$. In these analyses, we assume the average particle rise velocity to be the terminal velocity in quiescent water w_0, a common assumption in both sediment and microplastics transport. We compare these diffusivity estimates to the more direct Lagrangian estimate K_A. The neutral particles are excluded from this analysis because they are nearly uniformly mixed; i.e., $d\langle c \rangle / dz \approx 0$ which leads to large uncertainty in any diffusivity estimate.

We first plot the depth-resolved, flux-estimate diffusivity K_F as defined in (3.20) in Figure 3.9. In all cases, K_F is relatively uniform over depth, especially near the surface where most of the particles

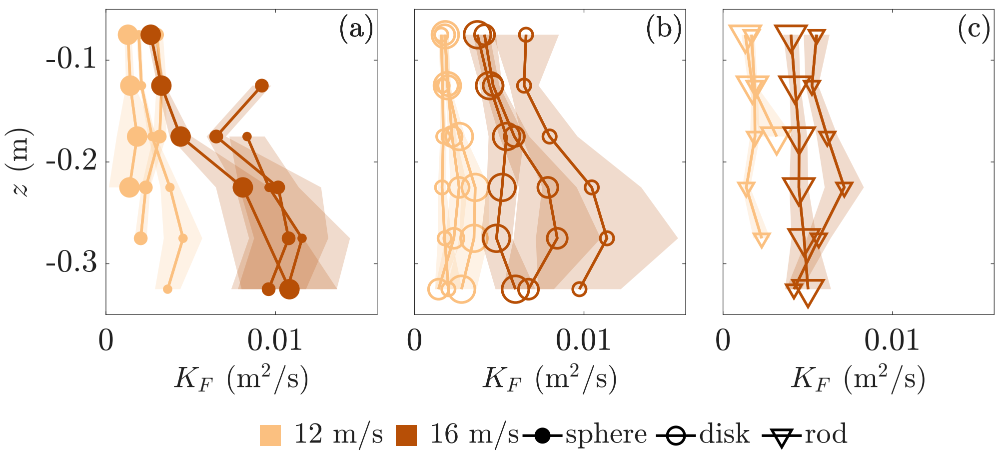

Figure 3.9: Vertical profiles of Eulerian turbulent diffusivity calculating assuming that the particle effective rise velocity is equal to the quiescent rise velocities. The 95% confidence intervals were obtained by bootstrap resampling, with uncertainty propagated through the concentration profile and gradient, and diffusivity calculations. We removed measurements with confidence intervals greater than 0.005 m^2/s.

are found. This supports the assumption that a constant diffusivity over depth is appropriate, as will be used in the following analysis.

Next, we estimate a bulk diffusivity from the concentration profiles. Figure 3.8 shows a clear exponential decay of $\langle c \rangle$ with depth for all buoyant particle types and wind speeds, agreeing with the predicted profile for a constant diffusivity as in (3.22). Fitting the profiles $\langle c \rangle(z) = c_0 \exp(z/\ell_m)$ to each concentration profile, we obtain the particle surface concentration c_0 and the mixing length ℓ_m. We plot the mixing length ℓ_m as a function of w_0 in Figure 3.10a and see that ℓ_m decreases with increasing w_0, i.e., increasingly buoyant particles are found closer to the surface. When we normalize the concentration profiles by c_0 and plot them against depth normalized by ℓ_m in Figure 3.10b, all the profiles collapse onto a single curve. This collapse supports the validity of the model and its assumption of a constant diffusivity (and drift velocity) over depth. From these fits, we find the corresponding diffusivity as $K_C = \ell_m\, w_0$ (3.24), shown in Figure 3.11a. Under the high wind speed (16 m/s), K_C decreases with increasing w_0 with some shape-dependence, e.g., falling

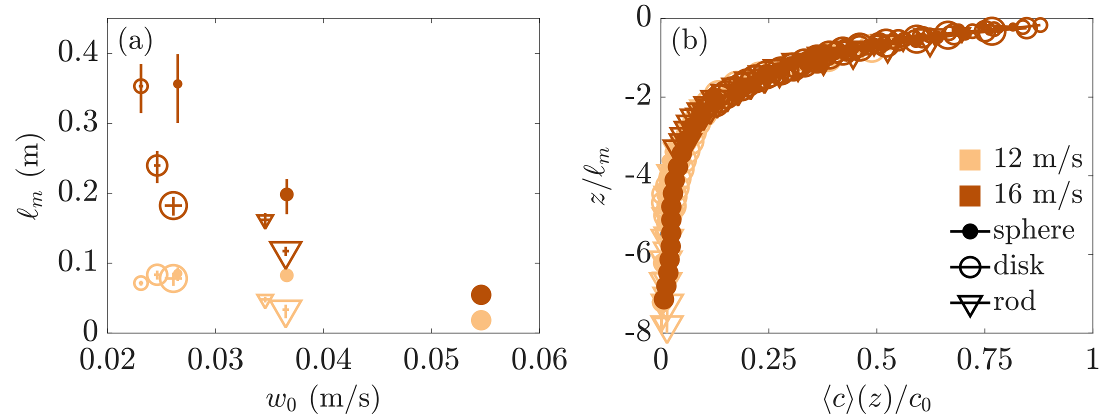

Figure 3.10: Mixing length and particle concentration profiles derived from exponential fits. (a) Mixing length ℓ_m as a function of particle rise velocity w_0 for all buoyant particle types and wind speeds. Error bars denote 95% confidence intervals from exponential-profile fits. (b) Normalized concentration profiles $\langle c\rangle(z)/c_0$ plotted against normalized depth z/ℓ_m.

most rapidly for disks. In contrast, the 12 m/s wind speed cases show K_C is relatively constant across the particle types with a slight decrease with increasing w_0.

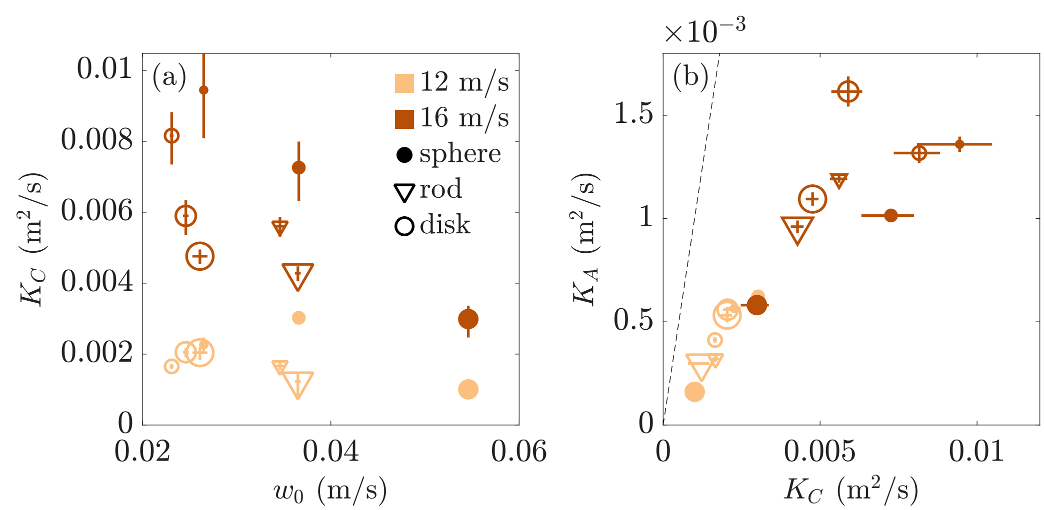

Figure 3.11: (a) Depth-averaged vertical diffusivity from exponential fitting, $K_C = \ell_m w_0$as a function of particle rise velocity. Error bars denote 95% confidence intervals. (b) Comparison of dispersion-based diffusivity vs. diffusivity from exponential fitting; the dashed line is 1:1.

We plot these Eulerian estimates of K_C against the Lagrangian estimates of K_A in Figure 3.11b, where we observe that the two estimates are strongly correlated. However, the correlation is not one-to-one; the K_C values are nearly an order of magnitude larger than the corresponding K_A values. Comparing K_F to K_A would give a similar trend, as K_F values track closely to K_C. The likely explanation for the large difference in magnitude is the assumption of w_0 as the assumed drift velocity in the derivation of K_C. Because $K_C = \ell_m w_0$ yields diffusivities that are too high, it suggests that w_0 is an overestimate of the effective particle rise velocity in our experiments. It follows that the particle's interactions with the turbulent and wavy flow reduces their average rise velocity in our experiments. We quantify the extent of this reduction in the rise velocity in the following section §3.4.3.

3.4.3 Effective rise velocity

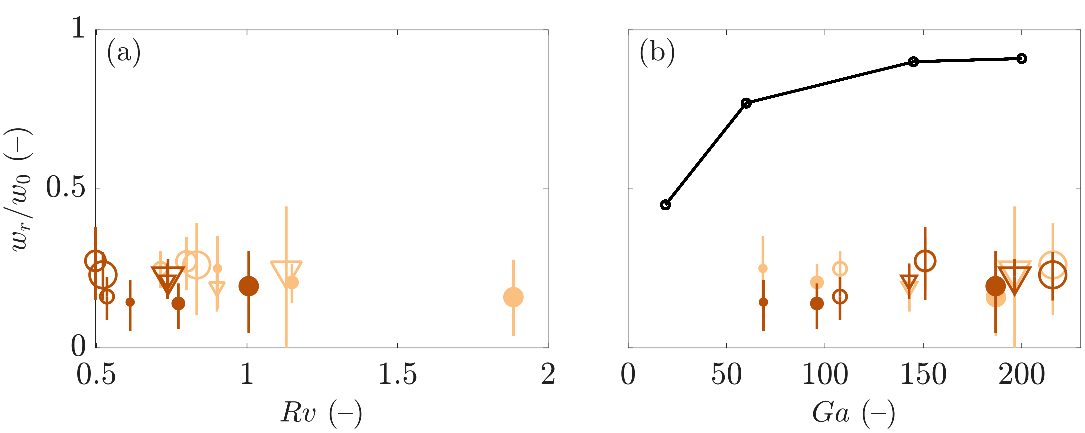

Figure 3.12: Normalized effective rise velocity w_r/w_0, where $w_r = K_A/\ell_m$, versus (a) velocity parameter Rv, and (b) Galileo number Ga where the black solid line represents the effective rise velocity of settling spheres in HIT from Fornari et al. (2016b). The error bars come from error propagation. We omitted the error bars for Rv and Ga to improve visualization (see Table 3.3 for the values with uncertainties).

Given that K_C overestimates our measurement of K_A, we conclude w_0 is not the appropriate drift velocity to use in this system. We instead estimate an effective rise velocity as $w_r = K_A/\ell_m$, i.e., the drift velocity that closes the flux balance in (3.19) given the measured diffusivity K_A. Note that w_r is not the same as the measured mean particle velocity $\langle w_p \rangle$ which vanishes in steady state (§3.4.1). Rather, w_r represents the mean drift of the particles relative to the mean Eulerian velocity.

We plot w_r normalized by w_0 as a function of Rv and Ga in Figure 3.12. We find that the effective rise velocity in each case is reduced by 60–80% relative to the quiescent value. In Figure 3.12b , we compare our results with simulations of settling spheres ($SG = 1.00035$–1.038) in homogeneous isotropic turbulence (HIT) (Fornari et al., 2016b); we justify this comparison by showing that the dynamics of slightly heavy and slightly buoyant particles are approximately symmetric (Appendix 3.6.4). The reduction we observe far exceeds that observed in HIT at similar Ga.

The excess rise velocity reduction in our experiments is likely due, in part, to particles preferentially sampling downwelling fluid. In a flow with a free surface, buoyant particles collect at surface convergence zones which coincide with regions of downwelling; the particles therefore oversample downward-moving fluid, i.e., $\langle w_f \rangle < 0$ along their trajectories. This mechanism is well-documented for buoyant material in Langmuir turbulence, where particles accumulate in downwelling regions beneath windrows (Chor et al., 2018b; Chamecki et al., 2019). This is similar to the retention of slowly rising particles in cellular flows described in the classic work of Stommel (1949). While our Langmuir number indicates wave-influenced turbulence without fully developed Langmuir circulation (§3.3.2), any free-surface turbulent flow can lead to particles clustering in convergence zones (Li et al., 2025).

Beyond preferential sampling, some of the rise velocity reduction could be due to the particle's finite size. Recent work has argued that the Basset history force and added mass can reduce sediment settling velocities for particles not small relative to the Kolmogorov lengthscale (Li et al., 2023). Our particles have average size ratios of $Sz \approx 9 - 21$, and the analysis of Li et al. (2023) predicts a reduction in terminal velocity of up to 65% for $Sz = 10$ and up to 75% for $Sz = 20$ (see their Eqn. 10). While this model was derived for spherical particles, it does indicate that a large rise velocity reduction is possible for particles that are larger than the Kolomogorv lengthscale.

Because we do not measure the fluid velocity along particle trajectories, our measurements cannot observe or distinguish these effects directly. And, regardless of how the rise velocity is reduced, the implication is the same: namely that the drift velocity needed to describe the average particle concentration profile is substantially smaller than w_0. Conversely, assuming w_0 would lead to an overestimated diffusivity from the concentration profiles alone.

3.4.4 Eddy viscosity and Schmidt number

We also compare the particle diffusivity K_A to the flow's eddy viscosity ν_t, quantifying the degree to which buoyancy decouples particle transport from momentum transport. Form the eddy viscosity profile in Figure 3.4d, we calculated an effective, average eddy viscosity $\hat{\nu}_t$ weighted by the concentration profile for each particle under each wind speed. We plot $\hat{\nu}_t$ in Figure 3.13a as a function of Rv, where we can also naively assume $Sc_t \approx 1$, and thus $\nu_t \approx K_V$. We see that K_V increases as particle buoyancy increases, since the more buoyant particles spend increasingly more time close to the surface where $\hat{\nu}_t$ is slightly higher. Although there is only a modest change with Rv, this is still the opposite of the trend observed for diffusivity with Rv from the previous estimates.

When we compare the particle and momentum diffusivity as $Sc_t^{-1} = K_A/\nu_t$ in Figure 3.13b, we see that Sc_t^{-1} decreases as particle buoyancy increases, again consistent with the crossing-trajectories theory of Csanady (1963) (solid curve from equation 3.14 with best-fit $C = 2.5 \pm 0.5$). Consequently, Sc_t increases monotonically with Rv (figure 3.13c), reaching values up to 3.3 for the most buoyant particles. These results show buoyant particles with $Sc_t > 1$, i.e., that their diffusivity is significantly less than that of the fluid momentum aligning with Chauchat et al. (2022), who reported Sc_t between 3 and 4 for settling particles in open-channel flows. In contrast, the neutral particles exhibit $Sc_t \approx 1$, indicating that the neutral particles show no effect of crossing-trajectories. In addition, this result shows strong agreement between the two independent measures of tracer diffusivity: namely the eddy viscosity from the turbulent Reynolds stress and the estimate from the neutral particle dispersion. Thus, this can lend confidence to the eddy viscosity values estimated in this flow. Together, these results indicate that common modeling assumptions (e.g., a quiescent rise velocity and $Sc_t = 1$) will fail with increasing Rv for buoyant particles in this system.

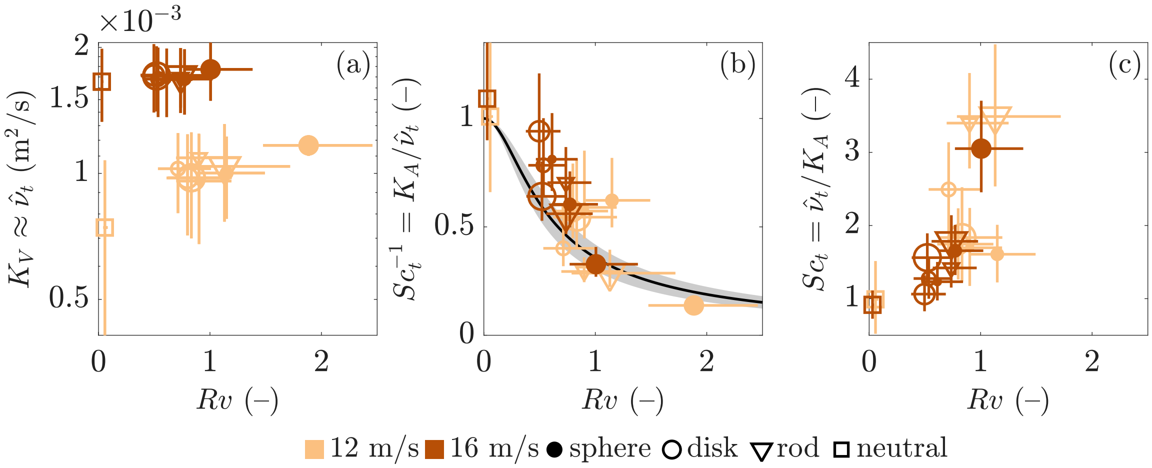

Figure 3.13: (a) Depth-averaged particle turbulent diffusivity assuming $Sc_t \approx 1$ and thus $K_V \approx \nu_t$. (b) Inverse turbulent Schmidt number Sc_t^{-1} versus Rv for all particle types and both wind speeds. The solid curve is the Csanady (1963) crossing-trajectories theory fitting with $C = 1.4$. (c) Turbulent Schmidt number Sc_t plotted against Rv.

3.5 *Conclusions*

This study characterizes the vertical transport of near-neutrally buoyant, finite-sized particles in a wind-driven free-surface boundary layer, using both Lagrangian and Eulerian approaches to evaluate the vertical turbulent diffusivity K. The Lagrangian approach estimates diffusivity K_A directly from the particle dispersion, which follows the classic ballistic-to-diffusive transition, with waves introducing some periodic motion. A main result is that particle buoyancy is the primary control on the vertical diffusivity: K_A decreases by a factor of up to four between the least buoyant particles and the most buoyant ones. This reduction in diffusivity with increasing rise velocity is found to be well explained by the crossing-trajectories theory of Csanady (1963) across all particles shapes and sizes. This effect is further confirmed by the decrease of the Lagrangian decorrelation time scale T_L with Rv which we estimated by fitting to the particle dispersion over time. We also find that particle shape plays only a secondary role, entering primarily through its effect on the quiescent rise velocity w_0. Inertial effects are also found to be weak, as is expected for near-neutrally buoyant particles (Berk and Coletti, 2024).

We then show that the Eulerian approach to inferring K_C from concentration profiles overestimates the diffusivity when assuming a quiescent rise velocity w_0. When comparing to the Lagrangian estimate K_A, we find that K_C overestimates the diffusivity by nearly an order of magnitude. This suggests that the effective rise velocity is reduced 60–80% lower than w_0. This reduction exceeds that of settling spheres in homogeneous isotropic turbulence at similar Galileo numbers (Fornari et al., 2016b), and we hypothesize that part of the excess reduction comes from preferential sampling of downwelling fluid. In flows with a free surface, buoyant particles can easily collect in surface convergence zones above downwelling regions (Yang et al., 2014; Kukulka and Brunner, 2015; Chamecki et al., 2019). Another explanation for the rise velocity reduction could be the particles' finite-size and associated unsteady forces (Li et al., 2023). To fully explain the reduced rise velocity, experiments with co-located fluid and particle velocities would be needed.

Finally, even though we find $Sc_t \approx 1$ for the neutrally buoyant particles, we find that $Sc_t \neq 1$ for the buoyant particles. Specifically, we find that Sc_t increases monotonically with Rv, reaching values up to 3.5 for the most buoyant particles, values which agree with recent measurements of settling particles in open-channel flows (Chauchat et al., 2022). Thus, this further emphasizes that $Sc_t \approx 1$ is not an appropriate closure for this regime of buoyant particles.

Together, these findings show how standard closures can result in errors in predicting diffusivity. Assuming $Sc_t = 1$ and a quiescent rise velocity can both result in overestimated particle diffusivity. Moreover, we demonstrate the crossing-trajectories effect clearly in a wavy wind-drive boundary layer flow with non-spherical and finite-sized particles. These results indicate that transport parameterizations for buoyant particles near the ocean surface must account for the reduction of diffusivity and rise velocity, and the buoyancy-dependent Schmidt number to accurately represent particle vertical distribution and transport.

3.6 *Appendix*

3.6.1 Assessment of steadiness and streamwise homogeneity in our experiments

We first check whether the particle distribution changes with horizontal position. For each particle case, we bin particle positions in the horizontal (15 cm bins) and vertical (3 cm bins) directions, and normalize each horizontal slice by its total particle count. We plot the resulting distributions in figure 3.14 which shows the buoyant particle concentrations are highest near the free surface and decrease with depth while the neutral particles are more evenly distributed throughout the water column, as expected. Most particles, including the neutral particles, show strong homogeneity in the *x* direction.

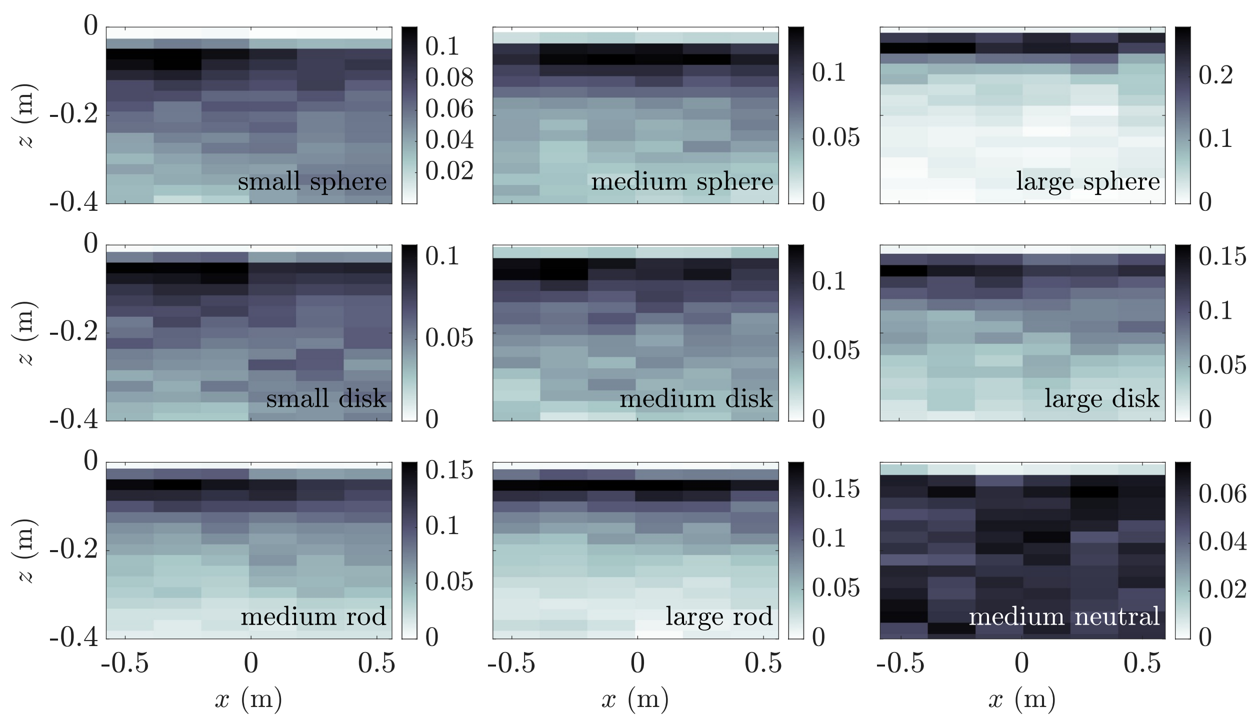

Figure 3.14: Horizontal-vertical distribution of particle counts (PDF) for various particle types under 16 m/s wind forcing. Each panel displays the probability density of particle counts in the x–z plane, with darker colors indicating higher concentrations.

We then check whether the particles have reached a statistically steady state in figure 3.15.

Each total run time was divided into quartiles, and the mean concentration profile for each particle shape, size, and wind speed was computed independently for each quartile. The convergence of these four quartile profiles shows that the particle distribution has reached a steady state. Temporal convergence generally improved with sphere size, though small spheres exhibited persistent transients at 12 m/s. Disks and medium rods converged consistently well. Large rods were unsteady at 12 m/s, showing pronounced deep penetration, but stabilized at 16 m/s. Neutral particles remained stationary and evenly mixed at both wind speeds. Unsteady quartiles were not considered in our analysis.

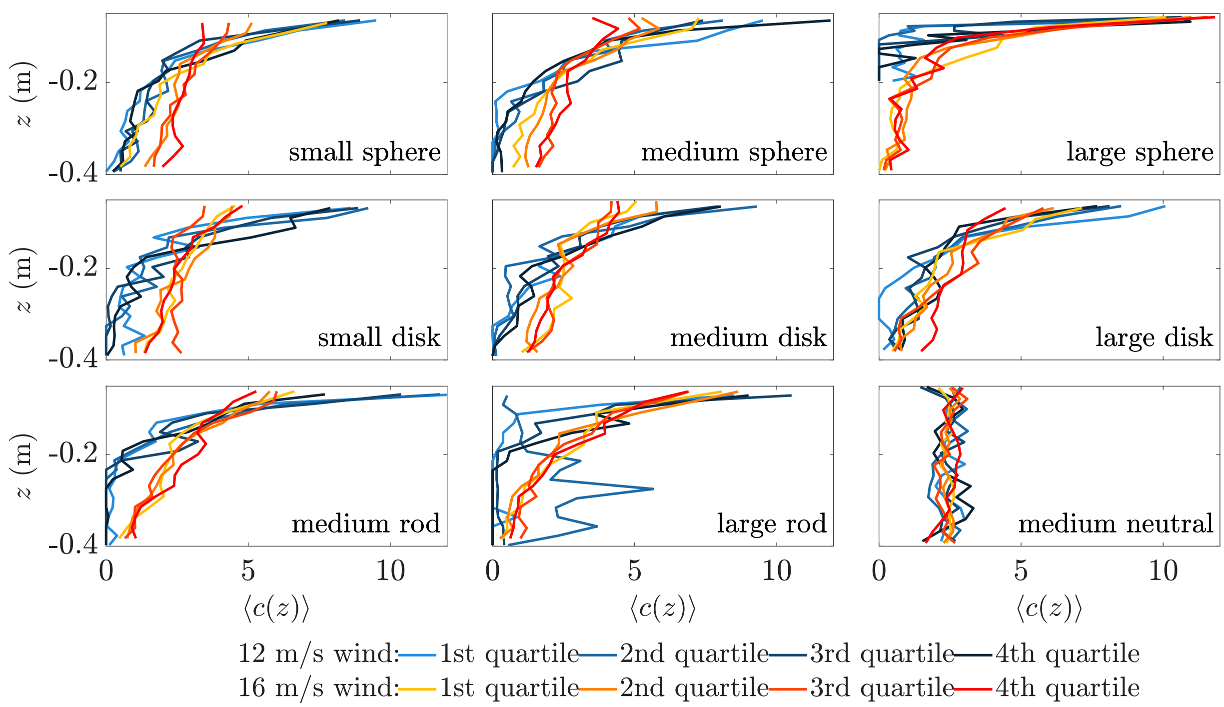

Figure 3.15: Temporal evolution of vertical concentration profiles $\langle c \rangle$ for various particle types under 12 m/s (blue shades) and 16 m/s (red shades) wind speeds.

3.6.2 Trajectory bias correction for asymptotic diffusivity estimate

The raw MSD is biased at large lag because short trajectories do not contribute uniformly across depth. We correct for this by reweighting trajectory segments to match the stationary depth distribution.

We discretize the vertical domain into fine reference bins $b = 1, \dots, B$ with edges $[z_b, z_{b+1}]$ and width $\Delta b = z_{b+1} - z_b$. From all recorded particle positions, we estimate the stationary depth distribution $c(b)$ satisfying $\sum_{b=1}^{B} c(b)\, \Delta b = 1$. Then, for a given lag τ, define the set of all valid start indices s_0 as $\mathcal{S}_{\mathcal{P}}(\tau) = \{s_0 : s_0 + \tau \leq T_{\mathcal{P}}\}$. The count of valid starts falling in reference bin b is

$$C(\tau, b) = \sum_{\mathcal{P}} \left| \left\{ s_0 \in \mathcal{S}_{\mathcal{P}}(\tau) : z_p^{(\mathcal{P})}(s_0) \in b \right\} \right|. \tag{3.28}$$

with total $N(\tau) = \sum_{b=1}^{B} C(\tau, b)$ and empirical distribution $c_\tau(\tau, b) = C(\tau, b) \,/\, [N(\tau)\, \Delta b]$. Thus, we define the depth-bias weight as

$$W(\tau, b) = \frac{c(b)}{c_\tau(\tau, b)}, \tag{3.29}$$

which up-weights underrepresented starting depths s_0 and down-weights overrepresented ones. If we denote the squared displacement associated with s_0 as

$$\langle \Delta z_p^2 \rangle_{\text{raw}}(\tau, b) = \frac{1}{C(\tau, b)} \sum_{\mathcal{P}} \sum_{s_0 \in \mathcal{S}_{\mathcal{P}, b}(\tau)} \left[z_p^{(\mathcal{P})}(s_0 + \tau) - z_p^{(\mathcal{P})}(s_0) \right]^2, \tag{3.30}$$

then the corrected MSD is

$$\langle \Delta z_p^2 \rangle_{\text{corr}}(\tau) = \frac{\sum_{b=1}^{B} W(\tau, b)\, C(\tau, b)\, \langle \Delta z^2 \rangle_{\text{raw}}(\tau, b)}{\sum_{b=1}^{B} W(\tau, b)\, C(\tau, b)}. \tag{3.31}$$

This yields a single depth-averaged MSD at each lag. The correction uses the full stationary distribution $c(b)$ across all fine bins, so the resulting diffusivity K_A is a bulk quantity representative of the entire water column, not a depth-resolved estimate. When $C(\tau, b) = 0$ for bins where $c(b)$ is appreciable, the lag is too large for reliable sampling and is excluded.

3.6.3 Equivalence between diffusivity in conservation equation and MSD

For a point-source release, the mean concentration $\langle c \rangle$ is proportional to the position PDF of an ensemble of particles, and its evolution is described by (3.17). At $t = 0$, the particles are concentrated at the coordinate origin, so we have $c(z, 0) = c_0 \delta(z)$, with c_0 the initial integrated concentration and $\delta(z)$ the Dirac delta function. The first and second moments of z_p follow by multiplying (3.17) by z and z^2 and integrating over z after dividing out c_0. For the mean, we have

$$\frac{\mathrm{d}}{\mathrm{d}t}\langle z_p(t)\rangle = \int z\,\frac{\partial\langle c\rangle}{\partial t}\,\mathrm{d}z = w_r, \tag{3.32}$$

so $\langle z_p(t)\rangle = w_r t$, as before. In the same manner, the second moment of (3.17) is

$$\int z^2\left[\frac{\partial\langle c\rangle}{\partial t} + \frac{\partial}{\partial z}\big(w_r\langle c\rangle\big)\right]\mathrm{d}z = \int z^2\left[\frac{\partial}{\partial z}\left(K(t)\,\frac{\partial\langle c\rangle}{\partial z}\right)\right]\mathrm{d}z, \tag{3.33}$$

assuming $\langle c\rangle$ and its derivatives vanish at the boundaries, giving

$$\frac{\mathrm{d}}{\mathrm{d}t}\langle z_p^2(t)\rangle - 2w_r\langle z_p(t)\rangle = 2K(t). \tag{3.34}$$

With $\langle z_p(t)\rangle = w_r t$, we obtain

$$\frac{1}{2}\frac{\mathrm{d}}{\mathrm{d}t}\langle z_p^2(t)\rangle - w_r^2 t = K(t). \tag{3.35}$$

Thus, the Eulerian conservation equation for concentration and the Lagrangian MSD (see equation 3.10) are two representations of the same transport process.

3.6.4 Mapping between slightly buoyant and slightly settling particles

Under a simplified Maxey–Riley equation, particles with small positive (settling) and negative (rising) density differences exhibit leading-order symmetric behavior, primarily differing by a reversal of the effective gravitational forcing direction. Given that the Maxey-Riley equation is valid for small, low-Re_p spheres and our particles are neither, we only use this equation to reason about scalings and symmetry, not to model the dynamics quantitatively.

For a rigid sphere in a non-uniform flow, the Maxey–Riley equation (Maxey and Riley, 1983) including Stokes drag, fluid acceleration, added mass, and gravitational/buoyancy forcing can be written as

$$\frac{\mathrm{d}\mathbf{u}_p}{\mathrm{d}t} = \beta\frac{\mathrm{D}\mathbf{u}_f}{\mathrm{D}t} + (1-\beta)\mathbf{g} - \gamma(\mathbf{u}_p - \mathbf{u}_f), \tag{3.36}$$

where $\mathbf{u}_p(t)$ is the particle velocity and $\mathbf{u}_f(\mathbf{x}_p, t)$ the fluid velocity at the particle centroid $\mathbf{x}_p$. The material derivative of the fluid velocity $\mathrm{D}\mathbf{u}_f/\mathrm{D}t$ accounts for local unsteadiness and convective fluid acceleration. The gravitational acceleration vector is $\mathbf{g}$ and the coordinate system in z is positive upward. The particle response rate γ, density parameter β, and gravitational forcing $\mathbf{g}_f$ are defined as

$$\beta = \frac{3}{2\left(\frac{\rho_p}{\rho_f} + \frac{1}{2}\right)}, \quad \mathbf{g}_f = (1-\beta)\mathbf{g} = \mathbf{g}\frac{\frac{\rho_p}{\rho_f} - 1}{\frac{\rho_p}{\rho_f} + \frac{1}{2}}, \quad \gamma = \frac{3\nu\,\mathcal{D}(Re_p)}{4d_p^2\left(\frac{\rho_p}{\rho_f} + \frac{1}{2}\right)}, \tag{3.37a, b, c}$$

Here, $\tau_p = \gamma^{-1}$ is an effective particle response time and quantifies its inertial response to fluid motion. In the Stokes limit, $\mathcal{D}(Re_p) = 24$ and τ_p reduces to the usual Stokes relaxation time. For finite particle Reynolds number, one common parameterization for the nonlinear drag is the Schiller-Naumann function $\mathcal{D}(Re_p) \equiv C_D Re_p = 24\left(1 + 0.15 Re_p^{0.687}\right)$. The vector $\mathbf{g}_f$ is the effective gravitational or buoyancy acceleration.

To examine the near-neutral limit, we write the density ratio as

$$\frac{\rho_p}{\rho_f} = 1 + \epsilon, \tag{3.38}$$

with $\epsilon = \Delta\rho_p/\rho_f$ measuring the relative density difference. For a slightly heavy particle, $\epsilon > 0$ and for a slightly buoyant one, $\epsilon < 0$. Because we are primarily interested in evaluating how particle inertia and buoyancy respond to small density contrasts, we perform asymptotic expansions on the particle response rate γ and the gravitational forcing $\mathbf{g}_f$. Note that β and γ have the same density-ratio dependence.

Substituting (3.38) into γ and $\mathbf{g}_f$ (3.37), and expanding in powers of ϵ gives

$$\gamma(\epsilon, Re_p) = \frac{12\nu\mathcal{D}(Re_p)}{d_p^2}\left(1 - \frac{2}{3}\epsilon + O(\epsilon^2)\right), \text{ and } \mathbf{g}_f(\epsilon) = \frac{2}{3}\mathbf{g}\epsilon\left(1 - \frac{2}{3}\epsilon + O(\epsilon^2)\right). \tag{3.39a, b}$$

Thus, for fixed Re_p, the response rate varies approximately linearly with ϵ, while its dependence on particle Reynolds number is prescribed through the nonlinear drag function $\mathcal{D}(Re_p)$. The effective gravitational forcing varies smoothly and approximately linearly with ϵ. In this asymptotic analysis, Re_p is held fixed, corresponding to a directly measured particle-fluid relative velocity. The factor $\mathcal{D}(Re_p)$ is therefore treated as constant with respect to ϵ. We therefore remove the Re_p dependence in the subsequent notation.

Now, consider two particles with the same diameter d_p and small density contrast $|\epsilon_1| \ll 1$, one slightly heavier than the fluid ($\epsilon = +\epsilon_1$) and one slightly lighter ($\epsilon = -\epsilon_1$). From (3.39), the difference magnitude is for the particle response rate and buoyancy term are

$$\gamma(+\epsilon_1)-\gamma(-\epsilon_1) = -\frac{16\nu\mathcal{D}(Re_p)}{d_p^2}\epsilon_1+O(\epsilon_1^2), \text{ and } |\mathbf{g}_f(+\epsilon_1)|-|\mathbf{g}_f(-\epsilon_1)| = \frac{8}{9}g\epsilon_1^2-O(\epsilon_1^3), \quad (3.40a,b)$$

respectively. Thus, slightly heavy and slightly buoyant particles with the same diameter experience inertial and gravity/buoyancy forcing of equal magnitude and opposite sign and have almost identical response rates to first order and second order in ϵ_1, respectively.

Their dynamics differ primarily by a reversal of the vertical direction. Mathematically, if we reflect the vertical variables

$$z \mapsto -z, \quad w_p \mapsto -w_p, \quad w_f \mapsto -w_f, \quad \mathbf{g} \mapsto -\mathbf{g},$$

then, to leading order in $|\epsilon_1|$, the equation of motion 3.36 for a slightly buoyant particle is mapped into that of a slightly sinking particle with the same $|\epsilon_1|$. This justifies using results from the extensive literature on settling particle to interpret the behavior of nearly neutrally buoyant particles, provided $|\rho_p/\rho_f - 1| \ll 1$. For our particles, $|\rho_p/\rho_f - 1| \leq 0.04$, so the higher-order terms in γ and $\mathbf{g}_f$ are at most $O(10^{-3})$ and $O(10^{-5})$, respectively. The near-neutral expansion is therefore accurate to better than 1%.

To summarize, the vertical reflection of the dynamics represents a leading-order symmetry of the reduced particle equation when particles have the same diameter, equal density contrast relative to the fluid, and same particle Reynolds number. However, this symmetry is approximate since mean shear, free-surface boundary condition, and wave-turbulence dynamics can all distinguish rising from settling particles in wall-bounded or homogeneous flows. The comparison nevertheless provides a useful scaling argument for interpreting and comparing settling and rising near-neutrally buoyant particles results from the literature, provided that the small-density-contrast assumption is satisfied.

Chapter 4

WAVE AND TURBULENCE EFFECTS ON LAGRANGIAN STATISTICS OF FINITE-SIZED PARTICLES

This chapter is based on a manuscript in preparation: Chávez-Dorado, J., Baker, L., Riley, J., & DiBenedetto, M., "Wave and Turbulence Effects on Lagrangian Statistics of Finite-sized particles in Free-surface Boundary Layer," 2026.

4.1 *Introduction*

Understanding the transport of buoyant particles in free-surface boundary layers is important for many environmental and engineering problems ranging from the fate of buoyant microplastics and oil droplets in the upper ocean (DiBenedetto, 2026; Boufadel et al., 2020) to the transport of pollutants and nutrients in the atmosphere (Farazmand, 2024). These environments are characterized by unsteady flows containing waves and turbulence across a range of spatial and temporal scales (Thais and Magnaudet, 1996; Teixeira and Belcher, 2002), together with particle properties that can strongly modify the particle response (see reviews by Brandt and Coletti, 2022; Mathai et al., 2020). Specifically, vertical transport determines how long particles remain near the free surface, how deeply they penetrate into the water column, and how they are redistributed by the flow. As a result, waves, turbulence, and particle-flow interactions can alter the vertical distribution and mixing of buoyant particles (DiBenedetto, 2026).

Vertical particle transport in an unsteady free-surface boundary layer is partly driven by the spreading of an ensemble of particles. This dispersion (mixing) is a inherently Lagrangian phenomenon since Lagrangian measurements provide a direct description of particle motion by following individual trajectories through the flow (Toschi and Bodenschatz, 2009). These measurements characterize the particle displacement and velocity history of the particle motion and the interaction between particles and the flow.

At long times, particle mixing is parameterized by an effective turbulent vertical diffusivity. This diffusivity can be estimated from the growth rate of the particle mean-squared displacement (MSD), denoted by K_A, or equivalently, from the time integral of the Lagrangian velocity autocovariance, denoted by K (Taylor, 1922). In practice, the autocovariance approach is often preferred because Lagrangian trajectories are rarely long enough to resolve a clean diffusive regime needed for the MSD, whereas the autocorrelation (normalized autocovariance) can be modeled from approximations to obtain its long time behavior even with finite data (Pope, 2000). The autocovariance contains information about both the variance of the velocity fluctuations and the timescale over which those fluctuations remain correlated. Therefore, the diffusivity can be expressed in terms of the velocity variance and the Lagrangian integral timescale.

In wall-bounded turbulence, anisotropy dominates and the autocorrelation depends on wall-normal position (Baker and Coletti, 2021, 2022). In free-surface boundary layers, however, waves and turbulence also generate velocity fluctuations with finite temporal and spatial coherence, both of which appear in the autocorrelation function (for example, see Veneziani et al., 2004; LaCasce, 2008; Chávez-Dorado et al., 2025). The surface constraint suppresses part of the three-dimensional dynamics, and the presence of waves produces persistent correlations due to orbital motions with its own decorrelation scale (Reijnders et al., 2022; Eeltink et al., 2023; Chávez-Dorado et al., 2025). Consistent with this behavior, heuristic models have been proposed for the autocorrelation of narrowband waves (Garraffo et al., 2001; Sallée et al., 2008; Reijnders et al., 2022).

Thus, separating wave and turbulence contributions to diffusivity is important because they have different effects on particle transport and should not necessarily be represented by the same diffusivity parameterization. For example, waves alone contribute coherent large-scale motion (D'Asaro, 2014) but can also increase the horizontal dispersion of particles (Farazmand and Sapsis, 2019; Clark et al., 2023), whereas turbulence produces energetic mixing and dispersion at smaller scales (Snyder and Lumley, 1971). Non-breaking waves can also affect mixing by compressing and stretching the vertical distribution of buoyant particles, pushing them relatively deeper under crests as compared to troughs (DiBenedetto et al., 2022). Non-breaking and breaking waves can also add turbulence and enhance near-surface mixing through convergence zones and downward jets (Qiao et al., 2004; Babanin and Haus, 2009; Perlin et al., 2013).

Most existing approaches for separating wave and turbulence contributions have been developed using Eulerian measurements (see literature review in Chávez-Dorado et al., 2025). An analogous decomposition for Lagrangian particle statistics has received less attention. In general, the main difficulty in separating wave and turbulence contributions comes from the overlap in the frequency ranges occupied by both, together with the fact that both may appear as broadband, time-correlated signals. Furthermore, in Lagrangian measurements, particles sample velocity along moving trajectories rather than at fixed points. As they move through different wave phases and depths, the amplitude and phase of the measured wave signal can change, reducing e.g., the velocity autocorrelation relative to a fixed observer (Xuan et al., 2020). For this reason, separating the respective contributions of turbulence and waves to Lagrangian observations is not trivial, and it remains unclear how much of the net diffusive transport in a free-surface boundary layer comes from turbulence versus wave motions, or how this partition depends on particle properties.

The diffusivity depends not only on the background flow, but also on particle properties (Brandt and Coletti, 2022). For near-neutrally buoyant particles, particle buoyancy (accounted for here by the particle terminal rise velocity in still-water w_0) introduces an additional source of variability but particle shape and finite-size effects play only a minor role, as seen in chapter 3. In particular, a particle with a net rise velocity crosses turbulent structures more rapidly than a fluid tracer (Yudine, 1959; Csanady, 1963; Squires and Eaton, 1991). This crossing-trajectories effect shortens the Lagrangian correlation time and can reduce the particle diffusivity as:

$$\frac{K}{K_n} = (1 + C^2 Rv^2)^{-1/2} \tag{4.1}$$

where K_n is the diffusivity of the tracer baseline, and C is a constant that relates the fluid Lagrangian decorrelation time to the average time it takes a for a buoyant/settling particle to cross an eddy. The velocity parameter $Rv = w_0/w_{\mathrm{rms}}$ quantifies the relative strength of the particle buoyancy compared to the fluid vertical velocity fluctuation root-mean-square w_{rms}. While the crossing-trajectories effect is well-studied within a turbulence context, it is unclear whether the crossing-trajectories effect also is important to how a particle interacts with a wave field.

In this study, we use trajectories of finite-size, near-neutrally buoyant particles in a free-surface boundary layer to calculate particle turbulent diffusivity K and K_A from measured Lagrangian velocity autocorrelation function and MSD, respectively. We further use a parametric model for the measured Lagrangian autocorrelation to separate the wave and turbulent components, allowing us to estimate their respective contributions to the velocity variance, integral timescale, and vertical diffusivity. We then compare the resulting diffusivities with estimates obtained from the MSD. We show that this simple model is able to reproduce the measured particle autocorrelations. From the model fits, we find that the wave component dominates the near-surface velocity variance, but contributes relatively little to the integral time scale. This results in turbulence being the main contributor to the diffusivity, with relatively little net effect of the waves. We also find that K and K_A yield similar diffusivity values and that both measures of diffusivity decrease with increasing particle rise velocity, consistent with a crossing-trajectories effect. The remainder of the paper is structured as follows: Section 4.2 introduces our stochastic model for the vertical autocorrelation. Section 4.3 describes the particle trajectories and the estimators of the Lagrangian statistics derived from them. Section 4.4 presents the results, and Section 4.5 concludes the paper.

4.2 *Theoretical framework*

4.2.1 Lagrangian description of diffusivity

We consider the vertical dispersion of an ensemble of particles: given the particle displacement $\Delta z_p = z_p(t) - z_p(t_0)$, we quantify dispersion with the mean-square displacement (MSD) of their trajectories $\langle \Delta z_p^2(t) \rangle$. Here $z_p(t)$ and $z_p(t_0)$ are the particle vertical position at time t and trajectory time origin t_0, respectively. Under statistically stationary conditions with no mean vertical particle motion, the MSD is related to the autocovariance of the vertical velocity fluctuation w_p via the following relationship:

$$\langle \Delta z_p^2(t) \rangle = 2 \int_0^t (t - \tau) R(\tau) \, d\tau, \tag{4.2}$$

where the Lagrangian autocovariance is

$$R(\tau) = \langle w_p(t_0)\, w_p(t_0 + \tau)\rangle. \tag{4.3}$$

We additionally define the vertical velocity variance $\sigma^2 = R(0)$, autocorrelation $\rho_{ww}(\tau) = R(\tau)/\sigma^2$ and the Lagrangian integral time scale $T_L = \int_0^\infty \rho_{ww}(\tau)\, d\tau$. From these relations, the diffusivity is defined as half the time rate of change of the MSD. The diffusivity should approach a constant value in the diffusive limit ($t \gg T_L$):

$$K_A = \lim_{t\to\infty} \frac{1}{2}\frac{d}{dt}\langle \Delta z_p^2(t)\rangle. \tag{4.4}$$

This we refer to as the asymptotic approximation of the diffusivity K_A. Using the expressions above, we can also similarly express the diffusivity in terms of the integral time scale and velocity fluctuation variance as

$$K = \sigma^2 T_L. \tag{4.5}$$

This follows the theory of Taylor (1922) which applies to tracers in isotropic turbulence. Thus, these relationships can potentially break down for non-tracer particles and/or particles in inhomogeneous flows. Our goal in this study is to separately estimate both K_A and K and compare the two estimates.

4.2.2 Wave and turbulence decomposition

In our experiments, the particle transport is affected by both turbulence and waves. While the diffusivity estimate K_A from the particle trajectories does not necessarily need any special treatment, estimating K requires considering the turbulence and waves separately.

We decompose the particle's vertical velocity into individual components representing the turbulence and the wave fluctuations and ignore shape, finite-size, and buoyancy effects:

$$w_p = w_p' + \tilde{w}_p \tag{4.6}$$

where w_p' is the turbulent fluctuation and $\tilde{w}_p$ is the wave fluctuation. We assume minimal wave turbulence interactions such that there is no covariance between the two components, e.g. $\langle w_p' \tilde{w}_p\rangle = 0$.

First, with respect to the turbulent component, we assume the autocovariance can be expressed as the product of the turbulent velocity variance σ_t^2 and an exponential decay

$$R_t(\tau) = \langle w'_p(t)\, w'_p(t+\tau) \rangle = \sigma_t^2 e^{-|\tau|/\Phi_t}. \tag{4.7}$$

Here, Φ_t is the decorrelation timescale associated with the turbulent velocities. This form of the autocovariance can be derived following a model of the turbulent particle velocity as an Ornstein-Uhlenbeck process with a Langevin equation which accounts for both time-correlated motion and stochastic noise (e.g., see Pope (2000)).

For the wave component of the autocovariance, we use a model of a damped oscillation (as in Garraffo et al. (2001); Sallée et al. (2008); Reijnders et al. (2022)), which captures both the wave oscillations and the decorrelation over time of the signal:

$$R_w(\tau) = \langle \tilde{w}_p(t)\tilde{w}_p(t+\tau) \rangle = \sigma_w^2 e^{-|\tau|/\Phi_w} \cos(\omega_L \tau), \tag{4.8}$$

where σ_w^2 is the wave-only variance, Φ_w is the wave decorrelation timescale and ω_L is the dominant angular frequency. This model is a common assumption in the literature typically presented without a formal derivation, however it can be derived by assuming a model of phase diffusion in a wave signal.

There are multiple physical processes that can lead to phase diffusion in the wave signal as seen by the particle which contribute to Φ_w. The first is due to the turbulent diffusion causing the particle to drift in the wave field. Another is the phase diffusion of the wave field itself. And finally, the buoyant particles rising through the wave field can also cause decorrelation similar to the crossing-trajectories effect in turbulence.

For example, consider the vertical velocity in deep-water wave described by linear wave theory for a wave with angular frequency ω_0:

$$w_w(x, z, t) = a\omega_0 e^{k_0 z} \sin(k_0 x - \omega_0 t + \phi) \tag{4.9}$$

where a is the wave amplitude, k_0 is the wavelength, and ϕ is a phase lag. If we assume motion due to the waves is small and that particle position x spreads via a diffusive process with diffusivity K, then we can derive the autocovariance R_w to relate $\Phi_w = 1/k_0^2 K$, in other words, Φ_w is related to the time it takes a particle to diffuse over a wavelength. We can also relate Φ_w to phase diffusion due to the wave field itself. In a narrowbanded wave-field with phase diffusion due to the finite bandwidth of the wave signal, the decorrelation time should scale with the width of the spectral peak $\Delta\omega$.

4.2.3 Diffusivity in a wavy-turbulent flow

With these two autocovariance models, again assuming no interaction between the waves and turbulence, the model for the total vertical velocity covariance $\langle w_p(t)\, w_p(t+\tau)\rangle$ is:

$$R_t(\tau) = \sigma_t^2 e^{-|\tau|/\Phi_t} + \sigma_w^2 e^{-|\tau|/\Phi_w} \cos(\omega_L \tau). \tag{4.10}$$

From this model, we can normalize by the total velocity fluctuation variance $\sigma^2 = \sigma_t^2 + \sigma_w^2$, to define the total autocorrelation

$$\rho_{ww}(\tau) = \underbrace{(1-A)e^{-|\tau|/\Phi_t}}_{\text{turbulent decay}} + \underbrace{Ae^{-|\tau|/\Phi_w} \cos(\omega_L \tau)}_{\text{damped wave oscillation}}, \tag{4.11}$$

where $A \in [0, 1]$ is the fractional wave contribution to the variance (referred to as wave fraction in the rest of the text), defined as

$$A = \frac{\sigma_w^2}{\sigma_t^2 + \sigma_w^2}. \tag{4.12}$$

The wave fraction is important to determine the share of turbulence and waves contributions. If $A \to 0$, the full autocorrelation is turbulence dominated, so the particle behaves more like a stochastic tracer. If $A \to 1$, the wave contribution dominates, so the autocorrelation is oscillatory and the particle motion depends on the wave phase. Therefore, the wave-dominated regime produces stronger coherent oscillatory motion, while the turbulence-dominated regime likely leads to more dispersion. To summarize, the turbulence and wave contributions to the variance are

$$\sigma_t^2 = (1-A)\sigma^2 \quad \text{and} \quad \sigma_w^2 = A\sigma^2. \tag{4.13}$$

Note that even though the particle buoyancy is ignored in the autocorrelation model in equation (4.11), its effects are present in our data and resulting analysis through the fitting of the model to the autocorrelation data.

The total integral timescale is obtained by integrating the normalized autocorrelation over positive lags:

$$T_L = \int_0^\infty \rho_{ww}(\tau)\,\mathrm{d}\tau = (1-A)\Phi_t + \frac{A\Phi_w}{1+\omega_L^2\Phi_w^2} = (1-A)T_{t,L} + AT_{w,L}, \tag{4.14}$$

where we redefine $T_{t,L} = \Phi_t$ and define $T_{w,L} = \Phi_w/(1+\omega_L^2\Phi_w^2)$.

Hence, we obtain a decomposed expression for the total diffusivity K:

$$K = \sigma^2 T_L, \tag{4.15}$$

$$= \sigma_t^2\Phi_t + \sigma_w^2\frac{\Phi_w}{1+\omega_L^2\Phi_w^2}, \tag{4.16}$$

$$= \sigma_t^2 T_{t,L} + \sigma_w^2 T_{w,L}, \tag{4.17}$$

$$= K_t + K_w, \tag{4.18}$$

where K_t and K_w are the turbulence and wave contributions to the total diffusivity K.

The contribution to the diffusivity is determined by the signed area under the autocorrelation function. In the limit $\Phi_t \to \infty$, the intrinsic turbulent temporal decorrelation vanishes. By contrast, as $\Phi_t \to 0$, the turbulent field becomes rapidly decorrelating, almost like white noise on the particle time scale, so the turbulent contribution decorrelates very quickly.

The wave contribution is controlled by the dimensionless parameter $\omega_L\Phi_w$. For $\omega_L\Phi_w \ll 1$, the wave loses phase coherence before completing one wave cycle, and

$$K_w \approx \sigma_w^2\Phi_w. \tag{4.19}$$

This represents a rapidly decorrelating wave component that may arise from phase diffusion, broadband wave structure, or particle sampling of a spatially varying wave field. For $\omega_L\Phi_w \gg 1$, the wave remains coherent over many cycles, but the positive and negative lobes of the oscillatory correlation largely cancel, giving

$$K_w \approx \frac{\sigma_w^2}{\omega_L^2\Phi_w}. \tag{4.20}$$

4.3 *Methods and statistics*

4.3.1 Experiments

The experiments were conducted in the Washington Air-Sea Interaction Research Facility, where wind blowing over a water channel generated a free-surface flow with turbulence and short-period waves. Particle motion was captured with large-scale shadow tracking (LSST), which provided long, high-resolution two-dimensional trajectories of individual particles over a 1 m × 0.45 m field of view at 30 Hz, resolving streamwise and vertical positions while leaving the spanwise coordinate unobserved.

Since LSST records only particle trajectories, we characterized the surrounding flow independently using a Nortek Vectrino acoustic Doppler velocimeter (ADV). We mounted the ADV probe vertically above the tank and measured all three fluid-velocity components over the water depth. At each measurement point, the ADV made eight vertical measurement cells spaced 4 mm apart. The measurements were collected at 50 Hz for 2 minutes at each location.

For details about the experimental facility and data processing, see Baker and DiBenedetto (2023) and for details about the flow and particle processing and characterization in the wind-driven boundary layer, see section 3.3.

4.3.2 Lagrangian statistics

In this section we summarize our approach for analyzing the Lagrangian data. We estimate the Lagrangian autocorrelation of vertical velocity separately within vertical depth bins to account for the vertical variability in the flow field. For each bin $\mathcal{B}$, we identify all track segments that start in the bin, use these segments to estimate the conditional mean velocity and its fluctuations, and then average the products of the fluctuations to obtain the autocorrelation. To remove the mean motion and obtain the fluctuations w_p, we follow the unbiased mean flow estimator from (Machicoane and Volk, 2016), although there are other estimators in the literature (e.g., Guala et al., 2007).

We compute a depth-conditioned Lagrangian mean velocity profile $\langle w_p(\tau, \mathcal{B})\rangle$ for each bin $\mathcal{B}$ and each time lag τ. For each particle track with index $\mathcal{P}$ and each bin $\mathcal{B}$, we identify all time instants t_0 at which the particle is located within $\mathcal{B}$. For every such t_0, we define a *segment* as the portion of the trajectory that begins at t_0 and extends forward until either the end of the track or the maximum lag is reached. For a lag τ, we retain only those segments whose initial position t_0 lies within bin $\mathcal{B}$ and for which the lagged value at $t_0 + \tau$ is available

$$\mathcal{S}_{\mathcal{P},\mathcal{B}}(\tau) = \left\{ t_0 : z_p^{(\mathcal{P})}(t_0) \in \mathcal{B},\ t_0 + \tau \leq T_{\mathcal{P}} \right\}, \tag{4.21}$$

where $T_{\mathcal{P}}$ is the duration of trajectory $\mathcal{P}$. The Lagrangian mean vertical velocity in bin $\mathcal{B}$ at lag τ is then obtained by averaging the vertical velocity over all valid starting times and all trajectories

$$\langle w_p(\tau, \mathcal{B}) \rangle = \frac{1}{N(\tau, \mathcal{B})} \sum_{\mathcal{P}} \sum_{t_0 \in \mathcal{S}_{\mathcal{P},\mathcal{B}}(\tau)} w_p^{(\mathcal{P})}(t_0 + \tau), \tag{4.22}$$

and the number of valid samples contributing to bin $\mathcal{B}$ at lag τ is

$$N(\tau, \mathcal{B}) = \sum_{\mathcal{P}} \left| \mathcal{S}_{\mathcal{P},\mathcal{B}}(\tau) \right|, \tag{4.23}$$

where $\left| \mathcal{S}_{\mathcal{P},\mathcal{B}}(\tau) \right|$ is the number of valid starting times in that bin. We then calculate the vertical velocity fluctuation relative to the bin mean velocity as

$$w_p(\tau, \mathcal{B}) = w_p(\tau, \mathcal{B}) - \langle w_p(\tau, \mathcal{B}) \rangle. \tag{4.24}$$

Having estimated the velocity fluctuation, we estimate ρ_{ww} for each depth bin as

$$\rho_{ww}(\tau, \mathcal{B}) = \frac{\langle w_p(t_0, \mathcal{B}) w_p(\tau + t_0, \mathcal{B}) \rangle}{\langle w_p(t_0, \mathcal{B})^2 \rangle}, \tag{4.25}$$

where the averages are taken over every segment that contributes to a given lag.

4.3.3 Model fitting and error estimation

To separate the turbulent and wave contributions, we fit the measured autocorrelation obtained from Equation (4.25) in each depth bin to the parametric autocorrelation model introduced in Equation (4.11). The model was fitted independently in each depth bin using nonlinear least squares. Bins containing fewer than five valid lag values were excluded from the fitting procedure. For each valid bin, we minimized the unweighted sum of squared residuals,

$$\min_{\boldsymbol{\theta}} \sum_{i=1}^{N_{\mathcal{B}}} \left[\rho_{\text{data}}(\tau_i, \mathcal{B}) - \rho_{\text{model}}(\tau_i, \mathcal{B}; \boldsymbol{\theta})\right]^2 , \tag{4.26}$$

where $\boldsymbol{\theta} = [\Phi_t,\ \Phi_w,\ A,\ \omega_L]$, is the vector of fitted model parameters, ρ_{model} is the autocorrelation predicted by the model, and ρ_{data} the autocorrelation estimated directly from the data, τ_i is the ith lag time included in the fit for bin $\mathcal{B}$, and $N_{\mathcal{B}}$ is the number of valid lag-time points. The fitted parameter confidence intervals were calculated from the residuals and the nonlinear least-squares Jacobian using a 95% confidence level. The parameter covariance matrix was used to propagate parameter uncertainty to the variance and integral time-scale components.

The goodness-of-fit of the autocorrelation model in (4.11) to the data is quantified via the normalized error

$$\xi = \frac{\left\|\rho_{\text{data}} - \rho_{\text{model}}\right\|_2^2}{\left\|\rho_{\text{data}}\right\|_2^2},$$

where $\|\cdot\|_2$ is the 2-norm.

4.4 *Results and Discussion*

In this section we present our results. We first compare Lagrangian and Eulerian velocity autocorrelations and focus on how wave and turbulence along with particle properties affect the autocorrelations as a function of depth. We then introduce a parametric model that separates turbulent from wave motion and examines the fitted parameters for both reference frames. Finally, these contributions are combined to estimate vertical diffusivity, showing that turbulence dominates particle transport and that normalized diffusivity decreases with increasing buoyancy because of the crossing-trajectories effect.

4.4.1 Velocity autocorrelation

First, we compare the Lagrangian and Eulerian velocity autocorrelations. The Lagrangian autocorrelations we plot from the smallest spheres and the Eulerian autocorrelation data comes from the

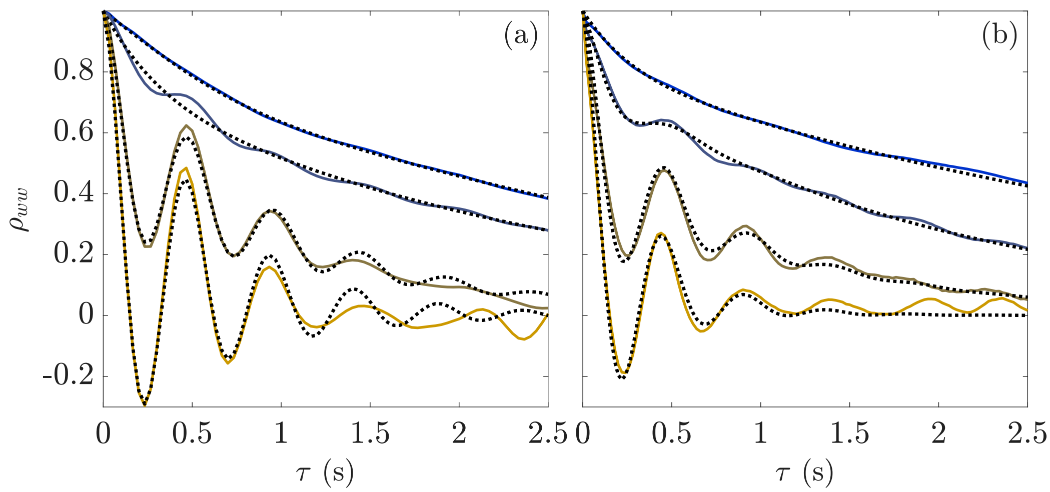

Figure 4.1: (a) Lagrangian and (b) Eulerian vertical velocity autocorrelation $\rho_{ww}(\tau, z)$ for small spheres at 12 m/s wind speed at four representative depths z: 0–8 cm (yellow), 8–15 cm, 15–25 cm and 25–40 cm (blue). We used the same vertical binning for the Eulerian and Lagrangian measurements so we can compare them. The dotted black lines show the fit of the parametric model (4.11) to each autocorrelation.

fixed ADV measurements. We plot the vertical velocity autocorrelations $\rho_{ww}(\tau, z)$ at four depths bins under 12 m/s wind speeds in figure 4.1. We see that overall, the Lagrangian and Eulerian autocorrelations resemble each other. For example, near the surface, there is a strong wave signal that gets weaker with depth. The lowest depth bin has almost no oscillatory wave signal. In addition, we see that the decay of the autocorrelations over time is faster near the surface and slower at depth. This is expected given the turbulence is stronger near the surface where we expect a shorter integral timescale.

Although similar, there are clear differences between the Lagrangian and Eulerian ρ_{ww}. For example, the Lagrangian autocorrelations tend to decay more rapidly at short times than the corresponding Eulerian curves. This is expected since a particle with a net upward drift crosses turbulent eddies more quickly than a fixed measuring point, shortening its correlation time through the crossing-trajectories effect. In addition, the wave oscillations have a higher amplitude in the

Lagrangian ρ_{ww}. This means the wave signal is more coherent overtime in the Lagrangian data as compared with the Eulerian data. This is likely explained by the fact that the Lagrangian particles follow the flow, moving in the direction of the waves, whereas the waves pass by the Eulerian sensor (which is also subject to a mean flow).

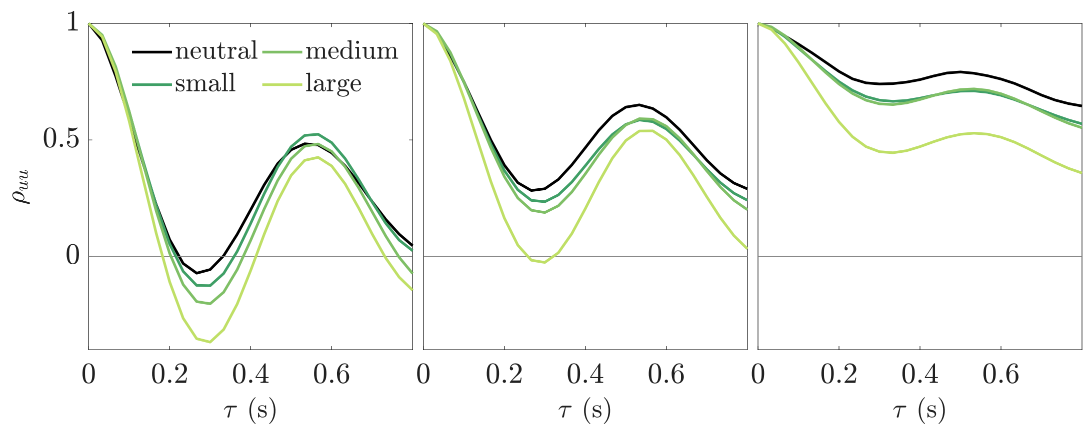

Figure 4.2: Horizontal velocity autocorrelation $\rho_{ww}(\tau, z)$ for spheres at 12 m/s wind speed at three representative depths z: left 5–12 cm, center 12–20 cm, and right 20–33 cm. The neutral particles are shown as black lines in each panel. Only spheres are shown here for clarity; rods and disks exhibit the same trends (not shown).

We also plot the Lagrangian autocorrelation for the different spherical particles in Figure 4.2. Specifically, we plot the horizontal velocity autocorrelation ρ_{uu} for spheres at 12 m/s at three depth bins, with neutral particles (our closest approximation to fluid tracers) in black included in each figure for reference. This plot helps to demonstrate the crossing-trajectories effect from Csanady (1963) that we expect for particles with a drift velocity. As particle buoyancy increases, ρ_{uu} decays progressively faster, with the neutral particles (black) retaining the longest correlation and the autocorrelation for the largest spheres decaying most rapidly. This trend is consistent across all three depth bins.

4.4.2 Parameters from the autocorrelation model fitting

Motivated by these observations, we derive the equation (4.11) as a simple parametric model that can capture the two dominant signatures visible in figures 4.1, and 4.2: (i) an oscillatory wave component and (ii) a non-oscillatory turbulent component. Recall that $\rho_{ww}(\tau)$ is a linear combination of an exponentially decaying turbulent term and an exponentially decaying sinusoidal wave term. Therefore, the model resolves surface wave oscillations and rapid turbulent decay, adjusting the wave energy fraction A and decay time Φ_t at intermediate depths. At greater depths, where wave effects vanish, the model reduces to a purely turbulent exponential decay. Finally, we note that although the waves in the tank are broadband in nature, we find that a single wave frequency in the autocorrelation model is able to capture the majority of the oscillatory motion.

We fit this two-component autocorrelation model to the measured $\rho_{ww}(\tau)$ for all particle shapes and sizes and wind speeds at each depth bin. For comparison, we also fit the model to the depth-binned Eulerian measurements. The solid black lines in figures 4.1 and 4.2 show the fit of the parametric model (4.11) to each autocorrelation. The model reproduces the broadband turbulent background together with the wave-frequency peak, with the peak weakening and the spectrum becoming increasingly dominated by turbulence with increasing depth. Thus, despite the simplicity of this model, it reproduces the measured $\rho_{ww}(\tau)$ well across depths, particle types, and wind speeds, as it is able to capture both the turbulent decay over time and the damped wave oscillation, with normalized fitting errors below 1%, as explained in section 4.3.3.

The fitted Lagrangian parameters $\Phi_{t,L}$, $\Phi_{w,L}$, A_L, and ω_L are plotted as functions of depth in Figure 4.3. The turbulent decay time $\Phi_{t,L}$ increases with depth and decreases with wind speed. Stronger near-surface turbulence produces faster decorrelation, while deeper in the water column the signal from the relatively larger eddies lead to longer correlation times. The wave coherence time $\Phi_{w,L}$ shows a different trend, slightly decreasing with depth as the wave orbital signal attenuates away from the surface. It also increases with wind speed, consistent with larger waves maintaining coherence over longer timescales. The wave fraction A_L is largest near the surface where it approaches unity and decreases with depth, following the decay of the wave orbital motion. At the

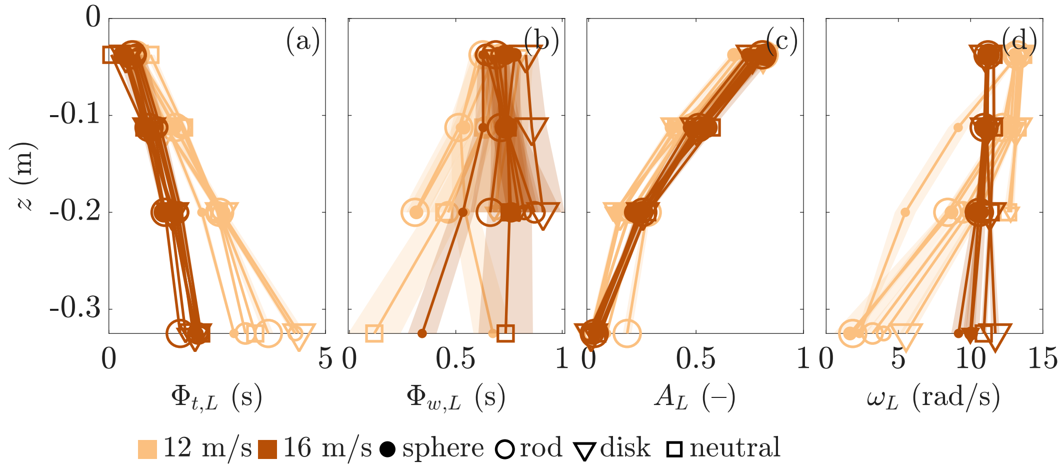

Figure 4.3: Depth profiles of the Lagrangian autocorrelation model parameters: (a) turbulent decay time $\Phi_{t,L}$, (b) wave coherence time $\Phi_{w,L}$, (c) wave contribution fraction A_L, and (d) dominant wave frequency ω_L.

deepest depths, $A_L \to 0$. The dominant frequency ω_L remains close to the peak wave frequency near the surface and becomes noisier at depth where the wave signal is weak.

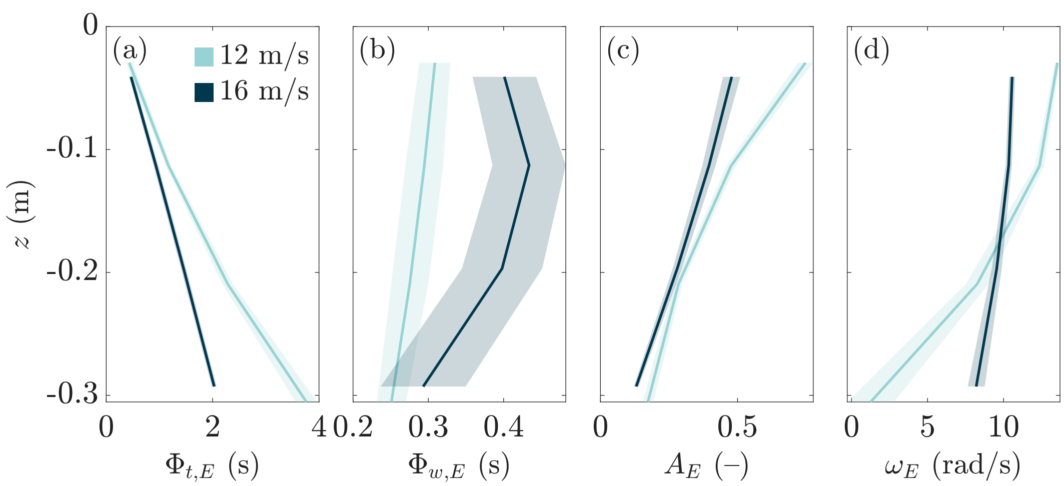

Figure 4.4: Depth profiles of the Eulerian autocorrelation model parameters: (a) turbulent decay time $\Phi_{t,E}$, (b) wave coherence time $\Phi_{w,E}$, (c) wave contribution fraction A_E, and (d) dominant wave frequency ω_E.

Applying the same parametric model to the Eulerian autocorrelations yields the fitted Eulerian parameters $\Phi_{t,E}$, $\Phi_{w,E}$, A_E, and ω_E, shown in figure 4.4. The overall trends mirror the parameters obtained from the Lagrangian fits. We see that $\Phi_{t,E}$ increases with depth, $\Phi_{w,E}$ and A_E decrease with depth, and ω_E stays near the wave frequency at the surface. Comparing the Eulerian and Lagrangian values, we see that the Eulerian turbulent timescale $\Phi_{t,E}$ is smaller than most of the corresponding $\Phi_{t,L}$ values. However, one difference appears in the wave contribution fraction A_E at the higher wind speed. At 16 m/s wind speed, A_E is slightly lower and follows a steeper decrease with depth than compared to the Lagrangian data. We attribute this to enhanced wave breaking at the higher wind speed, which injects turbulent kinetic energy near the surface and partially converts coherent wave motions into turbulence. We expect wave breaking to be underrepresented in the Lagrangian data because the particle are slightly harder to track under the strongest breaking events.

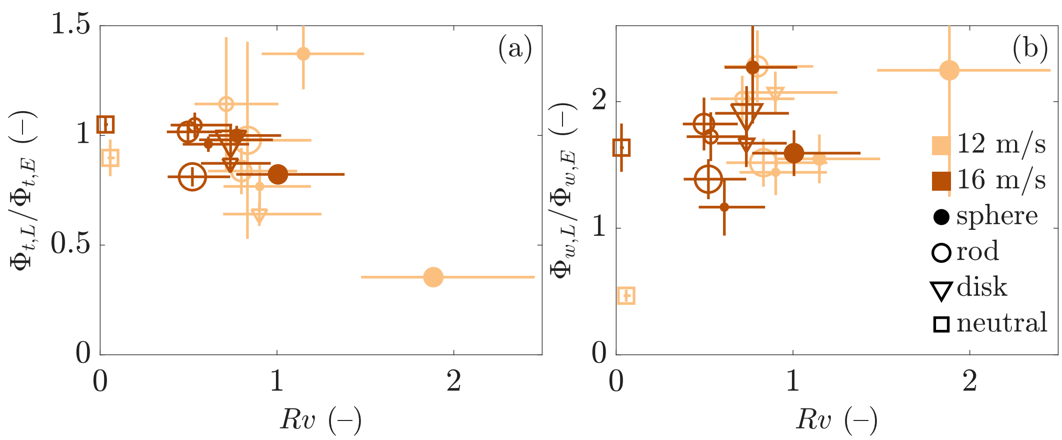

Figure 4.5: (a) Lagrangian and (b) Eulerian non-dimensional time scale in the depth range 20–30 cm. The error bars include the uncertainty associated with the estimates.

We next quantify the difference between the Lagrangian and Eulerian decorrelation time scales by comparing their turbulent and wave timescales in Figure 4.5. We plot the data for all particle types as a function of Rv. The turbulent timescale ratio $\Phi_{t,L}/\Phi_{t,E}$ in figure 4.5a ranges mostly below approximately 1. The ratio does shows a monotonic decrease with Rv for the buoyant particles in both wind speed conditions. A decrease with increasing Rv is consistent with the crossing-trajectories effect. In addition, the fact that the ratio is approximately unity indicates that the two measurements capture a similar turbulent decorrelation timescale. In contrast, we see that the wave timescale ratio $\Phi_{w,L}/\Phi_{w,E}$ plotted in figure 4.5b is greater than unity, with most values between approximately 1.6 and 2.1. This means that the Eulerian time-series wave velocity signal decorrelates faster than the wave velocity signal following the particle trajectories. This can likely be explained because the particles move with the waves so their wave signal will decorrelate slower than that of a fixed observer. The two measurements therefore sample the wave field differently (Longuet-Higgins, 1986). In addition, the mean flow in the tank means that the turbulent eddies and waves will advect past the Eulerian measuring point which could also partially explain why the $\Phi_{w,E}$ values are shorter than the corresponding $\Phi_{w,L}$ values.

4.4.3 Variance and timescale separation

Recall that since $K = \sigma_L^2 T_L$, we need both the fluctuation variance and Lagrangian time scale to determine the diffusivity. We can further separate the turbulent and wave contributions to each term using the autocorrelation model. Thus, in this section, we decompose the velocity fluctuation variance σ_L^2 into its turbulent and wave contributions: $\sigma_{t,L}^2$ and $\sigma_{w,L}^2$, where the sum of the two is equal to the total velocity fluctuation variance. We also decompose the Lagrangian time scale T_L into its turbulent and wave components: $T_{t,L}$ and $T_{w,L}$, where recall that $T_L = (1 - A)T_{t,L} + AT_{w,L}$. These values all come directly from the model fitting to the autocorrelations.

We plot σ_w^2, σ_t^2, and their sum σ_L^2 in Figures 4.6(a-c) as a function of depth for all particles under both wind speeds. Note that we do not consider the deepest point for the large spheres in 12 m/s wind because there are too few particles at this depth to provide robust estimates. In figure 4.6a, we see that the wave contribution σ_w^2 is largest near the surface and decays with depth, following the decay of wave orbital motion away from the water surface. The turbulent contribution σ_t^2 plotted in figure 4.6b is smaller near the surface but remains relatively constant over depth, so it becomes the dominant part of the total variance in the deeper bins. This follows the plots of A shown earlier, where $A < 0.5$ values correspond to depths where the turbulence contribution to the velocity variance dominates over the waves' contribution. Thus, the total variance σ_L^2 in figure 4.6c

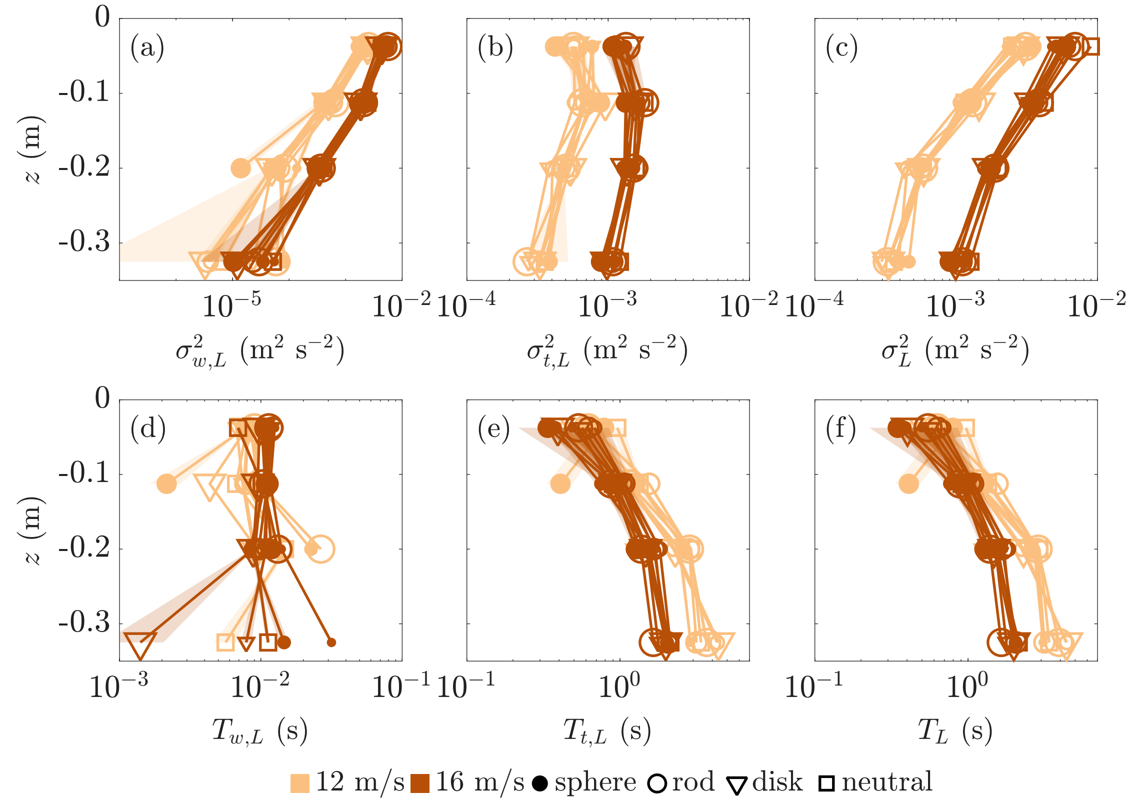

Figure 4.6: (a–c) Lagrangian vertical velocity variance, σ^2, associated with waves, turbulence, and their total. (d–f) Lagrangian integral time scale, T_L, associated with waves, turbulence, and their total.

transitions from being wave-dominated close to the free surface to turbulence-dominated farther below. In addition, we see that σ_L^2 is largest just beneath the surface and decays rapidly with depth, while stronger winds produce larger σ_L^2 at all depths. All of the particle types tend to follow similar trends, and thus we find that particle shape has only a minor effect on the vertical velocity variance, suggesting that in these experiments, the velocity variance is controlled primarily by the flow rather than by particle geometry.

Next, we plot $T_{t,L}$, $T_{w,L}$, and the total integral time scale T_L as a function of depth in figures 4.6d-f. The two timescales have contrasting behavior over depth: $T_{t,L}$ increases with depth (following the earlier plot of $\Phi_{t,L}$), but $T_{w,L}$ is relatively constant with depth. However, we see that the resulting T_L

closely follows the turbulent component $T_{t,L}$, indicating that the wave contribution to the integral timescale is small, likely due to its oscillatory signal in time. We again note that differences between particle shapes are small compared to the difference across depth and wind-speeds. This indicates that the Lagrangian time scales are primarily set by the flow, with only weak sensitivity to particle geometry and is consistent with results for slightly settling particles in turbulent boundary-layer experiments (Baker, 2021).

4.4.4 Diffusivity

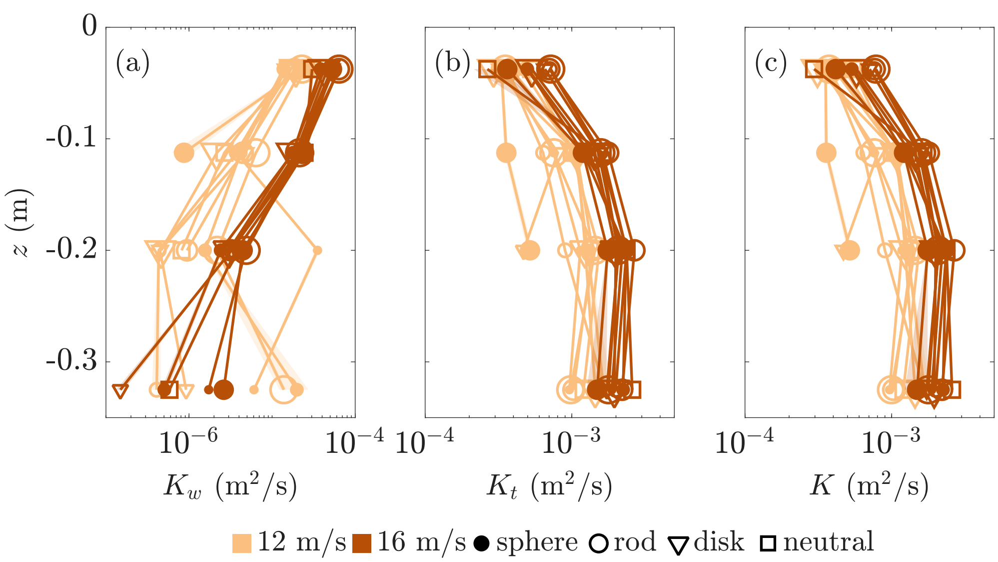

Figure 4.7: Depth dependence of the (a) wave and (b) turbulent contributions to the total vertical diffusivity (c) for different particle shapes and wind speeds.

Having quantified both the individual contributions to velocity variance and integral timescales from the waves and turbulence, we now plot the resulting diffusivity profiles. In figure 4.7a, we plot the wave contribution K_w, and in figure 4.7b, we plot the turbulence contribution K_t. We observe that $K_t \gg K_w$ over all depths, and therefore we find that the turbulence is responsible for the majority of the diffusive transport of the particles. The two components of diffusivity also follow different trends with depth: K_w peaks at the surface and decreases with depth whereas K_t is smallest at the surface and increases to a relatively constant value over depth. With respect to K_t, the opposing trends observed in σ_t^2 and $T_{t,L}$ over depth from figures 4.6b and 4.6e largely compensate to cause K_t to tend towards the approximately uniform profile below the surface. Finally, we plot the total diffusivity K in figure 4.7c, which is the sum of the wave and turbulent contributions, where we see the curves follow those of K_t almost exactly. We see some variation with respect to particle size and shape, as expected given the crossing-trajectories effect we observed in section 3.4.1.

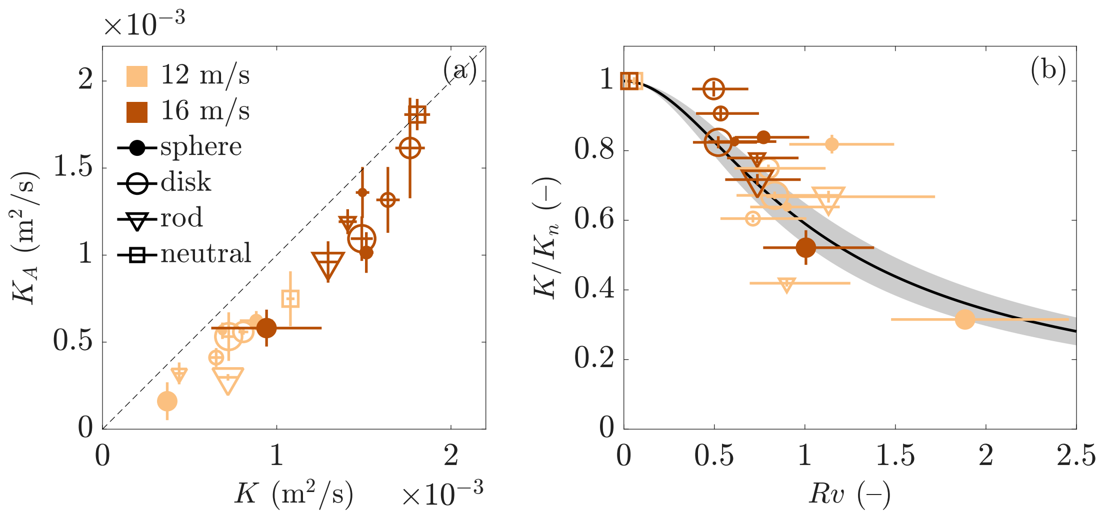

Figure 4.8: Comparison of K_A versus K. The dashed line indicates one-to-one agreement. (b) Normalized diffusivity K/K_n as a function of Rv, together with the fitted relation from (4.1) shown by the black curve. For K_A, the confidence intervals are obtained from the standard deviation of the estimate. The intervals for K and K/K_n are propagated from their respective estimated confidence intervals.

From these diffusivity profiles, we compute an effective diffusivity per experiment using the particles' distribution over the water column and compare the terms that contribute the most with the diffusivity estimated from particle mean-square displacement K_A as in (4.4) (e.g., see §3.4.1). We plot the two estimates against each other in Figure 4.8a. We see the two independent estimates of diffusivity follow close to a one-to-one relationship, indicating strong agreement. The turbulence-only term K_t is responsible for most of the total diffusivity K, as shown in Figure 4.7, which agrees well with K_A. This means that turbulence motion contributes most of the mixing. While the autocorrelation approach tends to slightly overestimate the diffusivity estimated from the particle dispersion, it tracks relative changes in mixing across particles and wind speeds well. To isolate the specific influences of particle buoyancy from the background turbulence, we normalize the results by the neutral tracer baseline, as shown in Figure 4.8b, and plot the ratio as a function of Rv. Here, the normalized diffusivity K/K_n, where K_n is the neutral particle's diffusivity, decreases with increasing buoyancy, following Csanady's theory with best-fit $C = 1.4 \pm 0.2$. This further confirms that the crossing-trajectories effect due to drift velocity is a dominant mechanism governing vertical transport in this regime, consistent with previous observations for buoyant droplets in isotropic turbulence (Gopalan et al., 2008) and our results in section 3.4.

4.5 *Conclusions*

This study investigated the effects of surface waves and turbulence on the dispersion of nearly buoyant, finite-size particles in a wind-driven free-surface boundary layer. The measurements combined Lagrangian particle tracks with Eulerian velocity measurements under different wind speeds, particle rise velocities, shapes, and sizes.

The main challenge in our experiments is that the observed dynamics were due in part to both turbulent and wave-induced motions. Another challenge inherent to studying boundary layers is that the flow is vertically inhomogeneous. To address this challenge, we developed a two-component model for the Lagrangian velocity autocorrelation. The model captures the turbulent contribution as an exponential decay and the wave contribution as a damped oscillation with its own decay time. By fitting the data to the model, we obtained estimates of the turbulent and wave contributions to both the velocity variance and the integral time scale. Applying the same model to the Eulerian measurements allowed us to compare the wave and turbulent contributions in the two reference frames.

Overall, we found that the autocorrelation model was able to accurately reproduces the measured Lagrangian correlations across all particle shapes, sizes, wind speeds, and depths considered in this study. From analyzing the results of the model, we find that the Lagrangian turbulent correlation time, normalized by the Eulerian turbulent correlation time, decreases with increasing particle buoyancy, consistent with crossing-trajectories effect. We also confirm see that particle shape and size play a secondary role, as seen in section 3. In contrast, the wave time scale inferred from the Lagrangian measurements is generally longer than that obtained from the Eulerian measurements. A possible explanation is that particles move with the wave-induced motion, whereas an Eulerian fixed-point observer sees the wave field as it passes by the measurement location.

From the model fits we find that the wave contribution to the variance is largest near the free surface and decreases rapidly with depth, while the turbulent contribution persists farther into the water column. As a result, the velocity variance is strongly influenced by waves near the surface and by turbulence at depth. Regarding the integral time scale, the turbulence is several order of magnitude larger than the wave component. Consequently, the waves net contribution to long-time diffusivity is relatively small compared to turbulence which provides most of the contribution to the effective long-time diffusive transport.

Taken together, these measurements provide the first direct experimental demonstration that wave and turbulent contributions can be separated in Lagrangian particle data from a realistic free-surface boundary layer. Despite the turbulence, surface waves, and even wave breaking, the model identifies a turbulent contribution to particle diffusivity that agrees with an independent dispersion-based estimate.

Chapter 5

CONCLUSIONS AND FUTURE WORK

5.1 *Conclusions*

This dissertation investigates the transport of nearly buoyant, finite-sized particles in a wind-driven free-surface boundary layer using laboratory experiments, data-driven analysis, and analytical modeling. The complexity between particle properties and flow dynamics, and the resulting modulation of particle mixing and rise velocity, motivates this dissertation. The main result shows that particle buoyancy is the primary control on vertical turbulent diffusivity in our experiments and the effective rise velocity is substantially lower than the corresponding quiescent rise velocity. This result demonstrates that an accurate vertical transport estimation of buoyant particles cannot ignore flow-particle dynamics at the scale of the waves.

The first contribution was a data-driven separation framework for Eulerian time series measurements. In Chapter 2 we developed an algorithm that isolates coherent wave motion from broadband turbulence even when the two overlap in frequency space, based on Dynamic Mode Decomposition. The algorithm is signal agnostic so it can be applied to any time series, and our only assumptions are that the waves and turbulence can be separated and that the waves are the most coherent features in the signal. Our approach required minimal tuning, where the main user input is the wave frequency range of interest. To demonstrate the method, we applied it to synthetic, field, and laboratory data and compare the results to other modal decomposition methods. A sensitivity analysis on the synthetic data showed that the decomposition performs the best when the wave energy in the signal is of equal or greater magnitude than that of the turbulence. Given the accuracy of our decomposition, we are able to analyze the velocity autocorrelation of the separated turbulence time series with minimal wave contamination. Overall, our decomposition method outperforms the other decomposition methods and provides for robust separation of the waves and turbulence, demonstrating wide applicability to ocean signal processing. This is important because, without an explicit separation, wave and turbulence contributions are conflated in the measured statistics.

In Chapter 3, we experimentally studied the vertical mixing of buoyant, finite-sized spheres, rods, and disks in a wind-driven free-surface flow and compared their vertical diffusivities, estimated directly from Lagrangian trajectories and from simplified transport models that use Eulerian measurements. From this comparison, we found that diffusivity decreases as particle buoyancy dominates turbulent mixing, consistent with the crossing-trajectories effect. Similarly, the decrease in particle diffusivity relative to momentum diffusivity follows the same trend, yielding Schmidt numbers greater than one. The results showed that simple estimates based on quiescent rise velocity can overpredict mixing and depth penetration. We conclude that assuming a still-water rise velocity in concentration-based models significantly overestimates diffusivity because the flow reduces the particle rise velocity relative to its still-water velocity. In this regime, the relevant transport quantity is an effective rise velocity that already reflects the interaction between the particle and the surrounding flow. Overall, we find that the flow and particle characteristics can both affect the particle diffusivity and rise velocity in non-trivial ways. These effects are often overlooked in microplastic transport models which can introduce substantial errors.

Motivated by these findings, in Chapter 4, we separate waves and turbulence contributions to the particle eddy diffusivity using a stochastic model for the Lagrangian vertical autocorrelation function. The model represents the measured autocorrelation as the sum of a monotonically decaying turbulent component and a damped oscillatory wave component. The main result of the autocorrelation analysis is that the turbulence-only term of the integral time scale captures the MSD-based diffusivity well and therefore represents the dominant mixing. The wave contribution is strongest in the velocity fluctuation variance and is strongest near the surface and weakens with depth.

Taken together, the three chapters show that wave and turbulence interactions can matter at every stage of the transport problem. The main conclusion is that near-surface particle transport cannot be reduced to a single eddy diffusivity without accounting for the crossing-trajectories effect.

5.2 *Future work*

Since particle rise velocity is a fundamental parameter for buoyant particles transport, a next step would be to measure co-located PIV data with tracers and particles to estimate the slip velocity directly and identify the mechanisms that reduce it. In unsteady flows, research shows that the average rise velocity can differ from its still-water value through two mechanisms: the particle may sample a nonzero mean fluid velocity due to preferential sampling (Friedman and Katz, 2002), or its mean slip velocity may shift due to nonlinear drag (Good et al., 2014; Ruth et al., 2021; Liu et al., 2024). Additional forces like added mass and Basset history force can further reduce this velocity (Guseva et al., 2016; Li et al., 2023). We could explore how much of the rise velocity reduction comes from the particle preferentially sampling fluid regions vs. from nonlinear drag reducing the vertical slip in response to horizontal velocity fluctuations. Additionally, we could test whether the analytical slip velocity model of Berk and Coletti (2024) applies to near-buoyant particles in a wavy flow, or whether modifications are needed to account for waves.

A natural extension of Chapter 4 is to generalize the autocorrelation model to include particle inertia and buoyancy explicitly through the particle equation of motion, similar to Pismen and Nir (1978) but without modeling the entire fluid velocity field. Our model treats the sampled vertical velocity as a superposition of turbulent and wave-induced fluctuations, but it does not yet resolve how finite response time and buoyancy drift. These effects can modify the autocorrelation, the mean-square displacement, and the effective diffusivity. Extending the model in that direction would allow the response time to enter the theory directly, rather than only through empirical fitting or effective parameters. The MSD and diffusivity evolution can be extracted from this generalized model to connect the particle motion equation directly to transport predictions. That would make it possible to test whether the same wave-turbulence mechanism that explains the autocorrelation also explains the time evolution of dispersion and the ballistic-to-diffusive transition. If successful, this would turn the present model into a predictive framework for nearly buoyant particles in free-surface boundary layers, with direct relevance to microplastic transport, oil droplets, and other environmental particles.

BIBLIOGRAPHY

Abreu, A. and Pedrotti, M. L. (2019). Microplastics in the oceans: The solutions lie on land. *Field Actions Science Reports. The journal of field actions*, (Special Issue 19):62–67.

Aiyer, A. K. and Meneveau, C. (2022). Resolved and subgrid-scale crossing trajectory effects in Eulerian large eddy simulations of size-dependent droplet transport. *Journal of Fluid Mechanics*, 935:A15.

Albidah, A. B., Brevis, W., Fedun, V., Ballai, I., Jess, D. B., Stangalini, M., Higham, J., and Verth, G. (2021). Proper orthogonal and dynamic mode decomposition of sunspot data. *Philosophical transactions. Series A, Mathematical, physical, and engineering sciences*, 379(2190):20200181.

Aliseda, A., Cartellier, A., Hainaux, F., and Lasheras, J. C. (2002). Effect of preferential concentration on the settling velocity of heavy particles in homogeneous isotropic turbulence. *Journal of Fluid Mechanics*, 468:77–105.

Aliseda, A. and Lasheras, J. C. (2011). Preferential concentration and rise velocity reduction of bubbles immersed in a homogeneous and isotropic turbulent flow. *Physics of Fluids*, 23(9):093301.

Allen, D., Allen, S., Abbasi, S., Baker, A., Bergmann, M., Brahney, J., Butler, T., Duce, R. A., Eckhardt, S., Evangeliou, N., Jickells, T., Kanakidou, M., Kershaw, P., Laj, P., Levermore, J., Li, D., Liss, P., Liu, K., Mahowald, N., Masque, P., Materić, D., Mayes, A. G., McGinnity, P., Osvath, I., Prather, K. A., Prospero, J. M., Revell, L. E., Sander, S. G., Shim, W. J., Slade, J., Stein, A., Tarasova, O., and Wright, S. (2022). Microplastics and nanoplastics in the marine-atmosphere environment. *Nature Reviews Earth & Environment*, 3(6):393–405.

Alsina, J. M., Jongedijk, C. E., and van Sebille, E. (2020). Laboratory Measurements of the Wave-

Induced Motion of Plastic Particles: Influence of Wave Period, Plastic Size and Plastic Density. *Journal of Geophysical Research: Oceans*, 125(12):e2020JC016294.

Andrady, A. L. (2011). Microplastics in the marine environment. *Marine Pollution Bulletin*, 62(8):1596–1605.

Araya, D. B., Colonius, T., and Dabiri, J. O. (2017). Transition to bluff-body dynamics in the wake of vertical-axis wind turbines. *Journal of Fluid Mechanics*, 813:346–381.

Ardhuin, F., Herbers, T. H. C., Watts, K. P., van Vledder, G. P., Jensen, R., and Graber, H. C. (2007). Swell and Slanting-Fetch Effects on Wind Wave Growth. *Journal of Physical Oceanography*, 37(4):908–931.

Aubry, N., Holmes, P., Lumley, J. L., and Stone, E. (1988). The dynamics of coherent structures in the wall region of a turbulent boundary layer. *Journal of Fluid Mechanics*, 192:115–173.

Babanin, A. V. and Haus, B. K. (2009). On the Existence of Water Turbulence Induced by Nonbreaking Surface Waves. *Journal of Physical Oceanography*, 39(10):2675–2679.

Baker, L. J. (2021). *Experimental Investigation of Inertial Sphere, Rod, and Disk Particles in a Turbulent Boundary Layer*. PhD thesis, University of Minnesota.

Baker, L. J. and Coletti, F. (2021). Particle–fluid–wall interaction of inertial spherical particles in a turbulent boundary layer. *Journal of Fluid Mechanics*, 908:A39.

Baker, L. J. and Coletti, F. (2022). Experimental investigation of inertial fibres and disks in a turbulent boundary layer. *Journal of Fluid Mechanics*, 943:A27.

Baker, L. J. and DiBenedetto, M. (2023). Large-scale particle shadow tracking and orientation measurement with collimated light. *Experiments in Fluids*, 64(3):52.

Balachandar, S. and Eaton, J. K. (2010). Turbulent Dispersed Multiphase Flow. *Annual Review of Fluid Mechanics*, 42(Volume 42, 2010):111–133.

Bec, J., Biferale, L., Cencini, M., Lanotte, A., Musacchio, S., and Toschi, F. (2007). Heavy Particle Concentration in Turbulence at Dissipative and Inertial Scales. *Physical Review Letters*, 98(8):084502.

Benilov, A. Yu., Kouznetsov, O. A., and Panin, G. N. (1974). On the analysis of wind wave-induced disturbances in the atmospheric turbulent surface layer. *Boundary-Layer Meteorology*, 6(1):269–285.

Berk, T. and Coletti, F. (2024). An analytical model for the slip velocity of particles in turbulence. *Journal of Fluid Mechanics*, 996:A1.

Bian, C., Liu, Z., Huang, Y., Zhao, L., and Jiang, W. (2018). On Estimating Turbulent Reynolds Stress in Wavy Aquatic Environment. *Journal of Geophysical Research: Oceans*, 123(4):3060–3071.

Boi, S., Mazzino, A., Muratore-Ginanneschi, P., and Olivieri, S. (2018). Generalization of Taylor's formula to particles of arbitrary inertia. *Physical Review Fluids*, 3(10):104501.

Bond, T., Ferrandiz-Mas, V., Felipe-Sotelo, M., and van Sebille, E. (2018). The occurrence and degradation of aquatic plastic litter based on polymer physicochemical properties: A review. *Critical Reviews in Environmental Science and Technology*, 48(7-9):685–722.

Boufadel, M., Liu, R., Zhao, L., Lu, Y., Özgökmen, T., Nedwed, T., and Lee, K. (2020). Transport of Oil Droplets in the Upper Ocean: Impact of the Eddy Diffusivity. *Journal of Geophysical Research: Oceans*, 125(2):e2019JC015727.

Brandt, L. and Coletti, F. (2022). Particle-Laden Turbulence: Progress and Perspectives. *Annual Review of Fluid Mechanics*, 54(Volume 54, 2022):159–189.

Braud, C., Heitz, D., Arroyo, G., Perret, L., Delville, J., and Bonnet, J.-P. (2004). Low-dimensional analysis, using POD, for two mixing layer–wake interactions. *International Journal of Heat and Fluid Flow*, 25(3):351–363.

Bricker, J. D. and Monismith, S. G. (2007). Spectral Wave–Turbulence Decomposition. *Journal of Atmospheric and Oceanic Technology*, 24(8):1479–1487.

Brunner, K., Kukulka, T., Proskurowski, G., and Law, K. L. (2015). Passive buoyant tracers in the ocean surface boundary layer: 2. Observations and simulations of microplastic marine debris. *Journal of Geophysical Research: Oceans*, 120(11):7559–7573.

Burnage, H. and Huilier, D. (1990). Diffusion of a Submicronic Spray in an Homogeneous Turbulent Flow. *Aerosol Science and Technology*, 12(3):637–649.

Byron, M. (2015). *The Rotation and Translation of Non-Spherical Particles in Homogeneous Isotropic Turbulence*. PhD thesis, University of California, Berkeley, United States – California.

Calzavarini, E., Volk, R., Bourgoin, M., Lévêque, E., Pinton, J.-F., and Toschi, F. (2009). Acceleration statistics of finite-sized particles in turbulent flow: The role of Faxén forces. *Journal of Fluid Mechanics*, 630:179–189.

Castro, I. P. and Vanderwel, C. (2021). *Turbulent Flows: An Introduction*. IOP Publishing.

Chamecki, M., Chor, T., Yang, D., and Meneveau, C. (2019). Material Transport in the Ocean Mixed Layer: Recent Developments Enabled by Large Eddy Simulations. *Reviews of Geophysics*, 57(4):1338–1371.

Chauchat, J., Hurther, D., Revil-Baudard, T., Cheng, Z., and Hsu, T.-J. (2022). Controversial turbulent Schmidt number value in particle-laden boundary layer flows. *Physical Review Fluids*, 7(1):014307.

Chávez-Dorado, J., Scherl, I., and DiBenedetto, M. (2025). Wave and Turbulence Separation Using Dynamic Mode Decomposition. *Journal of Atmospheric and Oceanic Technology*, 42(5):509–526.

Cheung, T. K. and Street, R. L. (1988). The turbulent layer in the water at an air—water interface. *Journal of Fluid Mechanics*, 194:133–151.

Chor, T., Yang, D., Meneveau, C., and Chamecki, M. (2018a). Preferential concentration of noninertial buoyant particles in the ocean mixed layer under free convection. *Physical Review Fluids*, 3(6):064501.

Chor, T., Yang, D., Meneveau, C., and Chamecki, M. (2018b). A Turbulence Velocity Scale for Predicting the Fate of Buoyant Materials in the Oceanic Mixed Layer. *Geophysical Research Letters*, 45(21):11,817–11,826.

Clark, L. K., DiBenedetto, M. H., Ouellette, N. T., and Koseff, J. R. (2020). Settling of inertial nonspherical particles in wavy flow. *Physical Review Fluids*, 5(12):124301.

Clark, L. K., DiBenedetto, M. H., Ouellette, N. T., and Koseff, J. R. (2023). Dispersion of finite-size, non-spherical particles by waves and currents. *Journal of Fluid Mechanics*, 954:A3.

Clift, R., Grace, J. R., and Weber, M. E. (2005). *Bubbles, Drops, and Particles*. Courier Corporation.

Cowherd, M., Egan, G., Monismith, S., and Fringer, O. (2021). Phase-Resolved Wave Boundary Layer Dynamics in a Shallow Estuary. *Geophysical Research Letters*, 48(8).

Cózar, A., Echevarría, F., González-Gordillo, J. I., Irigoien, X., Úbeda, B., Hernández-León, S., Palma, Á. T., Navarro, S., García-de-Lomas, J., Ruiz, A., Fernández-de-Puelles, M. L., and Duarte, C. M. (2014). Plastic debris in the open ocean. *Proceedings of the National Academy of Sciences*, 111(28):10239–10244.

Craig, P. D. and Banner, M. L. (1994). Modeling Wave-Enhanced Turbulence in the Ocean Surface Layer. *Journal of Physical Oceanography*, 24(12):2546–2559.

Craik, A. D. D. and Leibovich, S. (1976). A rational model for Langmuir circulations. *Journal of Fluid Mechanics*, 73(3):401–426.

Csanady, G. T. (1963). Turbulent Diffusion of Heavy Particles in the Atmosphere. *Journal of the Atmospheric Sciences*, 20(3):201–208.

D'Asaro, E. A. (2014). Turbulence in the Upper-Ocean Mixed Layer. *Annual Review of Marine Science*, 6(Volume 6, 2014):101–115.

Daubechies, I., Lu, J., and Wu, H.-T. (2011). Synchrosqueezed wavelet transforms: An empirical mode decomposition-like tool. *Applied and Computational Harmonic Analysis*, 30(2):243–261.

Dávila, J. and Hunt, J. C. R. (2001). Settling of small particles near vortices and in turbulence. *Journal of Fluid Mechanics*, 440:117–145.

Davis, R. (1983). Oceanic property transport, Lagrangian particle statistics, and their prediction. *Journal of Marine Research*, 41(1).

Dean, R. G. (1965). Stream function representation of nonlinear ocean waves. *Journal of Geophysical Research (1896-1977)*, 70(18):4561–4572.

DiBenedetto, M. H. (2026). The Fluid Mechanics of Ocean Microplastics. *Annual Review of Fluid Mechanics*, 58(Volume 58, 2026):355–382.

DiBenedetto, M. H., Clark, L. K., and Pujara, N. (2022). Enhanced settling and dispersion of inertial particles in surface waves. *Journal of Fluid Mechanics*, 936:A38.

DiBenedetto, M. H., Donohue, J., Tremblay, K., Edson, E., and Law, K. L. (2023). Microplastics segregation by rise velocity at the ocean surface. *Environmental Research Letters*, 18(2):024036.

Doron, P., Bertuccioli, L., Katz, J., and Osborn, T. R. (2001). Turbulence Characteristics and Dissipation Estimates in the Coastal Ocean Bottom Boundary Layer from PIV Data. *Journal of Physical Oceanography*, 31(8):2108–2134.

Duke, D., Honnery, D., and Soria, J. (2012). Experimental investigation of nonlinear instabilities in annular liquid sheets. *Journal of Fluid Mechanics*, 691:594–604.

Durgesh, V. and Naughton, J. W. (2010). Multi-time-delay LSE-POD complementary approach applied to unsteady high-Reynolds-number near wake flow. *Experiments in Fluids*, 49(3):571–583.

Eeltink, D., Calvert, R., Swagemakers, J. E., Xiao, Q., and van den Bremer, T. S. (2023). Stochastic particle transport by deep-water irregular breaking waves. *Journal of Fluid Mechanics*, 971:A38.

Einstein, A. (1905). On the movement of small particles suspended in a stationary liquid demanded by the molecular-kinetic theory of heat (English translation, 1956). *Annalen de Physik*, 17:549–560.

Farazmand, M. (2024). Extreme firebrand transport by atmospheric waves in wildfires. https://arxiv.org/abs/2411.13275v1.

Farazmand, M. and Sapsis, T. (2019). Surface Waves Enhance Particle Dispersion. *Fluids*, 4(1):55.

Farmer, D. and Li, M. (1994). Oil dispersion by turbulence and coherent circulations. *Ocean Engineering*, 21(6):575–586.

Feddersen, F. and Williams, A. J. (2007). Direct Estimation of the Reynolds Stress Vertical Structure in the Nearshore. *Journal of Atmospheric and Oceanic Technology*, 24(1):102–116.

Fernandes, P. C., Risso, F., Ern, P., and Magnaudet, J. (2007). Oscillatory motion and wake instability of freely rising axisymmetric bodies. *Journal of Fluid Mechanics*, 573:479–502.

Filho, E. V. and Lopes dos Santos, P. (2019). A Dynamic Mode Decomposition Approach With Hankel Blocks to Forecast Multi-Channel Temporal Series. *IEEE Control Systems Letters*, 3(3):739–744.

Fisher, A. W. and Nidzieko, N. J. (2024). AUV Observations of Langmuir Turbulence in a Stratified Shelf Sea. *Journal of Physical Oceanography*, 54(9):1903–1920.

Fornari, W., Picano, F., and Brandt, L. (2016a). Sedimentation of finite-size spheres in quiescent and turbulent environments. *Journal of Fluid Mechanics*, 788:640–669.

Fornari, W., Picano, F., Sardina, G., and Brandt, L. (2016b). Reduced particle settling speed in turbulence. *Journal of Fluid Mechanics*, 808:153–167.

Foster, D. L. (1997). *Dynamics of the Nearshore Wave Bottom Boundary Layer*. PhD thesis, Oregon State University, United States – Oregon.

Friedman, P. D. and Katz, J. (2002). Mean rise rate of droplets in isotropic turbulence. *Physics of Fluids*, 14(9):3059–3073.

Fujii, K., Takeishi, N., Kibushi, B., Kouzaki, M., and Kawahara, Y. (2019). Data-driven spectral analysis for coordinative structures in periodic human locomotion. *Scientific Reports*, 9(1):16755.

Garraffo, Z. D., Mariano, A. J., Griffa, A., Veneziani, C., and Chassignet, E. P. (2001). Lagrangian data in a high-resolution numerical simulation of the North Atlantic: I. Comparison with in situ drifter data. *Journal of Marine Systems*, 29(1):157–176.

Gemmrich, J. R. and Farmer, D. M. (2004). Near-Surface Turbulence in the Presence of Breaking Waves. *Journal of Physical Oceanography*, 34(5):1067–1086.

Gerbi, G. P., Trowbridge, J. H., Edson, J. B., Plueddemann, A. J., Terray, E. A., and Fredericks, J. J. (2008). Measurements of Momentum and Heat Transfer across the Air–Sea Interface. *Journal of Physical Oceanography*, 38(5):1054–1072.

Gerbi, G. P., Trowbridge, J. H., Terray, E. A., Plueddemann, A. J., and Kukulka, T. (2009). Observations of Turbulence in the Ocean Surface Boundary Layer: Energetics and Transport. *Journal of Physical Oceanography*, 39(5):1077–1096.

Giordani, H., Bourdallé-Badie, R., and Madec, G. (2020). An Eddy-Diffusivity Mass-Flux Parameterization for Modeling Oceanic Convection. *Journal of Advances in Modeling Earth Systems*, 12(9):e2020MS002078.

Good, G. H., Ireland, P. J., Bewley, G. P., Bodenschatz, E., Collins, L. R., and Warhaft, Z. (2014). Settling regimes of inertial particles in isotropic turbulence. *Journal of Fluid Mechanics*, 759:R3.

Gopalan, B., Malkiel, E., and Katz, J. (2008). Experimental investigation of turbulent diffusion of slightly buoyant droplets in locally isotropic turbulence. *Physics of Fluids*, 20(9):095102.

Gordeyev, S. V. and Thomas, F. O. (2013). A temporal proper decomposition (TPOD) for closed-loop flow control. *Experiments in Fluids*, 54(3):1477.

Goring, D. G. and Nikora, V. I. (2002). Despiking Acoustic Doppler Velocimeter Data. *Journal of Hydraulic Engineering*, 128(1):117–126.

Grilli, M., Schmid, P. J., Hickel, S., and Adams, N. A. (2012). Analysis of unsteady behaviour in shockwave turbulent boundary layer interaction. *Journal of Fluid Mechanics*, 700:16–28.

Guala, M., Liberzon, A., Tsinober, A., and Kinzelbach, W. (2007). An experimental investigation on Lagrangian correlations of small-scale turbulence at low Reynolds number. *Journal of Fluid Mechanics*, 574:405–427.

Gualtieri, C., Angeloudis, A., Bombardelli, F., Jha, S., and Stoesser, T. (2017). On the Values for the Turbulent Schmidt Number in Environmental Flows. *Fluids*, 2(2):17.

Guo, X. and Shen, L. (2013). Numerical study of the effect of surface waves on turbulence underneath. Part 1. Mean flow and turbulence vorticity. *Journal of Fluid Mechanics*, 733:558–587.

Guseva, K., Daitche, A., Feudel, U., and Tél, T. (2016). History effects in the sedimentation of light aerosols in turbulence: The case of marine snow. *Physical Review Fluids*, 1(7):074203.

Hasselmann, K., Barnett, T., Bouws, E., Carlson, H., Cartwright, D., Enke, K., Ewing, J., Gienapp, H., Hasselmann, D., Kruseman, P., Meerburg, A., Müller, P., Olbers, D., Richter, K., Sell, W., and Walden, H. (1973). Measurements of wind-wave growth and swell decay during the Joint North Sea Wave Project (JONSWAP). *Ergaenzungsheft zur Deutschen Hydrographischen Zeitschrift, Reihe A*, page 94.

Heidt, L. and Colonius, T. (2023). Spectral proper orthogonal decomposition of harmonically forced turbulent flows.

Huang, N. E., Shen, Z., Long, S. R., Wu, M. C., Shih, H. H., Zheng, Q., Yen, N.-C., Tung, C. C., and Liu, H. H. (1998). The Empirical Mode Decomposition and the Hilbert Spectrum for Nonlinear and Non-Stationary Time Series Analysis. *Proceedings: Mathematical, Physical and Engineering Sciences*, 454(1971):903–995.

Huang, N. E. and Wu, Z. (2008). A review on Hilbert-Huang transform: Method and its applications to geophysical studies. *Reviews of Geophysics*, 46(2).

Huang, Y., Schmitt, F. G., Lu, Zhiming., and Liu, Y. (2009). Analysis of daily river flow fluctuations using empirical mode decomposition and arbitrary order Hilbert spectral analysis. *Journal of Hydrology*, 373(1):103–111.

Jiang, J.-Y., Street, R. L., and Klotz, S. P. (1990). A study of wave-turbulence interaction by use of a nonlinear water wave decomposition technique. *Journal of Geophysical Research: Oceans*, 95(C9):16037–16054.

Jovanović, M. R., Schmid, P. J., and Nichols, J. W. (2014). Sparsity-promoting dynamic mode decomposition. *Physics of Fluids*, 26(2):024103.

Kukulka, T. and Brunner, K. (2015). Passive buoyant tracers in the ocean surface boundary layer: 1. Influence of equilibrium wind-waves on vertical distributions. *Journal of Geophysical Research: Oceans*, 120(5):3837–3858.

Kukulka, T., Proskurowski, G., Morét-Ferguson, S., Meyer, D. W., and Law, K. L. (2012). The effect of wind mixing on the vertical distribution of buoyant plastic debris. *Geophysical Research Letters*, 39(7).

Kumar, N., Cahl, D. L., Crosby, S. C., and Voulgaris, G. (2017). Bulk versus Spectral Wave Parameters: Implications on Stokes Drift Estimates, Regional Wave Modeling, and HF Radars Applications. *Journal of Physical Oceanography*, 47(6):1413–1431.

Kutz, J. N., Brunton, S. L., Brunton, B. W., and Proctor, J. L. (2016). *Dynamic Mode Decomposition*. Society for Industrial and Applied Mathematics, Philadelphia, PA.

LaCasce, J. H. (2008). Statistics from Lagrangian observations. *Progress in Oceanography*, 77(1):1–29.

Laist, D. W. (1987). Overview of the biological effects of lost and discarded plastic debris in the marine environment. *Marine Pollution Bulletin*, 18(6, Supplement B):319–326.

Lamb, S. H. (1930). *Hydrodynamics*. University Press.

Laxague, N. J. M., Özgökmen, T. M., Haus, B. K., Novelli, G., Shcherbina, A., Sutherland, P., Guigand, C. M., Lund, B., Mehta, S., Alday, M., and Molemaker, J. (2018). Observations of Near-Surface Current Shear Help Describe Oceanic Oil and Plastic Transport. *Geophysical Research Letters*, 45(1):245–249.

Lebreton, L., Slat, B., Ferrari, F., Sainte-Rose, B., Aitken, J., Marthouse, R., Hajbane, S., Cunsolo, S., Schwarz, A., Levivier, A., Noble, K., Debeljak, P., Maral, H., Schoeneich-Argent, R., Brambini, R., and Reisser, J. (2018). Evidence that the Great Pacific Garbage Patch is rapidly accumulating plastic. *Scientific Reports*, 8(1):4666.

Leibovich, S. (1983). The Form and Dynamics of Langmuir Circulations. *Annual Review of Fluid Mechanics*, 15(1):391–427.

Li, G., Weiss, G., Mueller, M., Townley, S., and Belmont, M. R. (2012). Wave energy converter control by wave prediction and dynamic programming. *Renewable Energy*, 48:392–403.

Li, M., Garrett, C., and Skyllingstad, E. (2005). A regime diagram for classifying turbulent large eddies in the upper ocean. *Deep Sea Research Part I: Oceanographic Research Papers*, 52(2):259–278.

Li, S., Bragg, A. D., and Katul, G. (2023). Reduced Sediment Settling in Turbulent Flows Due To Basset History and Virtual Mass Effects. *Geophysical Research Letters*, 50(22):e2023GL105810.

Li, Y., Salmon, H. S., Hassaini, R., Chang, K., Mucignat, C., and Coletti, F. (2025). Spatiotemporal scales of motion and particle clustering in free-surface turbulence. *Physical Review Fluids*, 10(3):034602.

Liu, Z., Farsoiya, P. K., Perrard, S., and Deike, L. (2024). Direct numerical simulation of bubble rising in turbulence. *Journal of Fluid Mechanics*, 999:A11.

Longuet-Higgins, M. S. (1986). Eulerian and Lagrangian aspects of surface waves. *Journal of Fluid Mechanics*, 173:683–707.

Lumley, J. L. (1967). The structure of inhomogeneous turbulent flows. *Atmospheric Turbulence and Radio Wave Propagation*, pages 166–178.

Lumley, J. L. (2007). *Stochastic Tools in Turbulence*. Courier Corporation.

Lydon, B., Polagye, B., and Brunton, S. (2023). Data-driven modeling of an oscillating surge wave energy converter using dynamic mode decomposition.

Machicoane, N. and Volk, R. (2016). Lagrangian velocity and acceleration correlations of large inertial particles in a closed turbulent flow. *Physics of Fluids*, 28(3):035113.

Magnaudet, J. and Thais, L. (1995). Orbital rotational motion and turbulence below laboratory wind water waves. *Journal of Geophysical Research: Oceans*, 100(C1):757–771.

Majda, A. J. and Kramer, P. R. (1999). Simplified models for turbulent diffusion: Theory, numerical modelling, and physical phenomena. *Physics Reports*, 314(4):237–574.

Massa, L., Kumar, R., and Ravindran, P. (2012). Dynamic mode decomposition analysis of detonation waves. *Physics of Fluids*, 24(6):066101.

Mathai, V., Lohse, D., and Sun, C. (2020). Bubbly and Buoyant Particle–Laden Turbulent Flows. *Annual Review of Condensed Matter Physics*, 11(1):529–559.

Maxey, M. R. (1987). The motion of small spherical particles in a cellular flow field. *The Physics of Fluids*, 30(7):1915–1928.

Maxey, M. R. and Riley, J. J. (1983). Equation of motion for a small rigid sphere in a nonuniform flow. *The Physics of Fluids*, 26(4):883–889.

Mazzitelli, I. M. and Lohse, D. (2004). Lagrangian statistics for fluid particles and bubbles in turbulence. *New Journal of Physics*, 6(1):203.

McWilliams, J. C., Sullivan, P. P., and Moeng, C.-H. (1997). Langmuir turbulence in the ocean. *Journal of Fluid Mechanics*, 334:1–30.

Mei, R., Adrian, R. J., and Hanratty, T. J. (1997). Turbulent Dispersion of Heavy Particles With Nonlinear Drag. *Journal of Fluids Engineering*, 119(1):170–179.

Melville, W. K. (1996). The Role of Surface-Wave Breaking in Air-Sea Interaction. *Annual Review of Fluid Mechanics*, 28:279–321.

Murray, S. P. (1970). Settling velocities and vertical diffusion of particles in turbulent water. *Journal of Geophysical Research*, 75(9):1647–1654.

Nir, A. and Pismen, L. M. (1979). The effect of a steady drift on the dispersion of a particle in turbulent fluid. *Journal of Fluid Mechanics*, 94(2):369–381.

Noh, Y., Kang, I. S., Herold, M., and Raasch, S. (2006). Large eddy simulation of particle settling in the ocean mixed layer. *Physics of Fluids*, 18(8):085109.

Onink, V., van Sebille, E., Laufk&ouml, C., and tter (2022). Empirical Lagrangian parametrization for wind-driven mixing of buoyant particles at the ocean surface. *Geoscientific Model Development*, 15(5):1995–1995.

Ouellette, N. T., O'Malley, P. J. J., and Gollub, J. P. (2008). Transport of Finite-Sized Particles in Chaotic Flow. *Physical Review Letters*, 101(17):174504.

Perez, L., Cossu, R., Couzi, C., and Penesis, I. (2020). Wave-Turbulence Decomposition Methods Applied to Tidal Energy Site Assessment. *Energies*, 13(5):1245.

Perlin, M., Choi, W., and Tian, Z. (2013). Breaking Waves in Deep and Intermediate Waters. *Annual Review of Fluid Mechanics*, 45(1):115–145.

Pismen, L. M. and Nir, A. (1978). On the motion of suspended particles in stationary homogeneous turbulence. *Journal of Fluid Mechanics*, 84(1):193–206.

Pope, S. B. (2000). *Turbulent Flows: FUNDAMENTALS*. Cambridge University Press, Cambridge.

Qiao, F., Yuan, Y., Deng, J., Dai, D., and Song, Z. (2016). Wave–turbulence interaction-induced vertical mixing and its effects in ocean and climate models. *Philosophical Transactions of the Royal Society A: Mathematical, Physical and Engineering Sciences*, 374(2065):20150201.

Qiao, F., Yuan, Y., Yang, Y., Zheng, Q., Xia, C., and Ma, J. (2004). Wave-induced mixing in the upper ocean: Distribution and application to a global ocean circulation model. *Geophysical Research Letters*, 31(11).

Qureshi, N. M., Bourgoin, M., Baudet, C., Cartellier, A., and Gagne, Y. (2007). Turbulent Transport of Material Particles: An Experimental Study of Finite Size Effects. *Physical Review Letters*, 99(18):184502.

Ragusa, A., Svelato, A., Santacroce, C., Catalano, P., Notarstefano, V., Carnevali, O., Papa, F., Rongioletti, M. C. A., Baiocco, F., Draghi, S., D'Amore, E., Rinaldo, D., Matta, M., and Giorgini, E. (2021). Plasticenta: First evidence of microplastics in human placenta. *Environment International*, 146:106274.

Reeks, M. W. (1977). On the dispersion of small particles suspended in an isotropic turbulent fluid. *Journal of Fluid Mechanics*, 83(3):529–546.

Reijnders, D., Deleersnijder, E., and van Sebille, E. (2022). Simulating Lagrangian Subgrid-Scale Dispersion on Neutral Surfaces in the Ocean. *Journal of Advances in Modeling Earth Systems*, 14(2):e2021MS002850.

Reimers, C. E. and Fogaren, K. E. (2021). Bottom Boundary Layer Oxygen Fluxes During Winter on the Oregon Shelf. *Journal of Geophysical Research: Oceans*, 126(3):e2020JC016828.

Rosa, T. L., Piecho-Santos, A. M., Vettor, R., and Guedes Soares, C. (2021). Review and Prospects for Autonomous Observing Systems in Vessels of Opportunity. *Journal of Marine Science and Engineering*, 9(4):366.

Rouse, H. (1937). Modern Conceptions of the Mechanics of Fluid Turbulence. *Transactions of the American Society of Civil Engineers*, 102(1):463–505.

Rowley, C. W., Mezić, I., Bagheri, S., Schlatter, P., and Henningson, D. S. (2009). Spectral analysis of nonlinear flows. *Journal of Fluid Mechanics*, 641:115–127.

Ruth, D. J., Vernet, M., Perrard, S., and Deike, L. (2021). The effect of nonlinear drag on the rise velocity of bubbles in turbulence. *Journal of Fluid Mechanics*, 924:A2.

Sallée, J., Speer, K., Morrow, R., and Lumpkin, R. (2008). An estimate of Lagrangian eddy statistics and diffusion in the mixed layer of the Southern Ocean. *Journal of Marine Research*, 66(4).

Salmon, H. R. S., Chang, K., Mucignat, C., and Coletti, F. (2025). Behaviour of finite-size floating particles in free-surface turbulence. *Journal of Fluid Mechanics*, 1019:A61.

Santamaria, F., Boffetta, G., Afonso, M. M., Mazzino, A., Onorato, M., and Pugliese, D. (2013). Stokes drift for inertial particles transported by water waves. *Europhysics Letters*, 102(1):14003.

Sato, Y. and Yamamoto, K. (1987). Lagrangian measurement of fluid-particle motion in an isotropic turbulent field. *Journal of Fluid Mechanics*, 175:183–199.

Scherl, I., Strom, B., Shang, J. K., Williams, O., Polagye, B. L., and Brunton, S. L. (2020). Robust principal component analysis for modal decomposition of corrupt fluid flows. *Physical Review Fluids*, 5(5):054401.

Schmid, P. J. (2010). Dynamic mode decomposition of numerical and experimental data. *Journal of Fluid Mechanics*, 656:5–28.

Schmid, P. J. (2011). Application of the dynamic mode decomposition to experimental data. *Experiments in Fluids*, 50(4):1123–1130.

Schmid, P. J. (2022). Dynamic Mode Decomposition and Its Variants. *Annual Review of Fluid Mechanics*, 54(1):225–254.

Schmidt, O. T. and Colonius, T. (2020). Guide to Spectral Proper Orthogonal Decomposition. *AIAA Journal*, 58(3):1023–1033.

Seena, A. and Sung, H. J. (2011). Dynamic mode decomposition of turbulent cavity flows for self-sustained oscillations. *International Journal of Heat and Fluid Flow*, 32(6):1098–1110.

Semeraro, O., Bellani, G., and Lundell, F. (2012). Analysis of time-resolved PIV measurements of a confined turbulent jet using POD and Koopman modes. *Experiments in Fluids*, 53(5):1203–1220.

Shapiro, M. and Goldenberg, M. (1993). Deposition of glass fiber particles from turbulent air flow in a pipe. *Journal of Aerosol Science*, 24(1):65–87.

Shaw, W. J. and Trowbridge, J. H. (2001). The Direct Estimation of Near-Bottom Turbulent Fluxes in the Presence of Energetic Wave Motions. *Journal of Atmospheric and Oceanic Technology*, 18(9):1540–1557.

Sirovich, L. (1987a). Turbulence and the Dynamics of Coherent Structures Part I: Coherent Structures. *Quarterly of Applied Mathematics*, 45(3):561–571.

Sirovich, L. (1987b). Turbulence and the Dynamics of Coherent Structures Part II: Symmetries and Transformations. *Quarterly of Applied Mathematics*, 45(3):573–582.

Sirovich, L. (1987c). Turbulence and the Dynamics of Coherent Structures Part III: Dynamics and Scaling. *Quarterly of Applied Mathematics*, 45(3):583–590.

Skyllingstad, E. D. and Denbo, D. W. (1995). An ocean large-eddy simulation of Langmuir circulations and convection in the surface mixed layer. *Journal of Geophysical Research: Oceans*, 100(C5):8501–8522.

Smedsrud, L. H. and Jenkins, A. (2004). Frazil ice formation in an ice shelf water plume. *Journal of Geophysical Research: Oceans*, 109(C3).

Smith, S. R., Alory, G., Andersson, A., Asher, W., Baker, A., Berry, D. I., Drushka, K., Figurskey, D., Freeman, E., Holthus, P., Jickells, T., Kleta, H., Kent, E. C., Kolodziejczyk, N., Kramp, M., Loh, Z., Poli, P., Schuster, U., Steventon, E., Swart, S., Tarasova, O., de la Villéon, L. P., and Vinogradova-Shiffer, N. (2019). Ship-Based Contributions to Global Ocean, Weather, and Climate Observing Systems. *Frontiers in Marine Science*, 6(434).

Smyth, C., Hay, A. E., and Zedel, L. (2002). Coherent Doppler Profiler measurements of near-bed suspended sediment fluxes and the influence of bed forms. *Journal of Geophysical Research: Oceans*, 107(C8):19–1–19–20.

Snyder, W. H. and Lumley, J. L. (1971). Some measurements of particle velocity autocorrelation functions in a turbulent flow. *Journal of Fluid Mechanics*, 48(1):41–71.

Squires, K. D. and Eaton, J. K. (1991). Measurements of particle dispersion obtained from direct numerical simulations of isotropic turbulence. *Journal of Fluid Mechanics*, 226:1–35.

Stokes, G. G. (1849). On the theory of oscillatory waves. *Trans. Cam. Philos. Soc.*, (8):441–455.

Stommel, H. (1949). Trajectories of small bodies sinking slowly through convection cells. *Journal of Marine Research*, 8(1).

Sullivan, P. P. and McWilliams, J. C. (2010). Dynamics of Winds and Currents Coupled to Surface Waves. *Annual Review of Fluid Mechanics*, 42(Volume 42, 2010):19–42.

Takens, F. (1981). Detecting strange attractors in turbulence. In Rand, D. and Young, L.-S., editors, *Dynamical Systems and Turbulence, Warwick 1980*, Lecture Notes in Mathematics, pages 366–381, Berlin, Heidelberg. Springer.

Taylor, G. I. (1922). Diffusion by continuous movements. *Proceedings of the London Mathematical Society*, 220:196–212.

Teixeira, M. a. C. and Belcher, S. E. (2002). On the distortion of turbulence by a progressive surface wave. *Journal of Fluid Mechanics*, 458:229–267.

Terray, E. A., Donelan, M. A., Agrawal, Y. C., Drennan, W. M., Kahma, K. K., Williams, A. J., Hwang, P. A., and Kitaigorodskii, S. A. (1996). Estimates of Kinetic Energy Dissipation under Breaking Waves. *Journal of Physical Oceanography*, 26(5):792–807.

Thais, L. and Magnaudet, J. (1995). A triple decomposition of the fluctuating motion below laboratory wind water waves. *Journal of Geophysical Research: Oceans*, 100(C1):741–755.

Thais, L. and Magnaudet, J. (1996). Turbulent structure beneath surface gravity waves sheared by the wind. *Journal of Fluid Mechanics*, 328:313–344.

Thakur, G., Brevdo, E., Fučkar, N. S., and Wu, H.-T. (2013). The Synchrosqueezing algorithm for time-varying spectral analysis: Robustness properties and new paleoclimate applications. *Signal Processing*, 93(5):1079–1094.

Thoman, T. X., Kukulka, T., and Gamble, K. (2021). Dispersion of Buoyant and Sinking Particles in a Simulated Wind- and Wave-Driven Turbulent Coastal Ocean. *Journal of Geophysical Research: Oceans*, 126(3):e2020JC016868.

Thorpe, S. A. (1985). Small-scale processes in the upper ocean boundary layer. *Nature*, 318(6046):519–522.

Thorpe, S. A. (2004). Langmuir Circulation. *Annual Review of Fluid Mechanics*, 36(Volume 36, 2004):55–79.

Titmus, A. J. and David Hyrenbach, K. (2011). Habitat associations of floating debris and marine birds in the North East Pacific Ocean at coarse and meso spatial scales. *Marine Pollution Bulletin*, 62(11):2496–2506.

Toschi, F. and Bodenschatz, E. (2009). Lagrangian Properties of Particles in Turbulence. *Annual Review of Fluid Mechanics*, 41(Volume 41, 2009):375–404.

Towne, A., Schmidt, O. T., and Colonius, T. (2018). Spectral proper orthogonal decomposition and its relationship to dynamic mode decomposition and resolvent analysis. *Journal of Fluid Mechanics*, 847:821–867.

Trowbridge, J. H. (1998). On a Technique for Measurement of Turbulent Shear Stress in the Presence of Surface Waves. *Journal of Atmospheric and Oceanic Technology*, 15(1):290–298.

Tu, J. H., Rowley, C. W., Luchtenburg, D. M., Brunton, S. L., and Kutz, J. N. (2014). On Dynamic Mode Decomposition: Theory and Applications. *Journal of Computational Dynamics*, 1(2):391–421.

Tutkun, M. and George, W. K. (2017). Lumley decomposition of turbulent boundary layer at high Reynolds numbers. *Physics of Fluids*, 29(2):020707.

van den Bremer, T. S. and Breivik, Ø. (2017). Stokes drift. *Philosophical Transactions of the Royal Society A: Mathematical, Physical and Engineering Sciences*, 376(2111):20170104.

van Sebille, E., Aliani, S., Law, K. L., Maximenko, N., Alsina, J. M., Bagaev, A., Bergmann, M., Chapron, B., Chubarenko, I., Cózar, A., Delandmeter, P., Egger, M., Fox-Kemper, B., Garaba, S. P., Goddijn-Murphy, L., Hardesty, B. D., Hoffman, M. J., Isobe, A., Jongedijk, C. E., Kaandorp, M. L. A., Khatmullina, L., Koelmans, A. A., Kukulka, T., Laufkötter, C., Lebreton, L., Lobelle, D., Maes, C., Martinez-Vicente, V., Maqueda, M. A. M., Poulain-Zarcos, M., Rodríguez, E., Ryan, P. G., Shanks, A. L., Shim, W. J., Suaria, G., Thiel, M., van den Bremer, T. S., and Wichmann, D. (2020). The physical oceanography of the transport of floating marine debris. *Environmental Research Letters*, 15(2):023003.

Veneziani, M., Griffa, A., Reynolds, A. M., and Mariano, A. J. (2004). Oceanic Turbulence and Stochastic Models from Subsurface Lagrangian Data for the Northwest Atlantic Ocean. *Journal of Physical Oceanography*, 34(8):1884–1906.

Wang, L.-P. and Maxey, M. R. (1993). Settling velocity and concentration distribution of heavy particles in homogeneous isotropic turbulence. *Journal of Fluid Mechanics*, 256:27–68.

Ward, C. P., Armstrong, C. J., Walsh, A. N., Jackson, J. H., and Reddy, C. M. (2019). Sunlight Converts Polystyrene to Carbon Dioxide and Dissolved Organic Carbon. *Environmental Science & Technology Letters*, 6(11):669–674.

Warhaft, Z. (2008). Laboratory studies of droplets in turbulence: Towards understanding the formation of clouds. *Fluid Dynamics Research*, 41(1):011201.

Weil, J. C., Sykes, R. I., and Venkatram, A. (1992). Evaluating Air-Quality Models: Review and Outlook. *Journal of Applied Meteorology (1988-2005)*, 31(10):1121–1145.

Wells, M. R. and Stock, D. E. (1983). The effects of crossing trajectories on the dispersion of particles in a turbulent flow. *Journal of Fluid Mechanics*, 136:31–62.

Wetchagarun, S. and Riley, J. J. (2010). Dispersion and temperature statistics of inertial particles in isotropic turbulence. *Physics of Fluids*, 22(6):063301.

Williams, J. J., Bell, P. S., and Thorne, P. D. (2003). Field measurements of flow fields and sediment transport above mobile bed forms. *Journal of Geophysical Research: Oceans*, 108(C4).

Williams, M. O., Kevrekidis, I. G., and Rowley, C. W. (2015). A Data–Driven Approximation of the Koopman Operator: Extending Dynamic Mode Decomposition. *Journal of Nonlinear Science*, 25(6):1307–1346.

Xu, H. and Bodenschatz, E. (2008). Motion of inertial particles with size larger than Kolmogorov scale in turbulent flows. *Physica D: Nonlinear Phenomena*, 237(14):2095–2100.

Xuan, A., Deng, B.-Q., and Shen, L. (2020). Numerical study of effect of wave phase on Reynolds stresses and turbulent kinetic energy in Langmuir turbulence. *Journal of Fluid Mechanics*, 904:A17.

Yang, D., Chamecki, M., and Meneveau, C. (2014). Inhibition of oil plume dilution in Langmuir ocean circulation. *Geophysical Research Letters*, 41(5):1632–1638.

Young, D. L. and Webster, D. R. (2018). Assessment of single-instrument techniques for removing wave bias from Reynolds stress estimates. *Limnology and Oceanography: Methods*, 16(1):35–50.

Yudine, M. I. (1959). Physical Considerations on Heavy-Particle Diffusion. In Landsberg, H. E. and Van Mieghem, J., editors, *Advances in Geophysics*, volume 6, pages 185–191. Elsevier.

Zhang, Z., Legendre, D., and Zamansky, R. (2019). Model for the dynamics of micro-bubbles in high-Reynolds-number flows. *Journal of Fluid Mechanics*, 879:554–578.

Zhao, L., Challabotla, N. R., Andersson, H. I., and Variano, E. A. (2015). Rotation of Nonspherical Particles in Turbulent Channel Flow. *Physical Review Letters*, 115(24):244501.

Zhu, Q., van Prooijen, B. C., Wang, Z. B., Ma, Y. X., and Yang, S. L. (2016). Bed shear stress estimation on an open intertidal flat using in situ measurements. *Estuarine, Coastal and Shelf Science*, 182:190–201.